Impulsive Stimulated Light Scattering from Glass-Forming Liquids: Structural Relaxation, Orientational Relaxation and Testing of Mode Coupling Theory

by

Yongwu Yang

B.S.(Physics) Huazhong Normal University (1987)
M.S.(Physics) Institute of Physics, Chinese Academy of Sciences(1990)

Submitted to the Department of Chemistry
in partial fulfillment of the requirements for the degree of

Doctor of Philosophy

at the

MASSACHUSETTS INSTITUTE OF TECHNOLOGY

September 1996

© Massachusetts Institute of Technology 1996. All rights reserved.

Author ....
Department of Chemistry
August 4, 1996

Certified by ....
Keith A. Nelson
Professor of Chemistry
Thesis Supervisor

Accepted by ....
Dietmar Seyferth
Chairman, Departmental Committee on Graduate Students

MASSACHUSETTS INSTITUTE
OF TECHNOLOGY

SEP 13 1996

ARCHIVES

This doctoral thesis has been examined by a committee of the Department of Chemistry as follows:

Professor Irwin Oppenheim ______________________ Chairman

Professor Keith A. Nelson ______________________ Thesis Supervisor

Professor Moungi G. Bawendi ______________________

Impulsive Stimulated Light Scattering from Glass-Forming Liquids: Structural Relaxation, Orientational Relaxation and Testing of Mode Coupling Theory

by

Yongwu Yang

Submitted to the Department of Chemistry
on August 4, 1996, in partial fulfillment of the
requirements for the degree of
Doctor of Philosophy

Abstract

We have applied a time-resolved polarized/depolarized light scattering technique, impulsive stimulated light scattering (ISS), to glass-forming liquids to study the liquid-glass transition phenomena. We have compared the results to the predictions of a first-principles theory, the mode coupling theory (MCT).

We have developed a theoretical understanding of viscoelastic properties of viscous liquids measured with ISS. By using the generalized hydrodynamics equations, we have derived the density response functions to the impulsive heating and impulsive electrostrictive force. There appear three modes including the acoustic mode, thermal diffusion mode, and relaxation or Mountain mode in ISS data. The structural relaxation dynamics can be obtained either from the time-dependence of the acoustic mode or from the relaxation mode. In addition, the relaxation strength can be determined from the relative amplitude ratio of the relaxation mode to the thermal diffusion mode. Both the relaxation dynamics and the relaxation strength can be compared to fundamental theoretical predictions.

We have conducted ISS experiments on two model fragile glass formers, an organic molecular liquid salol and an ionic salt mixture calcium nitrate/potassium nitrate (CKN). The temperature dependences of the relaxation strengths or Debye-Waller factors for both salol and CKN show a square-root cusp at a crossover temperature T_c. The relaxation mode dynamics are characterized from nanosecond to millisecond time scales and show a characteristic change around T_c. These findings are consistent with the MCT predictions. We have also characterized the acoustic mode dynamics in salol over a frequency range from 10 MHz to several GHz. The observed α relaxation peaks at high temperatures are analyzed in terms of a stretched exponential function. The acoustic modulus spectra at low temperatures are compared to the susceptibility spectra measured in depolarized light scattering and to the MCT predictions.

We have also performed preliminary ISS experiments on salol to monitor transverse acoustic wave propagation and orientational relaxation. Further experimental studies are suggested.

Thesis Supervisor: Keith A. Nelson
Title: Professor of Chemistry

Acknowledgements

First of all, I would like to express my deepest appreciation to my advisor, Keith Nelson, for his scientific insight and financial support during the course of my graduate career. His comments and suggestions were a great help to me throughout my graduate work.

It has been a great experience to work in the Nelson group with such a friendly and helpful group of people. I would like to begin to thank John Rogers for introducing me the picosecond laser system. I have benefited greatly by working with him on thin films projects (not included in this thesis) during the first two years. He was always ready to discuss just about anything at any time. Ion Halalay's enthusiasm on science has encouraged me to work on the glass-transition projects described in this thesis. Anil Duggal and Scott Silence collected some of the data on salol described in Chapters 6 and 7. Lisa Dhar answered many of my questions on C programming and Mac programs. Andrew Cook was very helpful on computer problems, especially on the linux operating system. Special thanks to Pat Huang for carrying out some of the experiments I would like to do, but don't have the time to do. He has a bright future. Alex Maznev is willing to discuss any topics including possible research projects in this lab. I would also like to thank Dora Paolucci and Tanya Kanigan, the later additions to the picosecond lab, who are carrying on the projects I have been working on these years. Dora proof-read the entire thesis. Thanks to Donghong Wu, Weining Wang, Jianping Zhou, Dutch Chung, Ciaran Brennan, and Marc Wefers, they were all helpful. I would also like to thank all current and former members of the Nelson group for making the basement of building two an enjoyable place.

I thank Prof. George Benedek's group for their generosity of letting me use their laboratory facilities. All the samples used for experiments described in this thesis were prepared in their laboratory.

Prof. Irwin Oppenheim and Prof. Moungi Bawendi, as members of my thesis committee, were very generous with both their time and advice. I would also like to thank Prof. Oppenheim for his first-year graduate course, Statistical Mechanics (II), which has introduced me modern statistical approaches to non-equilibrium statistical problems.

I would like to thank Prof. Herman Cummins and Prof. Wolfgang Götz for many helpful discussions on the work described in this thesis. I thank Prof. Cummins and Dr. Matthias Fuchs for providing data and fits presented in Figs. 1-2 and 6-11.

I would like to express my deep gratitude, appreciation and love to my wife Canwen Liu, without whose encouragement and support in the past twelve years, I would not have achieved so far. Her careful reading of this thesis is responsible for its clarity. I would like to express my love and appreciation to my son, Binley Yang, and my little twin sons Lingene Harvey Yang and Hongsen Mitchell Yang, who have forgiven me for not spending much time with them over the past couple of months. I am also grateful to my parents-in-law for their great help during our difficult times. Finally, I would like to express my love and appreciation to my parents, brother and sisters for their encouragement and support. Their love from the other side of the

sphere means a great deal to me.

Preface

This thesis consists of the work I did over the last three years on the liquid-glass transition phenomena. In the first two years I worked on thin film projects which are not described in this thesis. Some of the results have been published.

Contents

List of Figures

List of Tables

List of Abbreviations

MCT	Mode Coupling Theory
ISS	Impulsive Stimulated Light Scattering
ISTS	Impulsive Stimulated Thermal Scattering
ISBS	Impulsive Stimulated Brillouin Scattering
VV ISS	All s-Polarized ISS
VH ISS	Cross-Polarized ISS
DLS	Depolarized Light Scattering
PCS	Photon Correlation Spectroscopy
BS	Rayleigh-Brillouin Scattering
VV BS	Polarized Rayleigh-Brillouin Scattering
VH BS	Depolarized Rayleigh-Brillouin Scattering
KWW	Kohlrausch-Williams-Watts
VTF	Vogel-Tamman-Fulcher
CW	Continuous Wave
YAG	Yttrium Aluminum Garnet
BBO	β-Barium Borate
RTD	Resistance Thermal Detector
CKN	$Ca_{0.4}K_{0.6}(NO_3)_{1.4}$

Chapter 1

Introduction

The dynamics of glass-forming liquids have come under intense study in recent years, largely as a result of advances in both experimental and theoretical approaches to the problem of complex relaxation. From the experimental side, methods newly developed or refined and/or newly applied to glass-forming materials include measurements of neutron spin echoes [1, 2], neutron time-of-flight [1, 3], frequency-dependent heat capacities [4], frequency-dependent dielectric constants [4-7], depolarized light scattering (DLS) [8-10], photon correlation spectroscopy (PCS) [11, 12], and impulsive stimulated light scattering (ISS), the subject of this thesis. Some well-established experimental methods have also been extended into previously inaccessible ranges of time, frequency, or wavevectors. In addition, new theoretical analyses of experimental observables such as DLS have revealed possibilities that were not earlier appreciated for extraction of complex relaxation dynamics [13]. This array of experimental methods has helped to deal with the central experimental challenge presented by glass-forming liquids, namely the broad range of time scales (typically several decades) over which relaxation occurs even at a single temperature and the extraordinary range (about 14 decades) covered as the temperature is varied across the liquid and glass regions. Concerning the theoretical treatment of glass-forming liquids, much of the recent surge in activity has been based on the results of mode coupling theory(MCT) [1, 14-16] which have offered a number of experimentally testable predictions. The ongoing challenge between experiment and theory in this area has spurred the rapid development of both.

In this thesis we present theoretical and experimental studies of impulsive stimulated light scattering on glass-forming liquids. We provide a detailed theoretical description of this method based on generalized hydrodynamics equations. We also describe ISS experiments on two different glass-forming liquids to test the mode coupling theory predictions. In Sec. 1.1 we give a brief description of the general features of the liquid-glass transition. Mode coupling theory of the liquid-glass transition and its predictions relevant to our experiments are summarized in Sec. 1.2. In Sec. 1.3 we briefly review several experimental results which support the basic idea of MCT. However more experimental tests of MCT are still necessary, and this is partly the motivation of the work described in this thesis. Section 1.4 gives an overview of the thesis.

1.1 General Features of Liquid-Glass Transition

When a liquid is slowly cooled below its bulk melting temperature T_m, it usually undergoes a first-order phase transition and forms a crystal, via a nucleation and growth process. Crystal growth starts when the size of a crystalline nucleus produced by spontaneous fluctuations of the liquid is larger than some critical size, and then the nucleus continues to grow until it envelopes the entire system. Because a critical nucleus can take a long time to form, one can prevent nucleation by cooling the liquid at a sufficiently high rate and thereby avoiding crystallization. Upon sufficiently fast cooling, the liquid can be supercooled indefinitely and can form an amorphous solid called a glass at or below the glass transition temperature T_g. The state of the system at T above T_g but below T_m is called a supercooled liquid. The temperature T_g is conventionally defined as the temperature where the viscosity η reaches 10^{13} poise [1 poise = 0.1 Nsm^{-2}], or defined as the temperature at which the specific heat measured in calorimetric experiments shows a jump. The latter is called the calorimetric glass transition temperature. This is a ubiquitous liquid-glass transition phenomenon and is believed to happen in all liquids including ones with metallic, ionic, covalent or Vander Waals bonds [17-19]. For liquids like argon the cooling rates needed for supercooling are much greater than that can be currently achieved in the laboratory. However, it is possible to slow down the cooling rate for liquids with sufficient anisotropy or complexity to frustrate nucleation so that experiments can be performed close to the region of the glass transition. In this section we summarize a series of features of supercooled dynamics.

1.1.1 Non-Arrhenius Behavior

As a liquid is supercooled, its viscosity increases dramatically from $\eta \simeq 10^{-2}$ poise at T_m to $\eta \simeq 10^{13}$ poise at T_g. Like any other transport coefficient, the viscosity reflects the underlying movement of the liquid molecules. The viscosity at T_g is the value at which the liquid takes approximately half an hour to respond to a small external stress. The variation of η is essentially proportional to that for the time scale τ of the relevant relaxation process. Thus the relaxation time increases by more than 14 orders of magnitude from T_m to T_g, perhaps the largest change ever known to occur in any physically measurable material property.

If some activated process involving crossing over a barrier of potential energy $(k_B T_A)$ could be the essential microscopic transport mechanism, one would expect an Arrhenius law for the viscosity η or the relaxation time τ,

$$\eta_A = \eta_A^0 e^{T_A/T}; \qquad \tau_A = \tau_A^0 d^{T_A/T}. \tag{1.1}$$

In an Arrhenius plot of $\log \eta_A$ or $\log \tau_A$ versus $1/T$, this yields a straight line. As shown in Fig. 1-1, only those liquids with open networks like SiO_2 and GeO_2 show an Arrhenius variation of viscosity or structural relaxation time between the glass transition temperature and the high temperature limit. These systems are classified as "strong" glass-forming liquids [20, 21] because their glassy structures are believed to be frozen rigidly into deep, isolated local potential energy minimum. However, for the liquids characterized by simple non-directional Coulomb attractions or by van der Waals interactions, the viscosities vary in a strongly non-Arrhenius fashion

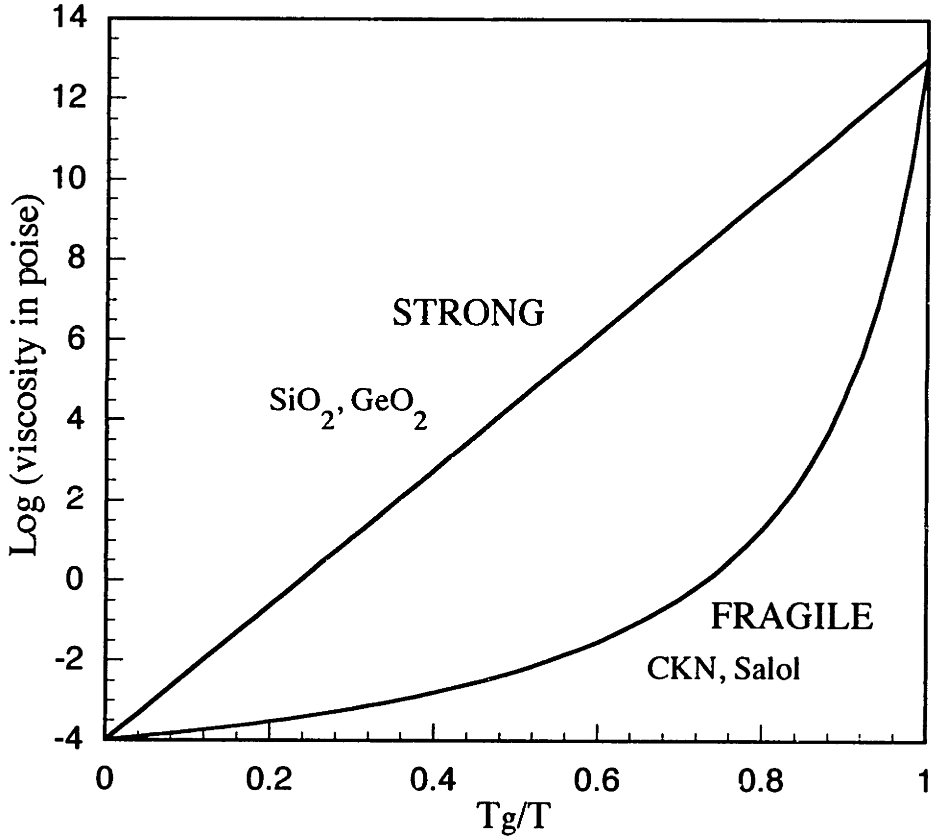

Figure 1-1: T_g-scaled Arrhenius plots of viscosities or relaxation times showing the strong/fragile pattern of liquid behavior

between T_g and T_m. These liquids are called "fragile" liquids, suggestive of many local potential energy minima which are closely spaced in energy and position phase space.

Several functional forms have been proposed to describe the strongly non-Arrhenius behavior of the viscosity. Among them an often used expression is the Vogel-Tamman-Fulcher (VTF) equation

$$\eta_{\mathrm{VTF}} = \eta^0_{\mathrm{VTF}} \exp\left[\frac{T_{\mathrm{VTF}}}{T - T_0}\right], \tag{1.2}$$

or for the relaxation time

$$\tau_{\mathrm{VTF}} = \tau^0_{\mathrm{VTF}} \exp\left[\frac{T_{\mathrm{VTF}}}{T - T_0}\right]. \tag{1.3}$$

This formula anticipates a special singularity at a temperature $T_0 < T_g$. Since we are concerned with the relaxation dynamics above T_g, we will not try to discuss the significance of the temperature T_0. (For discussion of T_0, see, for example, Ref. [4])

1.1.2 α Relaxation Stretching

The strongly temperature-sensitive slow processes mentioned above are believed to be due to the cooperative motion of large clusters of molecules, and are therefore referred to as structural relaxation. The slowest of these is called the α relaxation process, the second slowest one is called the β relaxation, etc.

An outstanding feature of structural relaxation is the stretching of the dynamics over time or frequency intervals of several orders of magnitude. We will describe the appearance of this feature in both time domain and frequency domain experiments.

Let us begin with the time domain experiments. In time domain experiments either the relaxation function $\phi(t)$ or the response function $\psi(t)$ is measured. In the former case, the system is disturbed by a perturbation field which is switched on slowly at time $t = -\infty$ and turned off abruptly at $t = 0$. The change of the variable A is then monitored as a function of time for $t \geq 0$. In the linear response regime

$$\delta A(t) = \phi(t)\delta A(t = 0). \tag{1.4}$$

In the experiments where the response function $\psi(t)$ is measured, the external field $a(t)$ is switched on suddenly at $t = 0$ and $a(t) = a_0 \exp(-\epsilon t), \epsilon \rightarrow +0$ for $t > 0$ [22]. In the linear regime one has

$$\delta A(t) = \psi(t)\delta A(t = +\infty). \tag{1.5}$$

Since there is simple relation between $\psi(t)$ and $\phi(t)$:

$$\psi(t) = 1 - \phi(t), \tag{1.6}$$

we will discuss the characteristics of structural relaxation in terms of the relaxation function $\phi(t)$.

It has been experimentally established that the relaxation function $\phi(t)$ does not follow the Debye model,

$$\phi_D(t) = f \exp[-t/\tau_\alpha]. \tag{1.7}$$

Instead it shows stretched exponential decay and can be described reasonably well by the Kohlrausch-William-Watts (KWW) function

$$\phi_{\mathrm{KWW}}(t) = f \exp[-(t/\tau_\alpha)^\beta], \tag{1.8}$$

with the stretching parameter $0 < \beta < 1$. The difference between the Debye model and the KWW function is obvious. While $\phi_D(t)$ decays from 90% to 10% of its initial value in a time interval of 1.34 decades, the dynamical window of a KWW relaxation process spans more than two decades.

The structural relaxation dynamics of a system can also be probed in the frequency domain. In this case, one applies an external field a with its amplitude a_0 and frequency ω to the system and measures the induced change δA of the conjugate variable A. In the linear response regime, one can write

$$\delta A = \chi(\omega) a, \tag{1.9}$$

where $\chi(\omega) = \chi'(\omega) + i\chi''(\omega)$ is the dynamical susceptibility of variable A, which is independent of a_0. The real part $\chi'(\omega)$ is even in ω and describes the reactive response. The imaginary part $\chi''(\omega)$ is odd in ω and has a property $\omega\chi''(\omega) \geq 0$. $\chi''(\omega)$ describes dissipation phenomena and is called the susceptibility spectrum. The real and imaginary parts of $\chi(\omega)$ are connected to each other through the Kramers-Kronig relation.

The relaxation functions $\phi(t)$ and the dynamical susceptibility $\chi(\omega)$ are the properties of the system. Therefore for the same observable A, they should provide the same dynamical information of the system. In fact, $\phi(t)$ is equivalent to $\chi(\omega)$ through the Kubo relation [23]

$$\chi(z)/\chi_T = z\phi(z) + 1, \tag{1.10}$$

where $\chi_T = \chi(z \rightarrow 0)$ is the thermodynamic derivative and $\phi(z)$ is the Laplace transform of $\phi(t)$:

$$\phi(z) = i\int_0^\infty dt e^{izt}\phi(t) = \mathrm{LT}[\phi(t)](z) \qquad \mathrm{Im}z > 0. \tag{1.11}$$

In particular, with $z = \omega + i0$ and $\phi(\omega + i0) = \phi'(\omega) + i\phi''(\omega)$ one finds from Eq. 1.10

$$\chi''(\omega)/\chi_T = \omega\phi''(\omega). \tag{1.12}$$

Here $\phi''(\omega)$ is the relaxation spectrum. $\phi'(\omega)$ and $\phi''(\omega)$ are the Fourier transform of the relaxation function $\phi(t)$,

$$\begin{aligned} \phi'(\omega) &= -\int_0^\infty dt \sin(\omega t)\phi(t), & (1.13) \\ \phi''(\omega) &= \int_0^\infty dt \cos(\omega t)\phi(t). & (1.14) \end{aligned}$$

Therefore for a Debye relaxation function (Eq. 1.7), one gets a Lorentzian relaxation spectrum

$$\phi''_D(\omega) = f\frac{\omega\tau_\alpha}{1 + (\omega\tau_\alpha)^2}. \tag{1.15}$$

The width in the curve of $\chi''_D(\omega) = \omega\phi''_D(\omega)$ versus ω at half height is about 1.14 decades. But experimental spectra of glass-forming liquids are stretched over several orders of magnitude of frequency variation.

1.1.3 α Relaxation Strength

Besides the dynamical parameters τ_α and β, another important parameter specifying the α relaxation is its relaxation strength f_q. It is defined as the initial amplitude of the α relaxation function or the integrated area of the relaxation spectrum $\phi''(\omega)$ with respect to ω over the peak.

The α relaxation strength can be measured, in principle, in neutron scattering experiments. For an ideal solid the measured density spectrum includes a strictly elastic contribution and a continuum due to inelastic excitations

$$\phi_q''(\omega) = \pi f_q \delta(\omega) + \text{continuum}. \tag{1.16}$$

The probability for elastic scattering f_q, or the intensity of the elastic line, is called the Debye-Waller factor. For a glass or a supercooled liquid, the elastic line in neutron scattering is replaced by a quasi-elastic peak. Therefore the α relaxation strength is referred to as effective Debye-Waller factor of the glass or the supercooled liquid. Obviously one has to choose a cutoff frequency ω_c such that only the α peak and the whole α peak is bracketed within the interval $|\omega| < \omega_c$. The cutoff frequency ω_c is often given by the size of the experimental frequency window. Thus with the limited frequency window available it sometimes poses a problem for the determination of the Debye-Waller factor, especially at higher temperatures when the α peak broadens and the higher-frequency part of the spectrum falls outside of the experimental frequency window. In the following Chapters, we shall show an alternative optical method to measure the Debye-Waller factor f_q in the low-q limit. With this method cutoff frequency problem can be avoided entirely.

For $T < T_g$, f_q is found to show a linear temperature dependence. However, for $T > T_g$, f_q exhibits a strong non-linear decrease with increasing T. In Sec. 1.2, we will give a MCT equation concerning the temperature dependence of the Debye-Waller factor.

1.1.4 β-Relaxation Regime

Between the very slow α relaxation peak and the band of typical microscopic (optic phonon) excitations, there is an intermediate or mesoscopic region called the β-relaxation regime. In this region, there is a secondary or β relaxation, which precedes the α relaxation in time. There are two features of the β relaxation which are most different from those of the α relaxation. One is that the β relaxation shows smooth temperature dependence and the other is that the relaxation stretching is more pronounced for the β peak than for the α resonance.

In the β-relaxation regime which consists of the β relaxation and the high frequency part of the α relaxation, the relaxation dynamics follow power law dependences. For the initial part of the α decay process, the von Schweidler law is proposed to describe its dynamics

$$\phi_{\mathrm{von}}(t) = f_{\mathrm{von}} - h_{\mathrm{von}}(t/\tau_\alpha)^b \qquad 0 < b < 1. \tag{1.17}$$

Equivalently for the susceptibility spectrum one has $\chi''_{\mathrm{von}}(\omega) \propto \omega^{-b}$. Note that even though Eq. 1.17 could be treated as a limiting case of Eq. 1.8 under the condition $t/\tau_\alpha \ll 1$, the critical exponent b is not necessarily the same as the stretching parameter β. Experiments have shown that the β relaxation spectra follow a power law behavior, i.e.

$$\phi_q(t) \propto t^{-a} \qquad \chi''_q(\omega) \propto \omega^a. \tag{1.18}$$

In addition, the structural relaxation follows the scaling law or time temperature superposition principle. We will delay the discussion to the next section.

1.2 Brief Review of Mode Coupling Theory of Liquid-Glass Transition

Since mode coupling theory was first developed successfully to describe the dynamics of liquids in the region of the liquid-vapor critical point [24], it has found many applications. For example, it has been used to evaluate transport coefficients and their long time tails in fluids away from critical points, and to describe Brownian motion and steady state systems [25]. In recent years, applications of the mode coupling approach include in the description of granular flow [26], and most actively, in the liquid-glass transition (for a complete review of MCT see Ref. [1]). This section is devoted to the brief review of the mode coupling theory of the liquid-glass transition.

Mode coupling theory interprets the liquid-glass transition as the interplay of two physical mechanism inherent to liquid state dynamics: the cage effect and the thermally assisted hopping processes [27-29]. The cage effect is seen as the origin of the dramatic slowing down of the dynamics in supercooled liquids. A particle is trapped in the cage formed by its neighbors and each one of the neighboring particles again is trapped by its own neighbors, and so on. Therefore a movement of any one of the particles is possible only when the cages rearrange cooperatively. As the particle density is increased or equivalently the temperature is decreased, the particle cannot move very far so diffusion over long distances is not possible. The particle merely rattles in the cage and experiences many shapes of the cages. At a critical temperature T_c or critical density, it then drives the system towards the ideal ergodic-nonergodic transition. This result is produced in the idealized MCT where only the cage effect is considered. However, the cages are not given static entities because the surrounding particles which form the cages are not fixed. The trapped particle can move because its neighbors move out of the way via thermally assisted hopping; and the neighbors can move because their neighbors move out of the way, etc. Because the particles build up this so-called backflow pattern, ergodic dynamics are established. As the system approaches T_c or the critical density, the hopping effect contribution becomes comparable to that of the cage effect, which provide another channel for density fluctuations. These processes allow structural rearrangements even above the critical density or below T_c. Thus inclusion of this effect in the extended MCT leads to smearing of the sharp ergodic-nonergodic transition. Below T_c, hopping events are the elementary steps leading to complex relaxation. Structural relaxation continues to slow down until its time scale becomes slower than that of the experimental probe at T_g. At this point the system falls out of equilibrium.

Mode coupling theory is the first first-principles approach to the liquid-glass transition. Under a number of assumptions and approximations whose validity remain under examination, it provides detailed quantitative predictions for complex structural relaxation. Substantial experimental attention has now shifted toward examination of the MCT predictions. In this thesis we will describe a method which has a dynamical window of more than 6 decades for testing some of MCT predictions. In the rest of this section we begin with MCT equation and then summarize the MCT predictions which are relevant to our experiments.

1.2.1 Mode Coupling Theory Equations

In 1984 mode coupling theory was proposed to describe the liquid-glass transition [14, 15]. Since then, there has been considerable progress on the theoretical side toward understanding of structural relaxation in supercooled liquids. The basic quantities of the MCT for structural relaxation are the normalized autocorrelation functions

$$\phi_q(t) = <\delta\rho_q(t)\delta\rho_q(0)>/S_q \qquad (1.19)$$

of the density fluctuation $\delta\rho_q(t)$ at wavevector magnitude q. $S_q = <|\delta\rho_q|^2>$ denotes the structure factor, the spatial Fourier transform of the averaged distribution of particle pairs. MCT starts with generalized oscillator equations of motion for $\phi_q(t)$,

$$\ddot{\phi}_q(t) + \gamma_q\Omega_q^2\dot{\phi}_q(t) + \Omega_q^2\phi_q(t) + \Omega_q^2\int_0^t dt' m_q(t-t')\dot{\phi}_q(t') = 0, \qquad (1.20)$$

where $\Omega_q = \sqrt{q^2v^2/S_q}$ (the thermal velocity $v = \sqrt{k_BT/m}$) and γ_q specify Hooke's restoring forces and Newton's friction constants, respectively. Just as γ_q is the Newton's friction constant, the kernel is the constant of proportionality between a force at time t and a velocity at a preceding time t'. Thus the integral in Eq. 1.20 describes the retardation effect. The essence of the MCT is to use the mode coupling approximation to express the kernel $m_q(t)$ in terms of products of correlation functions for pairs of density fluctuations, and pairs of density fluctuations and currents. Explicitly, the memory function (or kernel) in the idealized MCT with activated hopping processes (discussed below) not included is expressed as

$$m_q(t) = \sum_{q_1} V^{(1)}(q, q_1)\phi_{q_1}(t) + \sum_{q_1, q_2} V^{(2)}(q, q_1, q_2)\phi_{q_1}(t)\phi_{q_2}(t) + \cdots . \tag{1.21}$$

Hence MCT deals with a closed set of integro-differential equations which can be solved numerically.

Equation 1.20 can be rewritten as a two step fraction via Laplace transformation:

$$\phi_q(z) = -\frac{1}{z - \dfrac{\Omega_q^2}{z + \Omega_q^2(\gamma_q + m_q(z))}}. \tag{1.22}$$

Substituting the above equation into $\kappa_q(z) = [1 + z\phi_q(z)]S_q/(nk_BT)$, we obtain an equivalent result for the frequency-dependent dynamical compressibility,

$$\kappa_q(\omega) = \frac{-\dfrac{q^2}{\rho_0}}{\omega^2 - \dfrac{q^2}{\rho_0}\dfrac{1 - \omega(i\gamma_q + m_q(\omega))}{\kappa_T}}, \tag{1.23}$$

which reduces to the isothermal compressibility κ_T in the $q \to 0$ and $\omega \to 0$ limits. For sound excitations in a simple liquid the compressibility reads

$$\kappa_q(\omega) = -\frac{q^2/\rho_0}{\omega^2 - q^2 M/\rho_0}, \tag{1.24}$$

where the sound speed is given by the longitudinal acoustic modulus M and the mass density ρ_0 as $c^2 = M/\rho_0$. Comparison of Eq. 1.23 to 1.24 leads to a generalized wavevector and frequency dependent longitudinal elastic modulus:

$$M_q(\omega) = \frac{1 - \omega(i\gamma_q + m_q(\omega))}{\kappa_T}. \tag{1.25}$$

In addition to the viscosities yielding an imaginary part for the modulus (γ_q term), the structural relaxation which is described by the relaxation kernel $m_q(\omega)$, induces a frequency dependence for the modulus. The imaginary part of the kernel, i.e. the relaxation spectrum $m''_q(\omega)$, yields additional acoustic damping and the real part $m'_q(\omega)$ leads to shifts of the acoustic frequency. The structural relaxation contribution to the modulus $M_q(\omega)$ can be closely related to the one for the density autocorrelation spectrum $\phi''_q(\omega)$, the Fourier cosine transform of $\phi_q(t)$.

1.2.2 Predictions of the Mode Coupling Theory

1.2.2.1 Nonergodicity Parameter $f_q(T)$

A central prediction of MCT concerns the nonergodicity parameter $f_q(t)$, the $t \to \infty$ limit of $\phi_q(t)$. In the idealized MCT where activated hopping processes are assumed to be absent, the analysis of Eq. 1.20 shows that there exists a critical temperature T_c at which a transition from a weak-coupling ergodic or liquid-like state to a strong-coupling nonergodic or ideal glass state occurs. For $T > T_c$ the density fluctuations relax toward equilibrium at sufficiently long time, i.e. $f_q(T) = 0$. At $T = T_c$ structural arrest occurs and $\phi_q(t \to \infty) = f_q^c > 0$. For $T < T_c$, $\phi_q(t \to \infty) = f_q$ increases rapidly with decreasing T.

As discussed in Sec. 1.1.3, the α relaxation appears in neutron scattering as a quasi-elastic peak. Thus the integrated area of the α peak is defined as the effective Debye-Waller factor $\tilde{f}_q$, which corresponds to the value of $\phi_q(t)$ not at $t = \infty$, but at the beginning of the α relaxation. In the idealized MCT, $\tilde{f}_q(T)$ is expected to show a square-root cusp at T_c, i.e.

$$\tilde{f}_q(T) = \begin{cases} f_q^c + O(\sigma) & T > T_c, \\ f_q^c + \tilde{h}_q\sqrt{\sigma} + O(\sigma) & T \le T_c, \end{cases} \tag{1.26}$$

where $\sigma = (T_c - T)/T_c$ is the dimensionless separation parameter and f_q^c varies smoothly with temperature. In the extended MCT, the predicted behavior is similar but with some rounding of the cusp around T_c. Note that the crossover temperature

T_c is a wavevector-independent property of the material, so its value should not depend on the experimental method used for its determination.

1.2.2.2 The α Relaxation

Within the idealized MCT, α relaxation only exists above T_c in the liquid state. MCT predicts that the α relaxation dynamics above T_c obeys the time-temperature superposition principle, or the scaling law,

$$\phi_q(t;T) = F(t/\tau_\alpha(T)). \tag{1.27}$$

Here the master functions F are temperature independent to the lowest order, and the temperature dependences of the relaxation functions $\phi_q(t;T)$ only enter via the scaling of the characteristic α relaxation times $\tau_\alpha(T)$. The relaxation time τ_α diverges at T_c via a power law dependence

$$\tau_\alpha = \omega_\alpha^{-1} = t_0|\sigma|^{-\gamma}. \tag{1.28}$$

The scaling functions F are generally well approximated by the KWW function of Eq. 1.8 with T-independent stretching exponent β.

When hopping processes are included in the extended MCT, $\phi_q(t)$ is no longer completely arrested at sufficiently long times to form an "ideal" glass. Instead, below T_c the α relaxation dynamics continue and evolve smoothly with decreasing temperature. Also, the divergence of $\tau_\alpha(T)$ is eliminated. Up to date, the detailed temperature dependence of τ_α around T_c has not been worked out theoretically.

1.2.2.3 The Factorization Property

In the β-relaxation region, Eqs. 1.20 are solved by the following factorization of time and wavevector dependencies:

$$\phi_q(t) = f_q^c + h_q G(t), \tag{1.29}$$

for $|G(t)| \ll 1$. Here h_q is the critical amplitude and f_q^c is the non-ergodicity parameter or Debye-Waller factor at T_c.

Similar expressions hold for all those correlators between variables X and Y which have a nonzero projection on density fluctuations or products of density fluctuations,

$$\phi_{\mathrm{XY}}(t) = f_{\mathrm{XY}}^c + h_{\mathrm{XY}} G(t). \tag{1.30}$$

The time independent quantities f_{XY}^c and h_{XY} have the same meaning as f_q^c and h_q in Eq. 1.29, which can, in principle, be calculated from the equilibrium static structure factor S_q taken at the critical temperature T_c. For all pairs X and Y, the time and temperature dependences of the correlation function $\phi_{\mathrm{XY}}(t)$ are the same, as expressed in the so-called β correlator $G(t)$. By performing the Fourier-Laplace transformation, one obtains

$$\phi_{\mathrm{XY}}(z) = -\frac{f_{\mathrm{XY}}^c}{z} + h_{\mathrm{XY}} G(z). \tag{1.31}$$

For the corresponding susceptibility, one has

$$\chi_{\mathrm{XY}}'' = h_{\mathrm{XY}} \omega G''(\omega) = h_{\mathrm{XY}} \chi''(\omega). \tag{1.32}$$

In other words, all susceptibility spectra have the same frequency dependence given by the β-susceptibility spectrum $\chi''(\omega)$ and they only differ up to a constant factor h_{XY}.

One example is for the generalized longitudinal acoustic modulus M in Eq. 1.25 [30]. Apart from a background ($i\gamma_q$ term) contribution, the ω-dependent part of the acoustic modulus is introduced by the memory function $m_q(t)$, which has the factorization property, $m_q(t) = m_q^c + h_q^m G(t) + O(G^2)$, in the β-relaxation regime. Equation 1.25 then becomes

$$M_q(\omega) = \frac{1 + m_q^c - \omega(i\gamma_q + h_q^m G(\omega))}{\kappa_T}. \tag{1.33}$$

Therefore for the structural relaxational part of the acoustic modulus, one has

$$M_R''(\omega) = h_M \omega G''(\omega) = h_M \chi''(\omega). \tag{1.34}$$

Another example is for the longitudinal acoustic compliance J, which is the inverse of the longitudinal acoustic modulus M [30]. Since the condition $G(t)$ being small means that $\omega G(\omega)$ is small, one gets

$$\begin{aligned} J_q(\omega) &= \frac{1}{M_q(\omega)} = \frac{\kappa_T}{1 + m_q^c - \omega(i\gamma_q + h_q^m G(\omega))} & (1.35) \\ &= \kappa_T \left[\frac{1}{1 + m_q^c} + \frac{\omega(i\gamma_q + h_q^m G(\omega))}{(1 + m_q^c)^2} \right]. & (1.36) \end{aligned}$$

In the above derivation, we have considered the fact that the background contribution ($i\gamma_q$ term) is small. Eq. 1.36 then leads to

$$J_R''(\omega) = h_J \omega G''(\omega) = h_J \chi''(\omega). \tag{1.37}$$

Again, the structural relaxational part of the longitudinal acoustic compliance, J_R'' follows the universal β-susceptibility spectrum $\chi''(\omega)$ in the β-relaxation regime.

1.2.2.4 The Critical Dynamics

With the factorization approximation of Eq. 1.29, Eq. 1.20 reduces to

$$\sigma - \delta t + \lambda G^2(t) = \frac{d}{dt} \int_0^t dt' G(t - t') G(t'), \tag{1.38}$$

where δ denotes the thermally activated hopping rate, and λ ($\frac{1}{2} < \lambda < 1$) is called the exponent parameter. The common β correlator $G(t)$ or the corresponding dynamical susceptibility $\chi''(\omega)$ is the solution of Eq. 1.38.

In the lowest order approximation of the power series expansion, the master function $G(t)$ takes explicit asymptotic forms. For $t \ll t_\sigma, G(t)$ follows the same power law on both sides of the ideal glass transition point, i.e. $G(t) = \sqrt{|\sigma|}(t_\sigma/t)^a$. For $t \gg t_\sigma$, $G(t)$ asymptotes to a constant $\sqrt{|\sigma|(1 - \lambda)}$ in the glass state and it

Table 1.1: Exponents a and b as a function of the exponent parameter λ

λ	a	b	λ	a	b
0.95	0.155	0.200	0.50	0.395	1.00
0.90	0.209	0.303	0.45	0.409	1.10
0.85	0.248	0.392	0.40	0.422	1.22
0.80	0.279	0.476	0.35	0.433	1.34
0.75	0.305	0.558	0.30	0.445	1.48
0.70	0.327	0.641	0.25	0.455	1.66
0.65	0.347	0.725	0.20	0.465	1.84
0.60	0.364	0.725	0.15	0.474	2.09
0.55	0.380	0.903	0.10	0.483	2.43

diverges according to a critical law $-\sqrt{|\sigma|}(t/t_\sigma)^b$ in the liquid state. The time scale t_σ which denotes the onset of the α relaxation is governed by the scaling law

$$t_\sigma = \omega_\sigma^{-1} = t_0|\sigma|^{-1/2a}, \tag{1.39}$$

and the two exponents a and b are determined by the single material-dependent parameter λ through the relation:

$$\begin{aligned} \lambda &= \frac{\Gamma^2(1+b)}{\Gamma(1+2b)} \qquad 0 < b \le 1 & (1.40) \\ &= \frac{\Gamma^2(1-a)}{\Gamma(1-2a)} \qquad 0 < a \le 1/2. & (1.41) \end{aligned}$$

Here $\Gamma(x)$ denotes the gamma function. Table 1.1 lists the characteristic exponents a and b as a function of λ.

Therefore for $T \le T_c$, density correlations initially decay through β relaxation described by the critical law and then arrest at a finite value,

$$\phi_q(t) = \begin{cases} f_q^c + h_q\sqrt{|\sigma|}(t_\sigma/t)^a & t_0 \ll t \ll t_\sigma, \\ f_q^c - h_q\sqrt{|\sigma|}/\sqrt{1-\lambda} & t_0 \ll t_\sigma \ll t. \end{cases} \tag{1.42}$$

Equivalently the dynamical susceptibility χ'' crosses over from the critical power law behavior $\chi''(\omega) \propto h_q\sqrt{|\sigma|}(\omega/\omega_\sigma)^a$ to a linear ω dependence. This gives rise to a knee in the $\log \chi''$ versus $\log \omega$ plot close to the scaling frequency ω_σ.

Above T_c in the liquid state, $\phi_q(t)$ obeys a power law on the short time scales and another power law, the von Schweidler law on longer time scales,

$$\phi_q(t) = \begin{cases} f_q^c + h_q\sqrt{\sigma}(t_\sigma/t)^a & t_0 \ll t \ll t_\sigma \ll \tau_\alpha, \\ f_q^c - h_q\sqrt{\sigma}(t/t_\sigma)^b & t_0 \ll t_\sigma \ll t \ll \tau_\alpha. \end{cases} \tag{1.43}$$

So the corresponding susceptibility χ'' takes the form

$$\chi_q''(\omega) \propto \begin{cases} h_q\sqrt{\sigma}(\omega/\omega_\sigma)^a & \tau_\alpha^{-1} \ll \omega_\sigma \ll \omega \ll t_0^{-1}, \\ h_q\sqrt{\sigma}(\omega/\omega_\sigma)^{-b} & \tau_\alpha^{-1} \ll \omega \ll \omega_\sigma \ll t_0^{-1}. \end{cases} \tag{1.44}$$

The susceptibility therefore exhibits a minimum around ω_σ in the $\chi''(\omega)$ curve. This susceptibility minimum is often described by the MCT interpolation equation,

$$\chi_q''(\omega) = \chi_{\min}'' \frac{b(\omega/\omega_{\min})^a + a(\omega_{\min}/\omega)^b}{a+b}, \tag{1.45}$$

where $\chi_{\min}'' \propto \sqrt{|\sigma|}$, and $\omega_{\min} \propto \omega_\sigma \propto |\sigma|^{1/2a}$. This interpolation is equivalent to a similar interpolation formula for the time dependent correlation function:

$$\phi_q(t) - f_q^c = h_q\sqrt{|\sigma|}\left[b\left(t_i^\beta/t\right)^a - a\left(t/t_i^\beta\right)^b\right], \tag{1.46}$$

where t_i^β denotes a time before which the β relaxation follows the critical law, while after which the initial part of the α relaxation decays via the von Schweidler law.

In the extended MCT, the hopping rate δ is finite and positive. The β-correlator $G(t)$ thus depends on both the separation parameter σ and the hopping rate δ. The one-parameter (σ) scaling in the idealized MCT is replaced by a two-parameter (σ, δ) scaling. As a consequence, the dynamics are modified. The most obvious differences occur at long times or low frequencies for temperatures close to and below T_c. Both the α peak and the minimum in $\chi''(\omega)$ exist in the extended MCT, but not in the idealized MCT. In the transition regime for T near T_c, the cage effect and the hopping effect provide comparable contributions. The hopping contributions modify the low-frequency wing of the idealized MCT β-spectrum so that, with decreasing T, the slope of the low frequency part (below the minimum) of the β-susceptibility spectrum becomes steeper. At temperatures well below T_c in the glass-like regime, the hopping effect dominates the dynamics. Since at high temperatures $\delta \ll \omega|\sigma|$, both versions of MCT are essentially indistinguishable for temperatures well above T_c. Therefore, Eqs. 1.27, 1.43-1.46 for T above T_c are still valid as good first approximations in the extended MCT.

With the definition of the nonergodicity parameter or the Debye-Waller factor $\tilde{f}_q$, Eq. 1.26 also survives in the extended MCT, although with rounding of the cusp around T_c. Thus Eq. 1.26 should still be used to locate the crossover temperature. In the extended MCT, the crossover temperature T_c marks a change in the nature of α relaxation. The α relaxation dynamics are controlled primarily by anharmonic processes above T_c and by activated hopping processes below T_c.

1.3 Some Previous Experimental Results

The study of viscous liquids and the liquid-glass transition has been pursued extensively for over 100 years [31]. Relaxation in glass forming liquids has been observed in many different response functions: neutron scattering [2, 3], frequency-dependent specific heat [4], dielectric loss [4-7], photon correlation [11, 12], light scattering [8, 32-36], longitudinal and transverse acoustic wave propagation [37], NMR [38, 39], and many more. While most dynamics studies have been concerned with motion on a time scale between 10^{-6} s and macroscopic times (say 10^2 s) around T_g, much of the recent effort has been shifted toward examination of the dynamics on fast time scales (from 1 MHz to 1 THz) to test the mode coupling theory predictions as well as empirical and heuristic models. In this section we review some of experimental results which bear on the mode coupling theory of the liquid-glass transition.

Mode coupling theory describes the liquid-glass transition scenario as a purely dynamic crossover from liquid-like (ergodic) to solid-like (glassy, nonergodic) behavior. The crossover is expected to occur at some critical temperature T_c of the supercooled liquid state, located at somewhere above T_g. The Debye-Waller factor $f_q(T)$ shows a square-root cusp (see Eq. 1.26) at T_c.

1.3.1 Neutron Scattering

Among the very first experimental data published in support of the crossover phenomena of MCT are neutron scattering measurements of the Debye-Waller factor $f_q(T)$, the height of the plateau in the correlation function $\Phi(q,t)$. As shown in figure 3 of Ref. [40], the data from fragile glass formers, $Ca_{0.4}K_{0.6}(NO_3)_{1.4}$ (CKN), o-terphenyl, and polybutadiene exhibit the square-root law at a crossover temperature T_c. For the intermediate system glycerol no crossover has been observed. However, as pointed out by the authors themselves [41], caution needs to be taken to interpret the CKN data, which do not show an obvious cusp. It was argued that for CKN the α relaxation has already moved in the experimental window at temperatures close to T_c. As a result $\Phi(q,t)$ begins to fall within the experimental window and there is no pronounced plateau, which makes the reading of f_q difficult. This problem is similar to the one of the cutoff frequency encountered in energy-resolved neutron scattering as discussed in Sec. 1.1.3.

1.3.2 Light Scattering

It has been shown that f_q in the low-q limit can be determined from the relation [42]

$$f_{q\to 0} = 1 - (c_0/c_\infty)^2, \tag{1.47}$$

where c_∞ (c_0) is the limiting sound velocity measured at frequencies well above (below) the α relaxation frequency range. The significance of Eq. 1.47 is two-fold. First, it provides an alternative experimental approach to test the MCT prediction of Eq. 1.26. In addition, it allows one to test the possible q-dependence of T_c, since cusp-like behavior can be sought in the T-dependence of $f_{q\to 0}$ as well as the Debye-Waller factor at high wavevector determined through neutron scattering.

The temperature T_c should be independent of wavevector q because, as shown in Eq. 1.26, it marks the onset of nonergodic behavior for density fluctuations at all wavevectors. The two limiting velocities and subsequently the value of $f_{q \to 0}$ can be measured by ultrasonics or Rayleigh-Brillouin scattering (BS). However, ultrasonics or mechanical measurements are suitable only for determination of c_0, but not c_∞, in the temperature range around T_c. Rayleigh-Brillouin scattering cannot determine both c_0 and c_∞ either. Even a determination of c_∞ from the positions of the Brillouin peaks is often impossible because the highest scattering wavevectors accessible with visible light do not yield sufficiently high acoustic frequencies. Therefore one cannot make a unique determination of T_c through Eq. 1.47 from acoustic measurements and Rayleigh-Brillouin scattering alone. That is the reason that the BS value of T_c determined for propylene carbonate [43] exceeded that determined through neutron scattering [44] by 60K. In other cases [45, 46], BS spectra have not been used for a unique determination but have been found to be consistent with values of T_c determined through neutron scattering measurements of $f_q(T)$ and depolarized light scattering susceptibility spectra [10] (which, as discussed below, provide a separate, dynamical route to T_c, not involving the Debye-Waller factor). Clearly more tests of Eq. 1.26 are necessary, especially in the low-q limit.

Other experimental evidence in support of MCT comes from comprehensive studies of depolarized light scattering from glass forming liquids [8, 47]. Figure 1-2 shows DLS susceptibility spectra of salol at several temperatures and the extended MCT fits. The T-sensitive α relaxation peak moves from high frequency at high temperatures to low frequency at low T until it shifts out of the experimental frequency range. Minima are observed above 253K in the susceptibility spectra. Around the minimum region, the dynamics follow the critical power laws which are represented by the solid lines in Fig. 1-2. The extended MCT analysis predicts that there exist minima in $\chi''(\omega)$ for T below 253K, which fall below the spectral region available. Data in this region are needed to allow a complete test of the MCT.

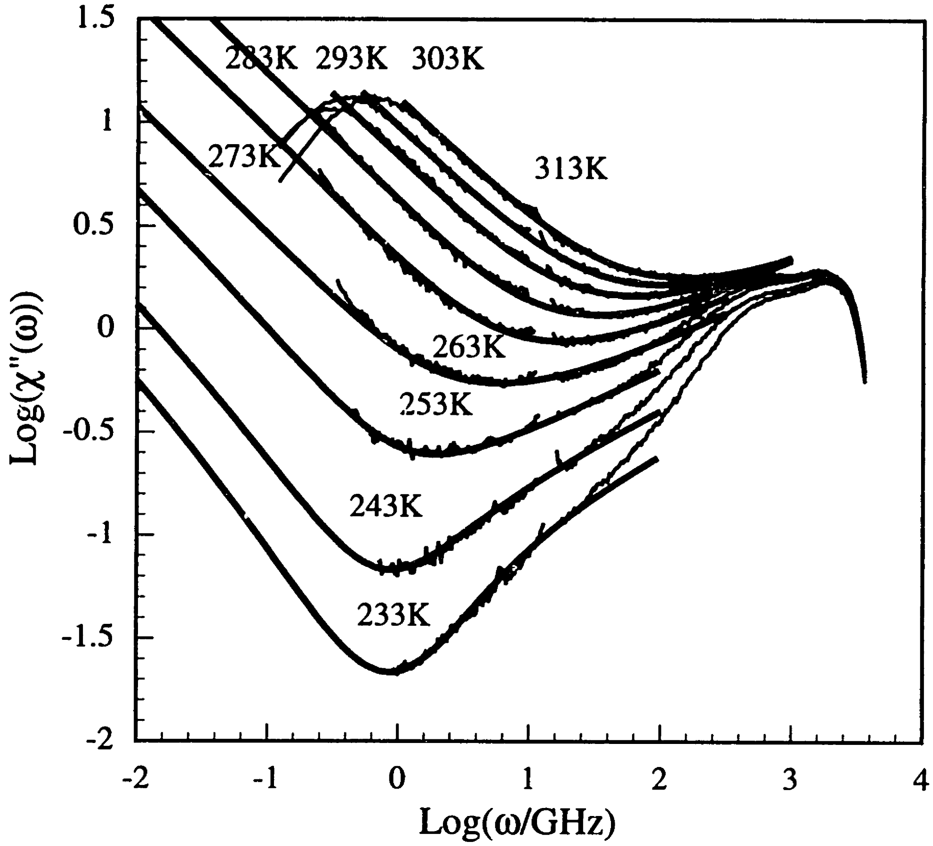

Figure 1-2: Susceptibility spectra $\chi''(\omega)$ of salol from 313K to 218K. The solid lines represent the extended MCT fits with the exponent parameter $\lambda = 0.73$.

1.4 Overview of the Thesis

In this thesis, we shall describe one of the applications of impulsive stimulated light scattering in the research of the liquid-glass transition. It covers a time window from sub-nanoseconds to many milliseconds, which makes it suitable for examination of the dynamics of liquid-glass transitions. We shall first present the experimental technique, and then give a detailed theoretical description of the technique. Following that we present applications of the technique to two glass forming liquids and analyses of the experimental data to test the predictions of the mode coupling theory.

Chapter 2 contains a description of the implementation of the ISS technique. The excitation mechanisms and a comparison of two probe systems will be discussed.

In Chapter 3, we present a generalized hydrodynamics approach to impulsive stimulated light scattering from glass-forming liquids. The generalized hydrodynamics equations, including nonlocal behavior in time, are used to calculate density response functions of ISS. Single-exponential relaxation dynamics are considered first, and then the results are generalized to account for complex relaxation. Thermal diffusion, acoustic, and relaxation modes are described. The time dependence of both acoustic and relaxation modes yields the structural relaxation dynamics. In addition, the relative amplitudes of the modes in ISS data yield the Debye-Waller factor f_q in the limit of low wavevector q. This permits testing of MCT predictions of a square-root cusp in the temperature dependence of $f_{q\to 0}(T)$ at a crossover temperature T_c. The information which can be obtained through ISS is compared in theoretical and practical terms to that obtainable through low-frequency Rayleigh-Brillouin scattering spectroscopy.

The remainder of the thesis is devoted to ISS experimental studies of two different glass formers. Chapter 4 contains an investigation of the structural relaxation dynamics of the organic glass former salol. In Chapter 5, we present results of another ISS study of the ionic glass former $Ca_{0.4}K_{0.6}(NO_3)_{1.4}$.

In Chapter 6, we further examine the longitudinal acoustic dynamics revealed in the ISS study of salol. Longitudinal acoustic velocities and damping rates are measured in the MHz-GHz range, from which the longitudinal modulus spectra and the compliance spectra are derived in the intermediate temperature range. The observed α relaxation peaks are analyzed in terms of an empirical (KWW stretched exponential) relaxation function. The high-frequency wings of the α relaxation peaks are compared to the susceptibility spectra from depolarized light scattering and the extended mode coupling theory predictions.

Chapter 7 contains some data on orientational relaxation dynamics of salol and partial data analysis. They are measured in ISS experiments with depolarized (VHVH) geometry. Further experiments to cover a wider dynamical range are suggested.

In Chapter 8 we summarize our findings and draw conclusions from the results we shall present in this thesis. Suggestions for possible future experiments and improvements of the technique are also presented.

Chapter 2

Impulsive Stimulated Light Scattering Technique

2.1 Introduction

Impulsive stimulated light scattering is a time-resolved optical spectroscopy method. It has been shown to be very powerful for following the acoustic dynamics of glass-forming liquids in the frequency range from 10 MHz to 10 GHz [33, 48-53]. Recently its dynamical range has been extended to cover sub-nanosecond through millisecond time scales, well suited for investigation of the dynamics in supercooled liquids. Also this method has recently been applied to examination of mechanical and thermal properties of polymer and other thin films [54-57]. In this Chapter we describe the details of the experimental implementation of the ISS technique.

2.2 The Technique

Impulsive stimulated light scattering is a time-delayed four-wave mixing or "transient grating" experiment. A schematic illustration of ISS experiment as conducted this thesis is shown in Fig. 2-1. Two parallel-polarized, picosecond excitation pulses of wavelength λ_E are crossed at an angle of intersection θ_E and overlapped spatially and temporally inside the sample. Optical interference of these two pulses creates

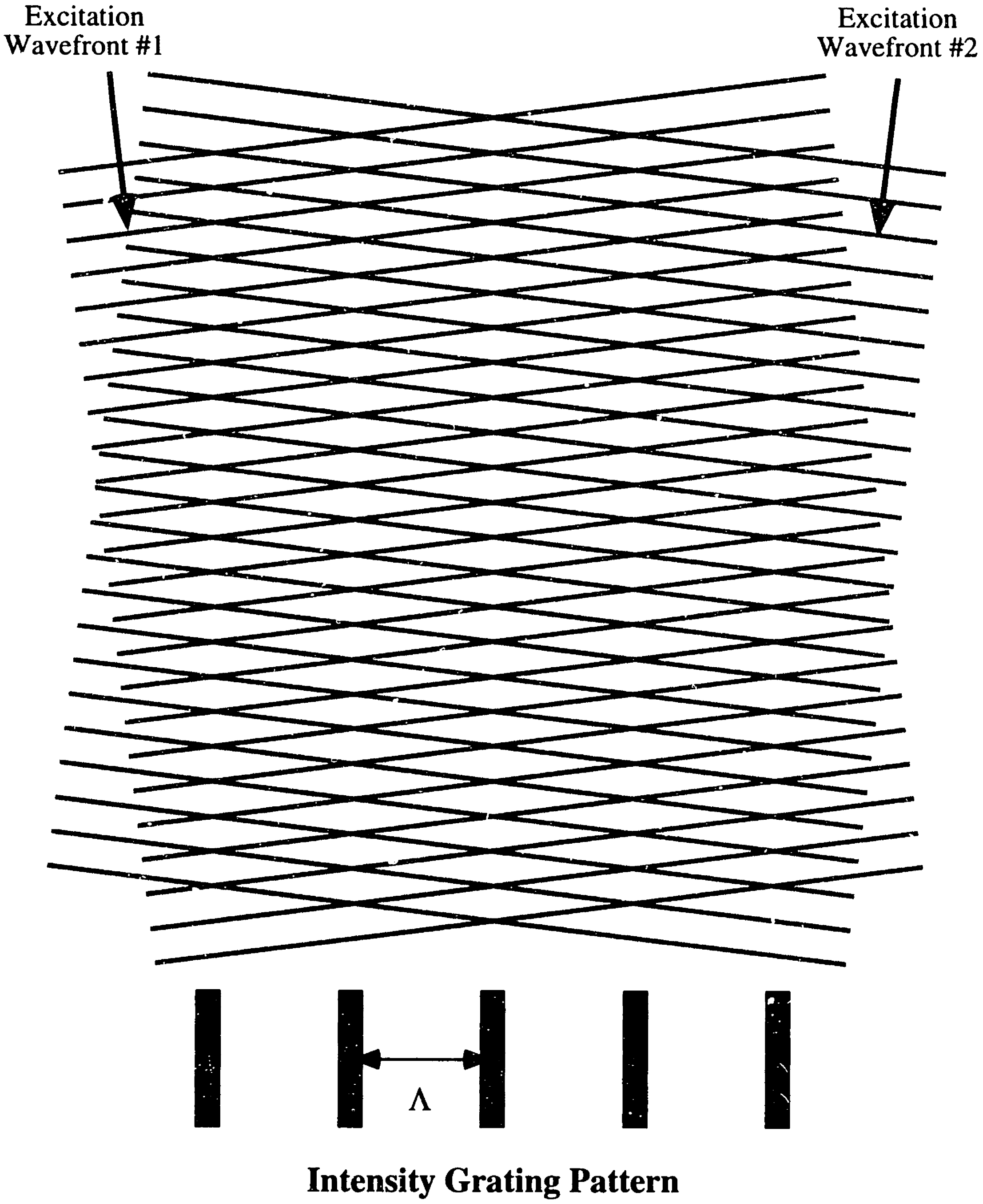

Figure 2-1: Formation of the interference grating pattern by crossing two excitation pulses.

an intensity grating pattern with wavevector magnitude

$$q = \frac{4\pi \sin(\theta_E/2)}{\lambda_E} = \frac{2\pi}{\Lambda}, \tag{2.1}$$

where Λ is the interference fringe spacing. The interaction of the field with the matter generates phase-coherent material excitations with the same wavevector q. When a third probe beam is incident at the phase-matching (Bragg) angle for the grating, part of the probe light will be diffracted in a direction with the mirror symmetry of the transmitted probe light. The time dependence of the material excitations is obtained by recording the diffraction efficiency as a function of the time delay between the pump and probe pulses with a variably-delayed short probe pulse, or time-resolving the diffracted probe light electronically with CW or quasi-CW probe system.

The excitation pulses can interact with the sample in two ways of interest here. First, acoustic modes can be excited through impulsive stimulated Brillouin scattering (ISBS). In this mechanism, the electric field exerts a sudden ("impulsive") electrostrictive stress at the excitation wavevector, launching two counterpropagating acoustic waves with wavevectors $\pm q$. Second, absorption of the excitation light by the sample can occur. For absorbing materials, optical absorption at the intensity peaks and subsequent rapid thermalization lead to the sudden formation of a temperature grating with wavevector q. Thermal expansion due to this impulsive, spatially periodic heating then results in a time-dependent density response at this wavevector. This process is referred to as impulsive stimulated thermal scattering (ISTS). In simple cases like normal liquids, the sample density overshoots and oscillates about the steady-state level. After the acoustic oscillations are fully damped, the steady-state density modulation decays due to thermal diffusion. Thus the acoustic mode can be excited through ISTS in addition to the thermal diffusion mode. In the following Chapters, we will discuss more complicated systems like complex liquids, in which the materials responses include an additional relaxation mode besides the acoustic and thermal diffusion modes.

As far as excitation of acoustic dynamics is concerned, there is no difference between the ISBS and ISTS mechanisms. Both of them give the same acoustic frequency and damping rate. Note that the acoustic mode can always be excited through ISBS for absorbing or non-absorbing materials, while only absorbing materials give ISTS signal. This is because ISTS depends on optical absorption by the sample at the excitation laser wavelength and subsequent rapid heating at the intensity grating peaks to suddenly generate the temperature grating. However, ISTS provides much more information than ISBS, which will be discussed in detail in the next Chapter. In practice, ISTS signal is much stronger than ISBS signal with the same excitation laser intensity even for weakly absorbing materials, except at very large wavevectors where the ISBS contribution may be no longer negligible, as will be shown in the next Chapter.

2.3 Experimental Setup

2.3.1 The Quasi-CW Probe System

Experiment implementation of ISS with a quasi-CW probe system is schematically shown in Fig. 2-2. The excitation pulses are derived from the output of a Q-switched, mode-locked, and cavity-dumped Nd:YAG laser which yields a pulse of about 500 μJ energy and 100 ps duration at a repetition of up to 1 kHz [58, 59]. The pulse is split with a 50% beam-splitter into two excitation pulses that are cylindrically focused and crossed at an excitation angle (in air) θ_E. These two pulses are temporally and spatially overlapped inside the sample by adjusting the relative path lengths and mirror positions. Typically, the laser spots are about 100 μm high and 5 mm wide at the focus. The large width is necessary so that the laser-generated acoustic waves observed in ISS do not leave the excitation region before they are fully damped.

The probe beam is derived from a single-mode CW Argon laser (Lexel, 1 W average power). The output of the Argon laser is electro-optically gated with an adjustable duration from several hundreds of nanoseconds to many seconds. The

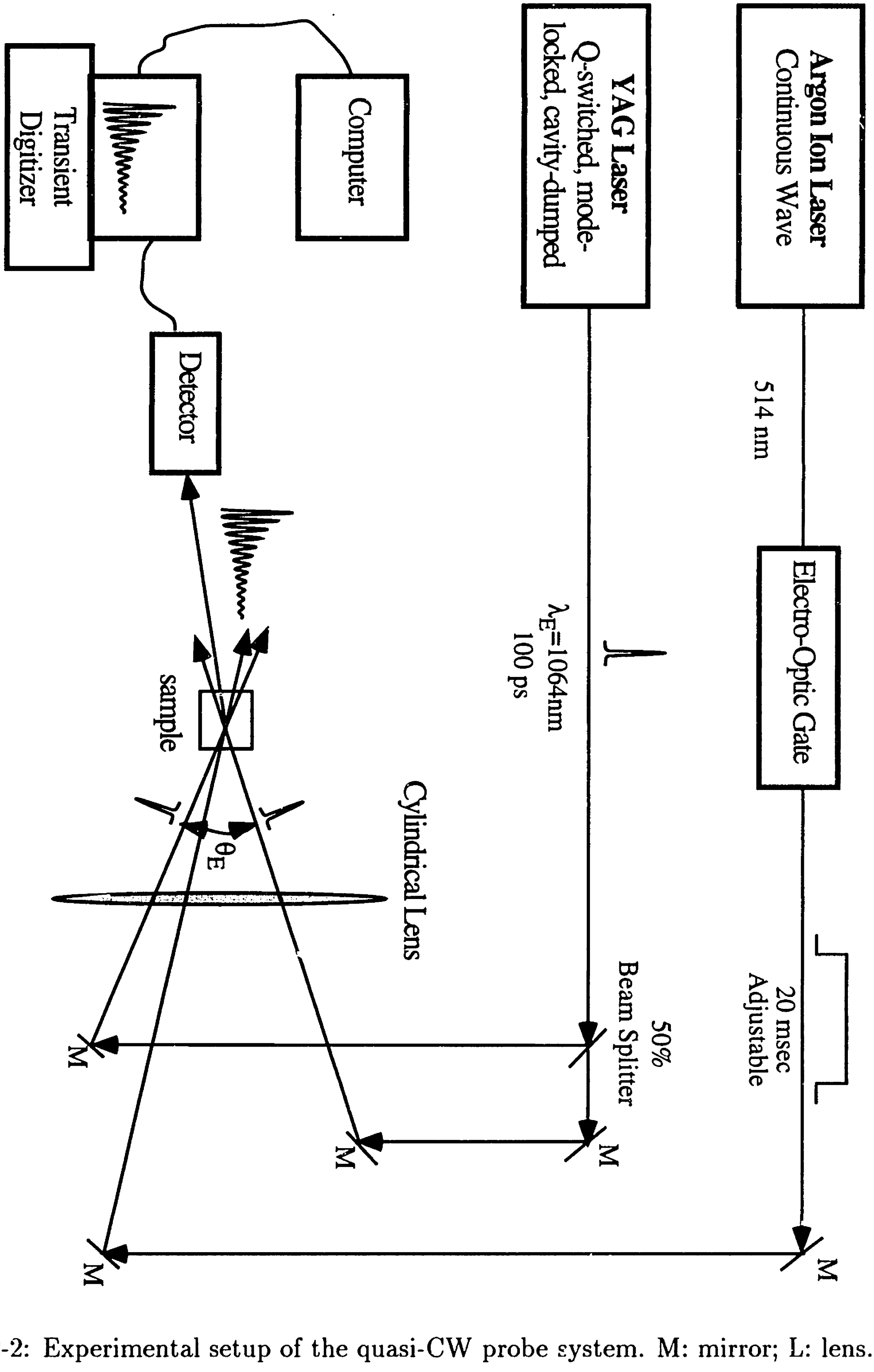

Figure 2-2: Experimental setup of the quasi-CW probe system. M: mirror; L: lens.

duration of the probe light is selected such that it is just long enough to detect the excited material dynamics with each pump laser shot. Therefore the probe light is incident on the sample only for a short period of time, which is often necessary to avoid sample blooming. The quasi-CW probe light is focused first by a cylindrical lens horizontally and then by another (also used for the excitation beams) vertically in the center of the grating. Diffracted signal is directed into an amplified fast photodiode (Antel Co., 2GHz bandwidth) whose output is processed by a digitizing oscilloscope (Tektronix DSA, 1GHz bandwidth). The digitized signal is transferred to a computer for storage and subsequent analysis.

This system has several useful features. Of primary importance are the wide ranges of scattering wavevectors q and time scales (from 1 ns to many milliseconds) which are accessible. Also important in practice is the fact that the entire temporal response is recorded in a single laser shot, and very high signal-to-noise (S/N) ratios can be realized with several seconds of signal averaging. Typically, data from 1000 shots are recorded and averaged in about 10 seconds.

2.3.2 The Pulse Probe System

Excitation at large wavevectors (large excitation angles) results in acoustic frequencies exceeding the 1-GHz bandwidth of the detection electronics in the quasi-CW probe system described above. In this case, the acoustic data can be collected with a pulse probe system. In this system, the excitation pulses are generated and overlapped inside the sample in the same way as in quasi-CW probe system, and the probe pulse is derived from a second mode-locked and Q-switched Nd:YAG laser. Its output consists of a train of 100 ps, 1.064 μm pulses. The largest pulse is selected electro-optically by a Pockel's cell and then frequency-doubled to yield 532 nm probe light. This probe pulse is incident upon the center of the grating at Bragg angle. (Fig. 2-3). The timing delay between excitation and probe pulses is controlled electronically by shifting the phase of common mode-locker radio-frequency (rf) source to the probe laser and by electronically delaying the appropriate amount of timing of the Q-switches and the single pulse selector concurrently [58, 59].

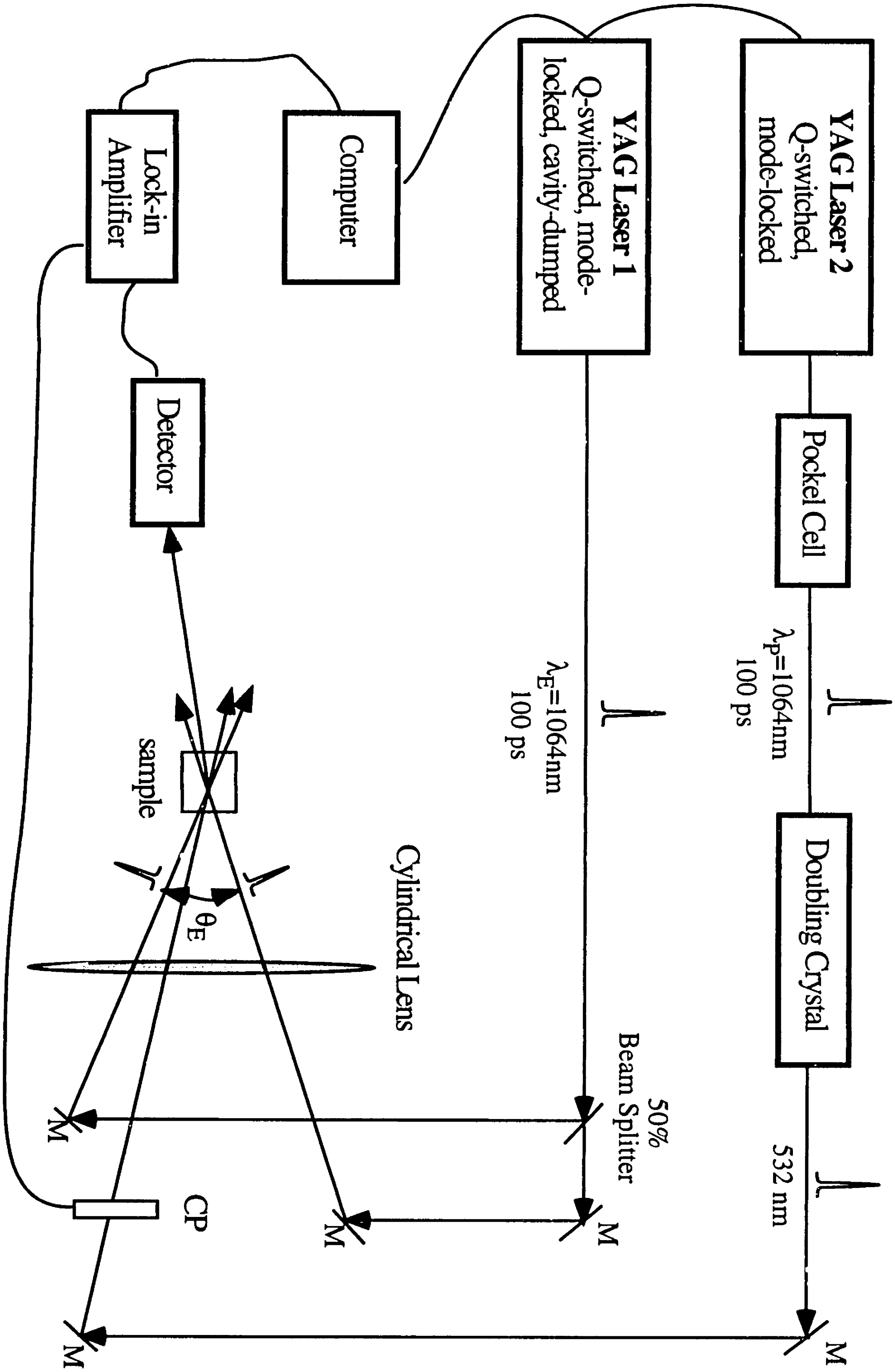

Figure 2-3: Experimental setup of the pulse probe system. M: mirror; L: lens; CP: Mechanical Chopper.

The signal beam is directed into a low-bandwidth amplified photodiode. The output of the photodiode is sent to a lock-in amplifier whose reference frequency is synchronized with a mechanical chopper running at an arbitrary frequency less than the laser repetition rate. The mechanical chopper is placed in the probe beam in order to reduce scattered light due to the excitation beams. The lock-in is connected through a general purpose interface bus (GPIB) interface to a personal computer, which also controls the time delay of the probe pulse. For each given delay time between the excitation and probe pulses, the computer records the diffracted signal intensity from the lock-in amplifier. Usually, the lock-in time constant is set to 100 ms, and the data are averaged over 20 consecutive sweeps over the whole time range. In this way the data are recorded "point by point" on the time axis and the time resolution is limited only by the pulse duration. Besides its higher time resolution than that of the CW probe system, the pulse probe system also has higher sensitivity. This is because the ISS signal level is proportional to the peak power in the probe beam and the peak power of the CW probe beam is much lower than that of the pulse probe beam. However, the S/N of the pulse probe system is generally lower than that of the quasi-CW probe system, since laser intensity fluctuations contribute to noise in the former. In addition, the data collection time is far longer (typically 10-30 minutes) in the pulse probe system since each laser shot yields just on point on the time axis rather than the entire temporal response.

2.4 Discussion

Both pulse and CW probe systems, in principle, can be used to detect ISBS or ISTS signal. But due to the very weak ISBS signal level, especially at low wavevector, and due to the low sensitivity of the CW probe system, it is often impossible to use the CW system for non-absorbing samples. In this case, the pulse probe system has to be used. However, ISTS signal intensity is usually strong enough to use the CW probe system so that one can take advantage of its superior signal to noise ratio, fast data acquisition rate, and wide dynamical range. Also ISTS yields not only acoustic dynamics as does ISBS, but also long-lived thermal diffusion dynamics as well as structural relaxation information. Therefore, generally ISTS is preferable to ISBS. To create ISTS signal, one has to choose the excitation laser wavelength so that the sample will weakly absorb the excitation light, or add into the sample a small amount of a strongly absorbing guest. Introduction of guests must be done judiciously, however, to avoid guest relaxation dynamics from contributing to the signals observed.

For acoustic oscillations excited by ISTS with frequencies above 1 GHz, as an alternative to pulse probe detection, a streak camera has recently become available as signal detector which has much higher time resolution ($\sim 2\, ps$) than the combination of the fast photodiode and transient digitizer. In this case, two different detection systems have to be utilized, the streak camera detection for fast acoustic dynamics, and the fast photodiode and transient digitizer detection for long time dynamics. The two sets of data are then combined to give the complete ISTS response.

Chapter 3

Generalized Hydrodynamics Theory of ISS from Glass-Forming Liquids

3.1 Introduction

In this Chapter[1] a generalized hydrodynamics analysis of impulsive stimulated light scattering is presented. In the ISS experiment, the time-dependent density response to crossed laser pulses which produce sudden heating (in ISTS) or sudden stress (in ISBS) is measured. The information content of ISS data is analyzed in detail for the cases of simple (single-exponential) or complex (nonexponential) structural relaxation dynamics. There appear thermal diffusion, acoustic, and structural relaxation modes in ISS data, which are time-dependent analogs of Rayleigh, Brillouin, and Mountain modes which appear in Rayleigh-Brillouin scattering (BS) spectra of complex fluids. In addition to their dynamics, the relative amplitudes of thermal diffusion, acoustic, and structural relaxation modes in ISTS data are shown to yield the value of the Debye-Waller factor, $f_q(T)$ in the low-wavevector limit. This permits testing of MCT predictions of the temperature dependence of $f_{q\to 0}(T)$.

---

[1] Some of the materials in this Chapter have been published in Ref. [60].

In Sec. 3.2, formal ISS response functions are given for any relaxation kernel form based on the generalized hydrodynamics equations. In Sec. 3.3 we present a detailed analysis of the ISS response functions for a single-relaxation-time process. The results for the Debye model are generalized for a stretched exponential relaxation function in Sec. 3.4.

A comparison of ISS to BS is presented in the context of measurements on glass-forming liquids in Sec. 3.5. In some cases the time-domain approach offers significant advantages which permit elucidation of complex relaxation dynamics and testing of mode-coupling theoretical predictions in ways which are difficult through frequency-domain light scattering spectroscopy. Particularly important are the capabilities in ISS of conducting measurements with a wide range of excitation angles or wavevectors and over a wide range of time scales. ISS and BS are compared with respect to information content which can be extracted in principle and in practice.

In Sec. 3.6, the generalized hydrodynamics equations for ISS are shown to be essentially the same as the MCT equations. Thus one can in principle calculate the ISS response functions by using the MCT relaxation kernel. ISS response function then should reveal the β relaxation dynamics in short time scales preceding the α relaxation. The conclusions are given in Sec. 3.7.

3.2 Generalized Hydrodynamics Equations for ISS

The general theory for impulsive stimulated light scattering has been developed in detail [61]. In the limit of ideal time resolution, ISS signal intensity is given by

$$I(q,t) = \left|-F_0 G_{\rho\rho}(q,t) + Q_0 G_{\rho T}(q,t)\right|^2 , \tag{3.1}$$

where $G_{\rho\rho}(q,t)$, the density-density response function, gives the time-dependent density response of the sample to laser-induced electrostrictive stress (of magnitude proportional to F_0), and $G_{\rho T}(q,t)$ gives the density response to laser-deposited heating of extent proportional to Q_0. Note that the response to heating might be expressed in terms of $G_{\rho S}$, the density-entropy correlation function, but as discussed below the specific heat connecting temperature to entropy is treated as a frequency-independent quantity; all the complex (frequency-dependent) behavior is described by the complex elastic modulus and viscosity.

For samples which are transparent at the excitation wavelength, there is no heating. So the signal contribution from $G_{\rho\rho}(q,t)$ dominates ISS signal, i.e. the density response is driven directly through impulsive simulated Brillouin scattering. Therefore for ISBS, the signal intensity is

$$I_{BS}(q,t) = |F_0 G_{\rho\rho}(q,t)|^2 . \tag{3.2}$$

For materials which absorb the excitation wavelength, heat is deposited into the sample in a spatially varying pattern and thermal expansion produces the density response. The scattering process in this case is impulsive stimulated thermal scattering and $G_{\rho T}(q,t)$ is the dominating term, i.e. the signal intensity is

$$I_{TS}(q,t) = |Q_0 G_{\rho T}(q,t)|^2 . \tag{3.3}$$

The response functions $G_{\rho\rho}(q,t)$ and $G_{\rho T}(q,t)$ for simple liquids have been derived previously based on ordinary hydrodynamics equations [59]. Here we start with generalized hydrodynamics equations and calculate the density response functions for complex liquids. The basic generalized hydrodynamics equations in q-space [27] are the continuity equation

$$\frac{\partial \delta\rho(q,t)}{\partial t} - \rho_0 i q v_{||}(q,t) = 0, \tag{3.4}$$

and the generalized Navier-Stokes equation

$$\begin{aligned} \rho_0 \frac{\partial v_{||}(q,t)}{\partial t} - iq\frac{k_B T_0}{S(q)}\delta\rho(q,t) - iq\frac{k_B T_0}{S(q)}\rho_0 \kappa \delta T(q,t) & \\ + \rho_0 q^2 \int_0^t dt' \phi_L(q,t-t') v_{||}(q,t') &= iqF(q,t), \end{aligned} \tag{3.5}$$

and the energy-transport equation

$$\rho_0 c_v \frac{\partial \delta T(q,t)}{\partial t} - c_v \frac{\gamma - 1}{\kappa} \frac{\partial \delta\rho(q,t)}{\partial t} + \lambda q^2 \delta T(q,t) = Q(q,t), \tag{3.6}$$

where κ is the thermal expansion coefficient, $\gamma = c_p/c_v$ the specific heat ratio, λ the thermal conductivity coefficient, ρ_0 the equilibrium density, and T_0 the equilibrium temperature. The electrostrictive pressure due to the laser pulses and the heating rate per unit volume due to absorption of laser light are denoted by $F(q,t)$ and $Q(q,t)$, respectively. $\phi_L(q,t)$ is a memory function representing the retarded response of the current to a change in the stress tensor and $S(q)$ is the structure factor. Note that only the compressibility and the longitudinal viscosity are generalized, whereas the thermal conductivity and specific heat are not modified. In the limit $\phi_L(q,t) = \delta(t)$ and $\lim_{q\to 0} k_B T/S(q) = (\partial\rho/\partial p)_T^{-1} = \gamma^{-1}c_0^2$ where c_0 is the adiabatic sound velocity, Eqs. 3.4-3.6 reduce to the ordinary linearized equations. Because the transverse part of the velocity is not coupled to the density in this linearized theory, we have not included the transverse part of the Navier-Stokes equation here. This has been treated in connection with depolarized ISBS experiments on shear waves in glass-forming liquids [51]. Since we are interested in the density response, the velocity component $v_{\|}(q,t)$ in Eq. 3.5 can be eliminated by using Eq. 3.4. One can then derive two simultaneous linear equations for the density response $\delta\rho(q,s)$ and temperature response $\delta T(q,s)$ through Laplace transformation:

$$\begin{aligned}\left[\frac{s^2}{q^2} + s\phi_L(q,s) + \frac{k_B T_0}{S(q)}\right] \delta\rho(q,s) + \left[\rho_0 \kappa \frac{k_B T_0}{S(q)}\right] \delta T(q,s) \\ = -F(q,s) + \delta\rho(q)\left[s/q^2 + \phi_L(q,s)\right]\end{aligned} \tag{3.7}$$

and

$$\begin{aligned}\left[-\frac{s(\gamma-1)c_v}{\kappa}\right] \delta\rho(q,s) + \left[\rho_0 c_v s + \lambda q^2\right] \delta T(q,s) \\ = Q(q,s) - \delta\rho(q)\frac{(\gamma-1)c_v}{\kappa} + \delta T(q)\rho_0 c_v.\end{aligned} \tag{3.8}$$

Here $\delta\rho(q)$ and $\delta T(q)$ are the initial values

$$\delta\rho(q) = \int_v d\mathbf{r}\exp(-i\mathbf{q}\cdot\mathbf{r})\delta\rho(\mathbf{r},0), \tag{3.9}$$

$$\delta T(q) = \int_v d\mathbf{r}\exp(-i\mathbf{q}\cdot\mathbf{r})\delta T(\mathbf{r},0), \tag{3.10}$$

which are necessary to construct the spontaneous light scattering spectrum. Equations 3.7 and 3.8 can be rewritten in a matrix form

$$\begin{pmatrix} \frac{s^2}{q^2} + s\phi_L(q,s) + \frac{k_B T_0}{S(q)} & \rho_0\kappa\frac{k_B T_0}{S(q)} \\ -\frac{s(\gamma-1)c_v}{\kappa} & \rho_0 c_v s + \lambda q^2 \end{pmatrix} \begin{pmatrix} \delta\rho(q,s) \\ \delta T(q,s) \end{pmatrix} \tag{3.11}$$

$$= \begin{pmatrix} -F(q,s) + \delta\rho(q)\left\{s/q^2 + \phi_L(q,s)\right\} \\ Q(q,s) - \delta\rho(q)\frac{(\gamma-1)c_v}{\kappa} + \delta T(q)\rho_0 c_v \end{pmatrix}. \tag{3.12}$$

This matrix equation describes the density and temperature responses of the sample to the electrostrictive stress and heat exerted by the excitation laser pulses. It can be expressed in an abbreviated form as

$$LX = F \tag{3.13}$$

where

$$L = \begin{pmatrix} \frac{s^2}{q^2} + s\phi_L(q,s) + \frac{k_B T_0}{S(q)} & \rho_0\kappa\frac{k_B T_0}{S(q)} \\ -\frac{s(\gamma-1)c_v}{\kappa} & \rho_0 c_v s + \lambda q^2 \end{pmatrix}, \tag{3.14}$$

and

$$F = \begin{pmatrix} -F(q,s) + \delta\rho(q)\left\{s/q^2 + \phi_L(q,s)\right\} \\ Q(q,s) - \delta\rho(q)\frac{(\gamma-1)c_v}{\kappa} + \delta T(q)\rho_0 c_v \end{pmatrix}. \tag{3.15}$$

The solutions to Eq. 3.13 are given by

$$X = L^{-1}F = GF \tag{3.16}$$

with

$$G_{\rho\rho}(q,s) = \frac{1}{\Delta}\left\{sq^2 + \frac{\lambda q^4}{\rho_0 c_v}\right\}, \tag{3.17}$$

$$G_{\rho T}(q,s) = \frac{1}{\Delta}\left\{-\frac{\kappa q^2}{c_v}\frac{k_B T_0}{S(q)}\right\}, \tag{3.18}$$

$$G_{T\rho}(q,s) = \frac{1}{\Delta}\left\{-\frac{(\gamma-1)sq^2}{\rho_0 \kappa}\right\}, \tag{3.19}$$

and

$$G_{TT}(q,s) = \frac{1}{\Delta}\left\{\frac{s^2}{\rho_0 c_v} + \frac{q^2}{\rho_0 c_v}\phi_L(q,s)s + \frac{q^2}{\rho_0 c_v}\frac{k_B T_0}{S(q)}\right\}. \tag{3.20}$$

Here

$$\begin{aligned}\Delta &= s^3 + s^2q^2\left\{\phi_L(q,s) + \frac{\lambda}{\rho_0 c_v}\right\} \\ &\quad + s\left\{\frac{\lambda q^4}{\rho_0 c_v}\phi_L(q,s) + \gamma q^2\frac{k_B T_0}{S(q)}\right\} + \frac{\lambda q^4}{\rho_0 c_v}\frac{k_B T_0}{S(q)}.\end{aligned} \tag{3.21}$$

For a density change $\delta\rho(q,s)$, the formal solution is

$$\delta\rho(q,s) = G_{\rho\rho}F_1 + G_{\rho T}F_2. \tag{3.22}$$

We will now calculate the density response functions $G_{\rho\rho}$ and $G_{\rho T}$. Since the changes in temperature described by $G_{T\rho}$ and G_{TT} produce negligible change in the dielectric constant and thus negligible contributions to ISS signal, we will not discuss these two response functions. For ISS, the initial values of Eqs. 3.9 and 3.10 are set to zero. The external forces in the ideal time and wavevector resolution limits can be approximated as delta functions in time and sinusoidal waves in space with specified wavevector q_0, i.e.

$$F(q,s) = F_0\delta(q \pm q_0) \tag{3.23}$$

and

$$Q(q,s) = Q_0\delta(q \pm q_0). \tag{3.24}$$

Substituting Eqs. 3.17, 3.18, 3.23, and 3.24 into Eq. 3.22 and then performing inverse Laplace transformation of the resultant equation, one obtains the time-dependent density variation $\delta\rho(q,t)$ due to laser pulse irradiation:

$$\delta\rho(q,t) = \delta(q \pm q_0)[-F_0 G_{\rho\rho}(q,t) + Q_0 G_{\rho T}(q,t)] \tag{3.25}$$

with

$$G_{\rho\rho}(q,t) = LT^{-1}\left[\frac{1}{\Delta}\left(sq^2 + \frac{\lambda q^4}{\rho_0 c_v}\right)\right] \tag{3.26}$$

and

$$G_{\rho T}(q,t) = LT^{-1}\left[-\frac{1}{\Delta}\left(\frac{\kappa q^2}{c_v}\frac{k_B T_0}{S(q)}\right)\right]. \tag{3.27}$$

Equation 3.25 is the exact solution to Eqs. 3.4-3.6, since no approximations have been made yet. It gives the total density response of ISS for any given memory function $\phi_L(q,t)$ and structure factor $S(q)$, and can, in principle, can be solved numerically.

Here we will take an alternative approach, which is to derive the analytical expressions of $G_{\rho\rho}(q,t)$ and $G_{\rho T}(q,t)$ for a single-exponential relaxation process (Debye model). The results are then generalized to account for complex relaxation processes. Notice that the wavevector magnitude q used in ISS experiments ranges from about 0.05 to 70 μm^{-1} and it is in the low-q or hydrodynamic limit, thus only motions on the macroscopic wavelength $2\pi/q$ need to be considered. In this $q \rightarrow 0$ limit the generalized compressibility becomes the hydrodynamic counterpart, i.e. $\lim_{q\rightarrow 0} k_B T_0/S(q) = c_0^2/\gamma$. Therefore we will replace $k_B T_0/S(q)$ by c_0^2/γ and only consider the generalized bulk viscosity to account for structural relaxational effects probed by ISS.

3.3 Density Response Functions in the Debye Model

3.3.1 Derivation of $G_{\rho\rho}(q,t)$ and $G_{\rho T}(q,t)$

In the Debye approximation, the kinematic viscosity function is $\phi_L(q,t) = \nu_L + \nu_R \exp(-t/\tau_R)$ and it can be identified as

$$\lim_{q\to 0} \phi_L(q,s) = \nu_L + \frac{c_\infty^2 - c_0^2}{1 + s\tau_R}\tau_R = \nu_L + \phi_L^R(q,s). \tag{3.28}$$

Here the frequency-independent part of the longitudinal kinematic viscosity $\nu_L = (\frac{4}{3}\eta_s + \eta_B)/\rho_0$, the relaxing part is $\phi_L^R(q,t)$; and c_∞ and c_0 are the infinite- and zero-frequency sound speed, respectively. Under the conditions $\nu_L q^2 \ll c_0 q$, $\Gamma_H \ll c_0 q$, and $\Gamma_H \tau_R \ll 1$ (with thermal diffusivity $\chi = \Gamma_H/q^2 = \lambda/(\rho_0 c_p)$) the dispersion equation $\Delta = 0$ can be cast into the following form:

$$(s + \Gamma_H)(s + i\omega_A + \Gamma_A)(s - i\omega_A + \Gamma_A)\left[s + \frac{c_0^2}{c_\infty^2 \tau_R}\right] = 0. \tag{3.29}$$

Here

$$\omega_A \equiv c_A q = c_0 q \left[D + \sqrt{D^2 + (c_0 q \tau_R)^{-2}}\right]^{1/2} \tag{3.30}$$

with

$$D = \frac{1}{2}\left[c_\infty^2/c_0^2 - (c_0 q \tau_R)^{-2}\right] \tag{3.31}$$

and

$$\Gamma_A = \underbrace{\frac{1}{2}q^2\left\{(\nu_L + (\gamma - 1)\chi) + \chi(1 - \frac{c_0^2}{c_A^2})\right\}}_{\Gamma_A^B} + \underbrace{\frac{1}{2}q^2\frac{c_\infty^2 - c_0^2}{1 + (\omega_A \tau_R)^2}\tau_R}_{\Gamma_R}. \tag{3.32}$$

In Eq. 3.32 we have separated the background contribution to damping, Γ_A^B, from the part Γ_R which is due to the structural relaxation processes of primary interest. From the dispersion Eq. 3.29, the response functions $G_{\rho\rho}(q,t)$ and $G_{\rho T}(q,t)$ can be calculated to the lowest order to yield

$$
\begin{aligned}
G_{\rho\rho}(q,t) &= \frac{c_A^2 q^2 \tau_R^2 + c_0^2 c_A^{-2}}{c_A^2 q^2 \tau_R^2 + c_0^4 c_A^{-4}} \frac{q}{c_A} e^{-\Gamma_A t} \sin(\omega_A t) \\
&\quad + \frac{(1 - c_0^2 c_A^{-2}) q^2 \tau_R}{c_A^2 q^2 \tau_R^2 + c_0^4 c_A^{-4}} \left[-e^{-\Gamma_A t} \cos(\omega t) + e^{-c_0^2 c_A^{-2} t/\tau_R)} \right], \qquad (3.33)
\end{aligned}
$$

and

$$
G_{\rho T}(q,t) = A \left[e^{-\Gamma_H t} - e^{-\Gamma_A t} \cos(\omega_A t) \right] + B \left[e^{-\Gamma_H t} - e^{-c_0^2 c_A^{-2} t/\tau_R} \right]. \qquad (3.34)
$$

Here

$$
\begin{aligned}
A &= -\frac{\kappa}{c_p} \frac{c_0^2}{c_A^2} \frac{c_A^2 q^2 \tau_R^2 + c_0^2 c_A^{-2}}{c_A^2 q^2 \tau_R^2 + c_0^4 c_A^{-4}}, \qquad (3.35) \\
B &= -\frac{\kappa}{c_p} \frac{q^2 \tau_R^2 (c_A^2 - c_0^2)}{c_A^2 q^2 \tau_R^2 + c_0^4 c_A^{-4}}. \qquad (3.36)
\end{aligned}
$$

In $G_{\rho T}(q,t)$ we have separated the thermal diffusion mode into two terms for later generalization. Equations 3.33 and 3.34 reveal qualitatively most of the features exhibited in ISS experiments on simple and relaxing liquids.

3.3.2 Properties of $G_{\rho\rho}(q,t)$ and $G_{\rho T}(q,t)$

3.3.2.1 Acoustic Mode

Both $G_{\rho\rho}(q,t)$ and $G_{\rho T}(q,t)$ in Eqs. 3.33 and 3.34 contain oscillatory terms, which represent sound propagation in the medium. Thus the acoustic frequency ω_A and damping rate Γ_A can be extracted from ISBS or ISTS measurements. When $\omega_A \tau_R \ll 1$, i.e. very short relaxation time relative to the acoustic period, Eqs. 3.30 and 3.32 become $c_A = c_0$ and $\Gamma_A = [\nu_L + (\gamma - 1)\chi]/2$, respectively. Then Eqs. 3.33 and 3.34 reduce to the ordinary hydrodynamic results for simple fluids [59], i.e. $A = -\kappa/c_p$ and $B = 0$ in $G_{\rho T}(q,t)$, while in $G_{\rho\rho}(q,t)$ the amplitude of the first term is equal to q/c_0 and the second and third terms disappear. The acoustic mode oscillating at frequency $c_0 q$ is weakly damped due to viscosity and thermal diffusion processes. In this limit, energy exchange between the acoustic mode and the relaxational mode can easily occur within the acoustic oscillation period. Structural rearrangement therefore occurs in phase with the acoustic oscillations, and the relaxing fluid behaves like a simple fluid. When $\omega_A \tau_R \gg 1$, we have $c_A = c_\infty$ and $\Gamma_A = [\nu_L + (\gamma - 1)\chi c_0^2/c_\infty^2]/2$. Again the acoustic mode is weakly damped due to viscosity and thermal diffusion. In this limit, energy exchange cannot occur and the oscillatory mode is not coupled to the structural relaxation processes. The fluid behaves like a solid in this high-frequency limit. In between the two limits, i.e. $\omega_A \tau_R \sim 1$, the acoustic velocity varies between c_0 and c_∞. There is an additional contribution to the acoustic damping rate from the structural relaxation which can occur during an acoustic period.

To study structural relaxation dynamics through acoustic measurements, one usually introduces a frequency dependence for the longitudinal acoustic modulus $M(s) = M'(s) + iM''(s)$. The dispersion relation

$$\rho_0 s^2 + M(s) q^2 = 0 \tag{3.37}$$

yields the familiar expressions [62] for $M(s)$ in terms of the acoustic frequency and damping rate,

$$\frac{M'(\omega_A)}{\rho_0} = \frac{\omega_A^2 - \Gamma_A^2}{q^2}, \tag{3.38}$$

$$\frac{M''(\omega_A)}{\rho_0} = \frac{2\omega_A \Gamma_A}{q^2}. \tag{3.39}$$

For an elastic medium, $\Gamma_A = 0$. One thus gets sharp sound wave resonances at the acoustic frequency ω_A and Eqs. 3.38 and 3.39 lead to a real modulus $M = M' = \rho_0(\omega_A/q)^2 = \rho_0 c_0^2$. For a simple liquid the viscosities and thermal diffusion introduce a damping rate $\Gamma_A = \Gamma_A^B$ for the acoustic propagation, which yields an imaginary part for the modulus. If the sample is a relaxing liquid, the structural relaxation then makes additional contributions to the acoustic damping rate $\Gamma_A = \Gamma_A^B + \Gamma_R$, which induces a frequency dependence for the modulus. That is, the acoustic modulus increases with increasing ω_A from the below "resonance" value $M(\omega_A \tau_R \ll 1) =$

$M_0 = \rho_0 c_0^2$ to the above "resonance" value $M(\omega_A \tau_R \gg 1) = M_\infty = \rho_0 c_\infty^2$. This variation is connected to some spectral peak of the imaginary part $M''(\omega_A)$ via Kramers-Kronig relations.

On the other hand, Eq. 3.21 yields the acoustic dispersion relation

$$s^2 + s\left[\phi_L(q,s)q^2 + \Gamma_H(\gamma - 1)\right] + c_0^2 q^2 = 0. \tag{3.40}$$

Comparison to Eq. 3.37 leads to

$$\frac{M(s)}{\rho_0} = s\left[\phi_L(q,s) + \chi(\gamma - 1)\right] + c_0^2, \tag{3.41}$$

or

$$\begin{aligned} \frac{M'(\omega_A)}{\rho_0} &= -\omega_A \mathrm{Im}\left[\phi_L^R(q,\omega_A)\right] + c_0^2, & (3.42)\\ \frac{M''(\omega_A)}{\rho_0} &= \omega_A \mathrm{Re}\left[\phi_L^R(q,\omega_A)\right] + \omega_A\left[\nu_L + \chi(\gamma - 1)\right]. & (3.43) \end{aligned}$$

Here $(-\rho_0\omega_A \mathrm{Im}[\phi_L^R(q,\omega_A)])$ and $(\rho_0\omega_A \mathrm{Re}[\phi_L^R(q,\omega_A)])$ are the real and imaginary relaxing parts of the longitudinal modulus. In the Debye relaxation model they are equal to $\rho_0(c_\infty^2 - c_0^2)\omega_A^2\tau_R^2/(1+\omega_A^2\tau_R^2)$ and $\rho_0(c_\infty^2 - c_0^2)\omega_A\tau_R/(1+\omega_A^2\tau_R^2)$, respectively. As expected, the imaginary relaxing part of the acoustic modulus divided by the acoustic frequency shows a Lorentzian shape with a maximum at $\omega_A\tau_R = 1$.

Care needs to be taken to analyze structural relaxation dynamics through acoustic modulus, since there are contributions from viscosity and thermal diffusion as well as the structural relaxation. One way to do the analysis is to calculate the total acoustic modulus, by using Eq. 3.38 and 3.39, from the measured acoustic frequency and damping rate. The structural relaxation dynamics can then be obtained by including a linear-ω-dependent term in the fitting function which, of course, contains some relaxation function form. The other way is to split the measured acoustic damping rate Γ_A into two parts, with Γ_A^B representing a background contribution from viscosity and thermal diffusion processes, and Γ_R representing the structural relaxation contribution. The structural relaxation contribution $M_R(\omega_A)$ to the longitudinal modulus can then be calculated as:

$$\frac{M_R'}{\rho_0} = \frac{\omega_A^2 - \Gamma_R^2}{q^2} - c_0^2, \tag{3.44}$$

$$\frac{M_R''}{\rho_0} = \frac{2\omega_A \Gamma_R}{q^2}, \tag{3.45}$$

which gives directly the relaxation dynamics. For a Debye relaxation process one obtains, by substituting Γ_R from Eq. 3.32 into the above equations, a Lorentzian shape with a maximum at $\omega_A \tau_R = 1$ for M_R''/ω_A and an increase from 0 at low frequency to $\rho_0(c_\infty^2 - c_0^2)$ at high freqency for the real part, as that in Eq. 3.43.

It is worthwhile to emphasize the importance of subtracting Γ_A^B, the contribution of the viscosity and thermal diffusion processes, from the measured total damping rate in order to derive the structural relaxation contribution to the longitudinal modulus. This is not always done. However, if the background contribution is significant then the need for its subtraction is clear from inspection of Eq. 3.39. Since Γ_A^B/q^2 is frequency-independent, the "white noise" contribution (linear in ω) is added to the imaginary part of the relaxation contribution to $M(\omega_A)$. As a result, the peak of M_R'' is pushed to a higher frequency and its shape is also changed, especially in the high frequency wing. For example, if one inserts the damping rate Γ_A of Eq. 3.32 for a Debye relaxation process into Eq. 3.39, one would not obtain a Lorentzian shape for $M''(\omega_A)/\omega_A$ as expected. The peak frequency is not τ_R^{-1} either. The real part $M'(\omega_A)$ is also effected. Figure 3-1 illustrates the difference between the relaxation spectrum and total longitudinal modulus spectrum due to the background contribution for a Debye α relaxation process. The background contribution (dotted curve) is calculated with a damping rate Γ_B^A equal to 5 percent of the damping rate Γ_R at the α peak. The total modulus spectrum (dashed curve) shows almost no difference from the α spectrum (solid curve) from low ferquency up close to the α peak. However, they are utterly different in the high frequency region. Especially, there exists a minimum in the total modulus spectrum. Clearly this minimum has a different origin as the one in the susceptibility spectrum $\chi''(\omega)$ of MCT described in Chapter 1. Therefore, it is important that one should subtract

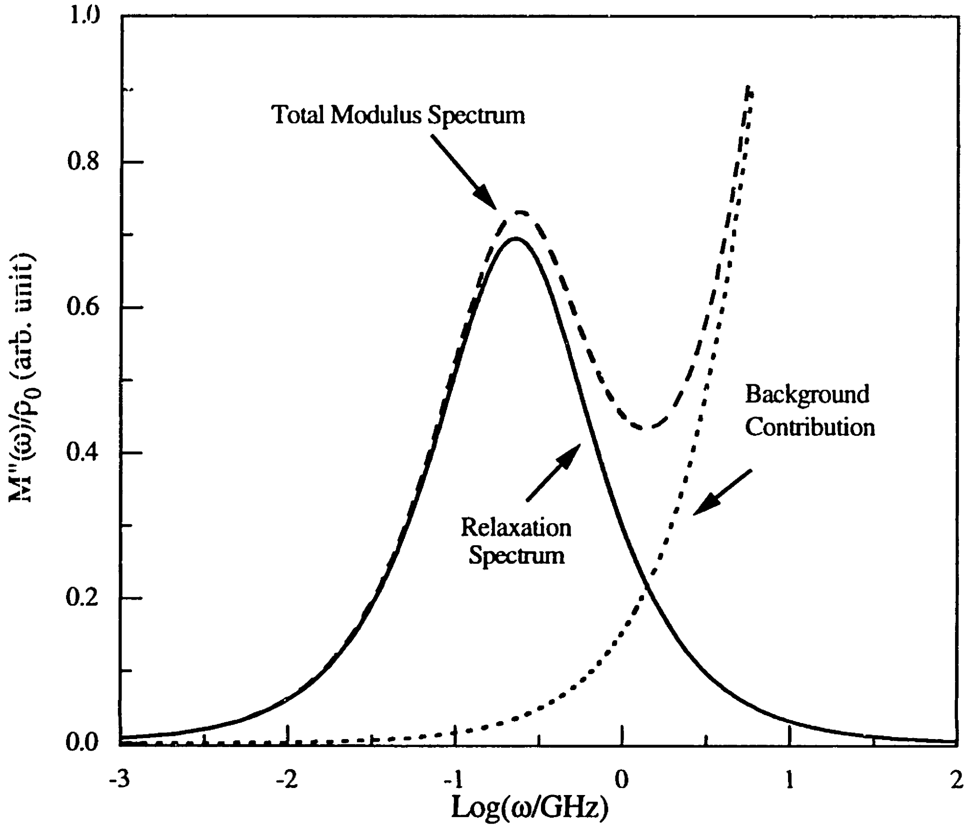

Figure 3-1: The frequency dependence of the imaginary part of the reduced acoustic modulus for the Debye α relaxation (solid line), viscosities and thermal diffusion or background contribution (dotted line), and the superposition of both (dashed line). The background contribution is the result with a damping rate Γ_B^A equal to 5 percent of the damping rate Γ_R at the peak of the relaxation spectrum.

the background contribution from the total acoustic damping rate to study the structural relaxation dynamics, or include a linear-ω-dependent term in the analysis of the total modulus spectrum.

3.3.2.2 Mountain Mode Dynamics

The ISTS response of Eq. 3.34 consists of two parts. The first "A" term describes the behavior of simple liquids, including glass-forming liquids at high temperatures. In such samples, sudden spatially periodic heating at wavevector q leads to spatially periodic thermal expansion which occurs on the time scale of half the acoustic oscillation period $\pi/\omega_A(q)$. There are a transient acoustic response consisting of damped acoustic oscillations and a steady-state density modulation which decays due to thermal diffusion at the rate $\Gamma_H(q)$. These are time-domain observations of the Brillouin and Rayleigh features in the light scattering spectrum. Besides the acoustic and thermal diffusion modes, the most striking feature of the response function $G_{\rho T}(q,t)$ given in Eq. 3.34 is the presence of a second exponential decay mode contained in the second "B" term, which describes the modifications to the transient acoustic behavior for viscoelastic fluids. This mode, often called the Mountain mode, is due to structural relaxation with a decay rate of $c_0^2 c_A^{-2} \tau_R^{-1}$. Therefore, the structural relaxation time can be directly extracted through ISTS measurement. Note that in ISTS signal the existence of such a relaxation mode manifests itself as an exponential rise instead of exponential decay because of its negative amplitude. Physically it represents slow components in the time-dependent volume response of the sample to sudden heating.

In $G_{\rho\rho}(q,t)$ as given by Eq. 3.33, there also appears an exponentially decaying mode with a decay rate of $c_0^2 c_A^{-2} \tau_R^{-1}$. It seems that the relaxation information could also be obtained directly from ISBS measurements. However, as discussed below, the amplitude of this mode is often too small to be detected in ISBS. In the following section we will mainly discuss the density response function $G_{\rho T}(q,t)$ measured in ISTS.

3.3.2.3 Intensity Ratio and Debye-Waller Factor

An important point can be made concerning the relative amplitudes of the three modes given in Eq. 3.34. The amplitudes of the thermal diffusion, acoustic and relaxation mode are $A+B$, $-A$, and $-B$, respectively. The ratio of the amplitudes of the relaxation mode to the thermal diffusion mode is therefore equal to $-B/(B+A)$. Similarly the ratio of the amplitudes of the relaxation mode to acoustic mode is B/A. At high frequencies, $\omega_A \tau_R \gg 1$, $c_A = c_\infty$, and A and B become $-(\kappa/c_p)(c_0^2/c_\infty^2)$ and $-(\kappa/c_p)(1-c_0^2/c_\infty^2)$, respectively. The nonergodicity parameter $f_{q\to 0}(T)$ is then related to the relative amplitude ratio of the relaxation mode to the thermal diffusion mode in $G_{\rho T}(q,t)$ as

$$f_{q\to 0}(T) = 1 - \frac{c_0^2}{c_\infty^2} = \frac{B}{A+B} \tag{3.46}$$

when $\omega_A \gg \tau_R^{-1} \gg \Gamma_H$, i.e. when all four roots of the dispersion equation 3.29 are well separated. The left-hand side of Eq. 3.46 has been derived separately [42].

The result in Eq. 3.46 is far more general than the Debye form for the memory function $\phi_L(q,t)$. It will be shown in the next section that it holds for any model of the memory function and so for any form of the relaxation function as long as the characteristic time scales of the relaxation mode, thermal diffusion mode and acoustic mode are well separated from each other. Before proving this, we first inspect briefly Eqs. 3.34 and 3.46. If one divides both sides of Eq. 3.34 by the amplitude of the thermal mode $A+B$, then Eq. 3.46 simply states that the nonergodicity parameter is determined by the amplitude of the α relaxation. This is a natural result of the definition of $f_{q\to 0}$. Therefore, it should not depend on any particular relaxation forms.

For the response function $G_{\rho\rho}(q,t)$ given in Eq. 3.33, the ratio between the relaxation mode amplitude to that of acoustic mode (the first term) is

$$I_{CB} = \frac{1 - c_0^2/c_\infty^2}{\omega_A^2 \tau_R^2 + c_0^2/c_A^2}\,\omega_A \tau_R. \tag{3.47}$$

It can be seen that the ratio I_{CB} becomes zero in both the low frequency limit

($\omega_A \tau_R \ll 1$), and the high frequency limit ($\omega_A \tau_R \gg 1$). Even in the intermediate frequency range i.e. $\omega_A \tau_R \sim 1$, I_{CB} is much less than 1. This means that the relaxation mode may appear only weakly in the ISBS signal. Therefore neither the relaxation dynamics nor the relaxation strength can be obtained easily from this feature in ISBS data. The terms in the square brackets of Eq. 3.33 can be ignored and only the first term is left which represents acoustic oscillations. Therefore, Eq. 3.33 becomes approximately

$$G_{\rho\rho}(q,t) = A_{\rho\rho} e^{-\Gamma_A t} \sin(\omega_A t). \tag{3.48}$$

The acoustic properties can be used to determine structural relaxation dynamics through the complex modulus, but generally not the relaxation strength since the dynamic range of acoustic frequencies is usually not sufficient for separate determination of c_0 and c_∞.

3.4 Generalized ISTS Response Function

Equation 3.34 can be easily generalized to more complicated relaxational dynamics such as the KWW stretched exponential function:

$$G_{\rho T}(q,T) = A\left[e^{-\Gamma_H t} - e^{-\Gamma_A t}\cos(\omega_A t)\right] + B\left[e^{-\Gamma_H t} - e^{-(t/\tau'_R)^\beta}\right]. \tag{3.49}$$

Here we have replaced the single-exponential relaxation by a stretched KWW function with characteristic parameters $\tau'_R = \tau_R c_\infty^2 / c_0^2$ and β, reflected in the slow rising mode. This generalized response function $G_{\rho T}(q,t)$ exhibits thermal diffusion, acoustic, and structural relaxation modes as described earlier by Eq. 3.34 but now the relaxation mode is more complex.

Concerning measurement of the relaxation mode, ISTS is just like any other response techniques as discussed in Chapter 1. This is because at $t = 0$ the temperature grating is instantaneously produced and the field can be considered to be constant under the condition of $\Gamma_H \tau_R \ll 1$. The time-dependent density response to the field is measured. This is obvious by examining Eq. 3.49. If one drops the terms in the first square bracket which describes the simple liquid behavior, then one ends up with

$$G_{\rho T}(q,T) = B\left[e^{-\Gamma_H t} - e^{-(t/\tau'_R)^\beta}\right]. \tag{3.50}$$

Under the condition of $\Gamma_H \tau_R \ll 1$, one would have $G_{\rho T}(q,T)/B = 1 - \exp[-(t/\tau'_R)^\beta]$ by replacing the first exponential term by 1. This is exactly the relation as described in Eq. 1.6 between the relaxation function and the response function.

As discussed above, the relation 3.46 still holds for the KWW relaxation function in the generalized ISTS response function of Eq. 3.49. We shall now present a mathematical proof of this statement.

We first rewrite Eq. 3.18 under the conditions $\nu_L q^2 \ll c_0 q$ and $\Gamma_H \ll c_0 q$ as follows:

$$-\frac{c_p}{\kappa}G_{\rho T}(q,s) = \frac{1}{s+\Gamma_H} - \frac{s+\phi_L(q,s)q^2}{s^2+s[\phi_L(q,s)q^2+\Gamma_H(\gamma-1)]+c_0^2q^2}. \tag{3.51}$$

By setting $\tilde{t} = tz$, $G_{\rho T}(q,t)$ becomes $\tilde{G}_{\rho T}(q,\tilde{t})$. Its Laplace transform $G_{\rho T}(q,s)$ becomes $\tilde{G}_{\rho T}(q,\tilde{s})/z$ with $\tilde{s} = s/z$ and $\tilde{G}_{\rho T}(q,\tilde{s})$ denoting the Laplace transform of $\tilde{G}_{\rho T}(q,\tilde{t})$. For the relaxational part of $\phi_L(q,t)$ there exist analogous relations, i.e. $\phi_L^R(q,t) = \tilde{\phi}_L^R(q,\tilde{t})$, and $\phi_L^R(q,s) = \tilde{\phi}_L^R(q,\tilde{s})/z$. When $z \to 0$ but rescaled time $\tilde{t}$ is fixed at a finite value, the α-relaxation process is separated from other processes, i.e. the condition for Eq. 3.46 to hold is satisfied. In this limit, substituting the above relations into Eq. 3.51 yields $(c_p/\kappa)\tilde{G}_{\rho T}(q,\tilde{s}) = 1/[\tilde{s} + c_0^2/\tilde{\phi}_L^R(q,\tilde{s})]$. By performing the inverse Laplace transform, one obtains

$$\frac{c_p}{\kappa}\tilde{G}_{\rho T}(q,\tilde{t}) = \frac{\tilde{\phi}_L^R(q,\tilde{t})}{c_0^2} - \frac{c_p}{\kappa}\frac{d}{d\tilde{t}}\int_0^{\tilde{t}} \frac{\tilde{\phi}_L^R(q,\tilde{t}-\tilde{t}')}{c_0^2}\tilde{G}_{\rho T}(q,\tilde{t}')d\tilde{t}'. \tag{3.52}$$

It follows directly from this equation that, independent of any specific model, a quasielastic peak in the kinematic viscosity spectrum $\tilde{\phi}_L^R(q,\tilde{\omega})$ causes a corresponding peak of $\tilde{G}_{\rho T}(q,\tilde{\omega})$ for the density response and vice versa. The integrated intensities ν_R and Bc_p/κ of the α peaks of the kinematic viscosity spectrum $\tilde{\phi}_L^R(q,\tilde{\omega})$ and density spectrum $\tilde{G}_{\rho T}(q,\tilde{\omega})$ are given by $\nu_R = \tilde{\phi}_L^R(q,\tilde{t} \to 0)$ and $Bc_p/\kappa = -(c_p/\kappa)\tilde{G}_{\rho T}(q,\tilde{t} \to 0)$, respectively. The limit $\tilde{t} \to 0$ in Eq. 3.52 leads to the result

$$\frac{-B}{\kappa/c_p} = \frac{\nu_R/c_0^2}{1+\nu_R/c_0^2}. \tag{3.53}$$

With $\nu_R = c_\infty^2 - c_0^2$, Eq. 3.53 is the same as Eq. 3.46 since $A + B = -\kappa/c_p$. Similar results have been shown [45, 63] for BS for any shape of the relaxation spectral peak, for example, Debye, Cole-Davidson, or KWW forms, etc.

3.5 Comparison of ISS to Rayleigh-Brillouin Scattering

Light scattering spectroscopy has been applied extensively to the study of liquid-glass transition. The underlying theoretical development [27, 64-67] on the basis of generalized hydrodynamics (Eqs. 3.5-3.6) has been largely paralleled in this Chapter, and fits to experimental spectra have been achieved through introduction of various memory functions [43, 45, 46]. In this section, we discuss the relationship between BS and ISTS.

As discussed above, ISTS data show acoustic, thermal diffusion, and structural relaxation dynamics in features closely analogous to the Brillouin, Rayleigh, and Mountain mode contributions to BS spectra. The spectral distribution of BS in the single-relaxation-time approximation can be obtained to the lowest order, from Eqs. 3.7 and 3.8 with F and Q being set to zero. The solution for the density fluctuations is given by

$$\begin{aligned}\delta\rho(\rho,s) &= \delta\rho(q)\left\{G_{\rho\rho}\left[\frac{\tau_R s^2}{q^2} + \left(\frac{1}{q^2} + \tau_R\nu_B\right)s + \nu_B + (c_\infty^2 - c_0^2)\tau_R\right]\right.\\ &\qquad \left. -G_{\rho T}\frac{c_v(\gamma-1)}{\kappa}\right\}. \end{aligned}\tag{3.54}$$

Following the same procedure as above, the contributions to the normalized spectrum from both $G_{\rho\rho}$ and $G_{\rho T}$ terms can be determined. The result for the spectral distribution $\sigma_{\rho\rho}$ from $G_{\rho\rho}$ is

$$\sigma_{\rho\rho}(q,\omega) = A_{\rho B}\left[\frac{\Gamma_A}{(\omega-\omega_A)^2+\Gamma_A^2} + \frac{\Gamma_A}{(\omega+\omega_A)^2+\Gamma_A^2}\right] + A_{\rho C}\frac{2c_0^2 c_A^{-2}\tau_R^{-1}}{\omega^2 + c_0^4 c_A^{-4}\tau_R^{-2}}, \tag{3.55}$$

where

$$A_{\rho B} = \frac{c_0^2 c_A^{-2}\tau_R^{-2} - (c_\infty^2 - c_0^2)q^2 + c_A^2 q^2}{c_0^4 c_A^{-4}\tau_R^{-2} + c_A^2 q^2}, \tag{3.56}$$

$$A_{\rho C} = \frac{c_0^4 c_A^{-4}\tau_R^{-2} + (c_\infty^2 - c_0^2)q^2 - c_0^2 c_A^{-2}\tau_R^{-2}}{c_0^4 c_A^{-4}\tau_R^{-2} + c_A^2 q^2}. \tag{3.57}$$

The spectral distribution $\sigma_{\rho T}$ from $G_{\rho T}$ is

$$\begin{aligned}\sigma_{\rho T}(q,\omega) &= A_{TB}\left[\frac{\Gamma_A}{(\omega-\omega_A)^2+\Gamma_A^2} + \frac{\Gamma_A}{(\omega+\omega_A)^2+\Gamma_A^2}\right] \\ &\quad +(1-\frac{1}{\gamma})\frac{2\Gamma_H}{\omega^2+\Gamma_H^2} + A_{TC}\frac{2c_0^2 c_A^{-2}\tau_R - 1}{\omega^2 + c_0^4 c_A^{-4}\tau_R^{-2}},\end{aligned} \tag{3.58}$$

where

$$A_{TB} = -\left(1-\frac{1}{\gamma}\right)\frac{c_0^4 c_A^{-4}\tau_R^{-2} + c_0^2 q^2}{c_0^4 c_A^{-4}\tau_R^{-2} + c_A^2 q^2}, \tag{3.59}$$

$$A_{TC} = -\left(1-\frac{1}{\gamma}\right)\frac{(c_A^2 - c_0^2)q^2}{c_0^4 c_A^{-4}\tau_R^{-2} + c_A^2 q^2}. \tag{3.60}$$

$\sigma_{\rho\rho} + \sigma_{\rho T}$ gives the total normalized BS spectral distribution obtained by Mountain [27, 65, 67]. It is seen that both $\sigma_{\rho\rho}$ and $\sigma_{\rho T}$ exhibit a damped sound wave and a relaxation process, while only $\sigma_{\rho T}$ exhibits thermal diffusion. From Eqs. 3.34, 3.55, and 3.58, it follows that the spectral distribution $\sigma_{\rho T}(q,\omega)$, but neither $\sigma_{\rho\rho}$ nor the total BS spectral distribution $\sigma_{\rho\rho}+\sigma_{\rho T}$, is proportional to the real part of the Fourier transform of the density response function $G_{\rho T}(q,t)$ measured in ISTS. This is to be expected since ISTS signal results from density changes induced thermoelastically through sudden heating while the BS spectrum results from density fluctuations induced both thermoelastically through spontaneous temperature fluctuations and adiabatically with no significant change in temperature. This is expressed through the initial conditions Eqs. 3.9 and 3.10 which are substituted into the preceding thermoelastic equations of motion.

Note that the generalized hydrodynamics equations described above are for an isotropic medium. For anisotropic molecular liquids the BS spectrum includes a significant contribution from polarizability anisotropy, mediated primarily through molecular orientational motion [45, 46]. However, in polarized (VV) ISTS the longitudinal motion is excited selectively, since the transient heating does not orient molecules. The anisotropic contribution to signal is usually negligibly small by comparison, so the above theory is still applicable for anisotropic materials.

The Debye-Waller factor can also be obtained from the BS spectrum. From Eqs. 3.55 and 3.58, when $\omega_A \gg \tau_R^{-1} \gg \Gamma_H$ the integrated areas of the Rayleigh peak, Brillouin doublets and Mountain peak are given by $1 - 1/\gamma$, $c_0^2/(\gamma c_\infty^2)$, and $(1 - c_0^2/c_\infty^2)/\gamma$, respectively. Thus

$$f_{q\to 0}^{BS} = \frac{\text{Mountain peak integrated area}}{\text{Mountain peak area} + \text{Brillouin peaks area}}. \tag{3.61}$$

In ISTS, the sum of the Mountain and acoustic mode amplitudes is equal to the thermal mode amplitude, so the thermal mode amplitude was used as reference to obtain the Debye-Waller factor. In BS, however, the contribution of $G_{\rho\rho}$ to the total spectral distribution changes the relative amplitudes such that the ratio of the Rayleigh peak area to the sum of Mountain and Brillouin peak areas gives the Landau-Placzek ratio.

In practice, determination of the Debye-Waller factor for a glass-forming liquid over a wide range of temperatures through either ISTS or BS presents challenges. As the sample is cooled to temperatures even well above T_g, the Mountain mode response, measured by τ_R' or its inverse, shifts from picosecond to millisecond time scales in ISTS data or from GHz to KHz linewidths in the BS spectrum. Determination of $f_{q\to 0}(T)$ requires that the conditions $\omega_A(q) \gg \tau_R^{-1} \gg \Gamma_H(q)$ be met. Hence, at any single scattering wavevector q this will obtain over a very narrow temperature range. In ISTS, variation of the scattering angle over a wide range is practical so that substantial variation of q is possible. In BS, this is more difficult. For this reason, ISTS currently presents more favorable practical prospects for determination of the Debye-Waller factor over a temperature range wide enough to permit critical testing of mode coupling theoretical predictions concerning its temperature-dependent behavior.

Equation 3.33 gives the response function $G_{\rho\rho}(q,t)$ measured in ISBS, which includes the oscillatory part and relaxational contributions. The dynamical parameters such as acoustic frequency, damping rate and relaxation time are the same as those measured in BS. But the relative contribution of each mode to ISBS is different from that to BS. As discussed above, ISBS data permit only weak observation of the Mountain mode, and generally cannot be used to measure the Debye-Waller factor. In addition, there is no thermal diffusion mode in ISBS to the lowest order, unlike in BS. (For the solutions of ISS and BS to the first order, see Appendix A.).

To close this section, we will briefly discuss the relationship between ISTS and another light scattering technique, photon correlation spectroscopy, which has been applied to study the dynamics of glass-forming liquids [11, 12, 68], especially at temperatures around T_g. Thermal diffusion and structural relaxation dynamics are observed in PCS measurements. When the structural relaxation time τ_R is much longer than the thermal diffusion time $\tau_H = \Gamma_H^{-1}$, the structural relaxation dynamics are determined. In homodyne detection the measured time-correlation function $C(q,t)$ of the scattered light intensity is related to the normalized density-density correlation function $\phi(q,t)$ by [11]

$$C(q,t) = B_1 + A_1\phi^2(q,t), \tag{3.62}$$

and in heterodyne detection the relationship between $C(q,t)$ and $\phi(q,t)$ is [12]

$$C(q,t) = B_2 + A_2\phi(q,t). \tag{3.63}$$

Here B_1 and B_2 give the background signal levels measured at long times; A_1 and A_2 are relative amplitudes that in practice can be considered fitting parameters. Often $\phi(q,t)$ is extracted from PCS data and fit with the KWW function. ISTS and PCS should yield the same α-relaxation dynamics, but in practice PCS is useful at lower temperatures and slower time scales.

3.6 Discussion

In our treatment we simply generalized the ISS response functions obtained from the Debye model to account for complex relaxation, without attempting to derive complex behavior through the use of a specific model for the relaxation kernel. In mode coupling theory, models have been used which permit numerical calculation of the relaxation function and whose results can be approximated rather accurately by the KWW function. Here we discuss the connection between the hydrodynamics equations for ISS and MCT.

As reviewed in Chapter 1, the starting point of MCT is a closed set of generalized kinetic equations (Eq. 1.20) for the density autocorrelation function $\phi_q(t)$. It assumes that the nonlinear coupling of the density fluctuations and coupling of density fluctuations to the currents are the cause of the structural relaxation. Analysis of Eqs. 1.20 then reveals many features which resemble experimental findings for glass-forming liquids. It is easy to show that the generalized hydrodynamics Eqs. 3.4-3.6 have the same structure as MCT Eq. 1.20. To do that, we first find a formal solution to Eq. 3.6, which reads

$$\begin{aligned} \delta T(q,t) &= \frac{1}{\rho_0 c_v}\int_0^t dt' \exp\left(-\frac{\lambda q^2}{\rho_0 c_v}(t-t')\right) Q(q,t') \\ &\quad + \frac{\gamma-1}{\rho_0 \kappa}\int_0^t dt' \exp\left(-\frac{\lambda q^2}{\rho_0 c_v}(t-t')\right) \delta\dot{\rho}(q,t'). \end{aligned} \tag{3.64}$$

Then substituting the above equation and Eq. 3.4 into Eq. 3.5, one finds the equation for the density response $\delta\rho(q,t)$ under conditions of ideal time and wavevector resolution:

$$\delta\ddot{\rho}(q,t) + \nu_L q^2 \delta\dot{\rho}(q,t) + \frac{k_B T_0}{S(q)} q^2 \delta\rho(q,t) + \int_0^t dt' \Phi(q,t-t')\delta\dot{\rho}(q,t')$$

$$= -q^2 \left[F_0(q) + \frac{\kappa}{c_v} \frac{k_B T_0}{S(q)} Q_0(q) \exp\left(-\frac{-\lambda q^2}{\rho_0 c_v} t \right) \right], \qquad (3.65)$$

with the memory function

$$\Phi(q,t) = q^2 \phi_L^R(q,t) + \frac{k_B T_0}{S(q)} (\gamma - 1) q^2 \exp\left(-\frac{\lambda q^2}{\rho_0 c_v} t \right), \qquad (3.66)$$

where $\phi_L^R(q,t) = \phi_L(q,t) - \nu_L$ is the relaxational part of the kinematic viscosity. It is seen that the left hand side of Eq. 3.65 has exactly the same form as that of the MCT Eq. 1.20, while the right-hand side of Eq. 3.65 is simply the driving force exerted through pulsed excitation in ISS. The only difference is that in MCT the last term of the memory function $\Phi(q,t)$ in Eq. 3.66 which results from the coupling between density and temperature fluctuations has been left out. This difference is of no importance since the exponential term in Eqs. 3.65 and 3.66 can be replaced by 1 under the condition $\Gamma_H \tau_R \ll 1$, and that is the condition on which all the main results in earlier sections are based. In the spirit of MCT, therefore, one could derive the complex relaxation dynamics for the Mountain mode in the ISS response functions by assuming the MCT relaxation kernel of Eq. 1.21, provided that the acoustic and thermal modes are well separated from the Mountain mode.

As for short-time dynamics, MCT predicts that there is a secondary β relaxation which precedes α relaxation in time. In the "mesoscopic" time window between the microscopic vibrational period $\sim \Omega^{-1}$ and the α-relaxation time τ_α, both α and β relaxations obey critical power laws. If one again uses the MCT relaxation kernel of Eq. 1.21, one should find that there is a β relaxation feature, preceding the α relaxation dynamics as discussed above in ISS response functions. Here we will not get into a deeper discussion of this. Rather we will assume the MCT results without detailed proof and generalize the ISTS response function $G_{\rho T}(q,t)$ in accordance with them to include the β relaxation contribution:

$$\begin{aligned} \frac{G_{\rho T}(q,t)}{(A+B)} &= e^{-\Gamma_H t} - \frac{A}{A+B} e^{-\Gamma_A t} \cos(\omega_A t) \\ &\quad - \left\{ f_{q \to 0} e^{-(\Gamma_R t)^\beta} + h_q \left[G(t;\sigma) + C\sqrt{\sigma} (t/t_\sigma)^b \right] \right\}. \end{aligned} \qquad (3.67)$$

Since the β master function $G(t;\sigma)$ contains the von Schweidler decay, the initial part of the α relaxation, the final term in Eq. 3.67 must be included to avoid double counting. Also, both sides of Eq. 3.67 have been divided by the amplitude $A+B$ of the thermal diffusion mode, so the amplitude of the α relaxation mode gives the Debye-Waller factor $f_{q\to 0}$. In practice, ISS experiments, as will be presented in the following Chapters, do not appear to have shown evidence of β relaxation dynamics in the Mountain mode because the observations of this mode have been on time scales longer than that the β relaxation occurs [9, 10, 69]. However, β relaxation may be observed in the complex elastic modulus spectrum measured in ISS in higher frequency range.

3.7 Summary and Conclusions

From the foregoing analysis, we conclude that ISS response functions can be constructed based on the generalized hydrodynamics equations which include nonlocal behavior in time to describe long-wavelength cooperative motions in supercooled liquids. An ISTS measurement of the density response to laser-induced heating in supercooled liquids contains five dynamical parameters, assuming that the structural relaxation dynamics can be described by two parameters as in the KWW form. Two of these are the acoustic frequency and damping rate. By measuring them at several wavevectors, the acoustic modulus spectrum can be constructed and used to examine the high-frequency structural relaxation dynamics. The third quantity, thermal diffusivity, can be determined accurately from the long-time decay in ISTS signal. The other two dynamical parameters are those of the Mountain mode which describes structural relaxation dynamics on nanosecond-millisecond time scales. This response, unlike the others, is wavevector-independent, and permits complex relaxation dynamics at a given temperature to be determined from a single measurement at a choice of wavevector which yields good separation between the acoustic, structural relaxation, and thermal diffusion responses. At different temperatures, different choices of wavevector may be needed to ensure this separation.

ISTS data also yield the relative amplitudes of the Mountain and Brillouin features. The amplitude ratio permits determination of the nonergodicity or Debye-Waller parameter of the mode coupling theory. ISTS measurement of $f_q(T)$ in the low-q limit is complementary to neutron scattering measurement of the integrated intensity of the α (elastic) peak to give $f_q(T)$ at large q. Note that in ISTS, unlike in neutron scattering, absolute measurement of scattering intensity is not necessary for determination of the Debye-Waller factor, since the thermal diffusion mode provides a reference for normalization of the response function at each temperature.

We have shown that both ISTS and BS measurements provide the same information, in principle, concerning the acoustic mode, Rayleigh mode and Mountain mode. As discussed above and also in Refs. [45] and [46], the Mountain mode dynamics and amplitude are often difficult to determine unambiguously through BS alone, due to the limited wavevector range and frequency window and the possibility of β-relaxation contributions to the spectrum which may make the analysis complicated. It is particularly difficult to obtain reliable information about structural relaxation dynamics and the Debye-Waller factor over a wide temperature range without the capability for recording BS spectra in a wide frequency range at a single wavevector and with substantial variation of the scattering wavevector.

At temperatures close to and below T_g, PCS measurement can yield the Mountain mode dynamics (although not the Debye-Waller factor). In some temperature region, PCS and ISTS measurements should give the same results on dynamics. PCS is most powerful in very slow time ranges (from μs to many seconds) while ISTS is well suited for faster (ns to many ms) time scales. It is interesting to note that the condition for the Mountain mode to be observed in PCS is opposite to that in ISTS. In PCS, one has to go to a large wavevector so that thermal diffusion is faster than the density-density correlation dynamics which are determined by structural relaxation and which are relatively slow at low temperatures. In ISTS, a small excitation wavevector has to be used to extend to low temperatures so that thermal diffusion is slower than the structural relaxation dynamics. Limitations on how low a wavevector (i.e. how small an excitation angle) is accessible in an ISTS experiment ultimately prevent measurement of structural relaxation at very low T. PCS measurements are needed to go to even lower temperatures.

In conclusion, ISS response functions $G_{\rho T}(q,t)$ and $G_{\rho\rho}(q,t)$ have been derived based on the generalized hydrodynamics equations, and their properties have been discussed in detail. The most important results concern the possibilities for measurement of Mountain mode dynamics and the Debye-Waller factor, which can be used to test central predictions of the mode-coupling theory, and the fundamental connection between the structure of the mode coupling and ISTS theoretical description.

Chapter 4

Relaxation Dynamics and Nonergodicity Parameter of Salol

In the rest of this thesis, we will present our ISTS experimental studies on a couple of model glass formers. As described by our theoretical model in Chapter 3, the ISTS data contain contributions from three modes: the acoustic, thermal diffusion, and relaxation or Mountain modes. With the current improved ISTS system as described in Chapter 2, the relaxation mode can be monitored in the time range from nanoseconds to many milliseconds permitting examination of predictions for T-dependent structural relaxation dynamics. In addition, the relaxation strength can be obtained from the relative amplitude ratio of the relaxation mode and thermal diffusion mode, which allows testing of the MCT predictions concerning the nonergodicity parameter f_q. For the acoustic mode, the frequency range covered goes from 10 MHz to several GHz, which bridges the frequency gap between ultrasonic measurements and Brillouin scattering. The characterization of the acoustic mode in this frequency window can provide valuable information for testing of the mesoscopic dynamics predicted by the MCT.

One of the model glass formers we have studied is the organic molecule salol. We have performed measurements at multiple excitation angles or wavevectors in order to characterize both the relaxation mode and acoustic mode. In this Chapter[1], we present a detailed analysis of the relaxation mode. Both dynamics and relaxation strength are analyzed and compared to the predictions of the mode coupling theory of the liquid-glass transition. We will leave the analysis of the acoustic mode to Chapter 6.

4.1 Introduction

The development of the first-principles approach of mode-coupling theory to the liquid-glass transition, reviewed in Chapter 1, has provided quantitative predictions for complex structural relaxation dynamics which are assumed to result from the retarded nonlinear interactions among density fluctuations. A central MCT prediction concerns the α relaxation strength or the effective Debye-Waller factor $f_q(T)$, defined as the integrated area of the α relaxation spectrum in the frequency domain, or equivalently, the amplitude of the α relaxation function in the time domain. In idealized MCT where thermally activated processes are ignored, there occurs an ergodic-to-nonergodic transition at a crossover temperature T_c at which $f_q(T)$ shows a square-root cusp. With thermally activated processes included in the extended MCT, ergodicity below T_c is restored. In this case $f_q(T)$ is predicted to show similar behavior except that the square-root cusp is somewhat smoothed over at temperatures around T_c. The crossover temperature T_c should be an intrinsic property of a material and should depend on neither wavevector q nor the experimental technique used for determination of $f_q(T)$.

The predicted square-root cusp of $f_q(T)$ has been observed in several materials [2, 44, 73-75] through measurements of the integrated intensity of the α (elastic) peak in the neutron scattering spectrum or the height of the plateau in the correlation function $\Phi(q, t)$ in neutron spin-echo experiments. Several experimental results have been reviewed in Chapter 1. In the low-q limit, one way to determine $f_q(T)$ is through the relation Eq. 1.47 by measurements of two limiting velocities c_0 and c_∞

---

[1] Some of the materials in this Chapter have been published in Refs. [70-72].

in ultrasonic experiments or Rayleigh-Brillouin scattering. However, as discussed in Chapter 1, both techniques are insufficient for unique determination of c_0 and c_∞, and thus $f_{q\to 0}$, in a temperature range wide enough for the determination of cusp-like behavior or the crossover temperature T_c.

Analogous to neutron scattering, the other way to determine $f_q(T)$ in the $q \to 0$ limit is to measure the integrated area of the α relaxation peak in the frequency domain or the amplitude of the corresponding feature in the time domain. This requires that the measurement method have sufficient dynamic range to include the entire α relaxation feature (usually several decades at a single temperature), and that the α feature be well separated from other contributions to the frequency-dependent or time-dependent signal. In Chapter 3 we have presented theoretical results showing how $f_q(T)$ and T_c can be determined in this manner through BS in the frequency domain or impulsive stimulated thermal scattering (ISTS) in the time domain. Contributions due to longitudinal acoustic waves, structural (α) relaxation, and thermal diffusion (i.e. Brillouin, Mountain, and Rayleigh modes respectively) appear in both BS and ISTS data, in the former as spectral features resulting from spontaneous fluctuations and in the latter as time-dependent responses to sudden heating with short, crossed excitation laser pulses. In favorable cases, the three features are well separated. Since the thermal diffusion and acoustic features are strongly q-dependent and the Mountain mode is essentially q-independent at low q, the BS or ISTS wavevector can be varied to optimize the separation of the Mountain mode from the other features as the sample is cooled and the structural relaxation dynamics (or relaxation spectrum) shift from fast to slow time scales (high to low frequencies). In practice, unique determination of α relaxation dynamics and amplitudes is currently possible over a far wider wavevector range through ISTS than BS, mainly because ISTS experiments at very small wavevectors (small excitation angles) and measurements of very slow responses (out to millisecond time scales) are not difficult.

To explore the capabilities for determination of Mountain mode dynamics, the Debye-Waller factor $f_{q\to 0}(T)$, and T_c, and for testing of mode-coupling theoretical predictions, we have performed ISTS experiments on the glass-forming liquid salol. This sample was selected for initial measurements in part because it is one of only a few liquids for which neutron scattering determination of $f_q(T)$ at high q (and from the observed square-root cusp, a value of T_c) has been reported. A baseline for comparison to our results therefore exists. Determination of whether $f_q(T)$ values at low q (which are expected to differ substantially from those at high q) show the square-root cusp predicted by MCT and, if so, whether this yields the same value of T_c, offer the possibility of a stringent test of MCT over essentially the complete range of wavevectors.

In Sec. 4.2, we describe experimental methods. Qualitative features of ISTS data are described in Sec. 4.3. In Sec. 4.4, data are analyzed quantitatively and the results for the Debye-Waller factor $f_{q\rightarrow 0}(T)$ and Mountain mode dynamics are presented. Discussion and conclusions follows in Sec. 4.5.

4.2 Experimental Methods

Salol (phenyl-salicylate, melting point $T_m = 315$K, calorimetric glass transition temperature $T_g = 218$K) was purchased from Aldrich Chemical Company (nominal purity 99%) in crystalline form. The material was placed in a beaker covered with pinholed aluminum foil and stored overnight in a 95 °C oven for dehydration. This was important to avoid formation of ice crystals in the samples at around 0 °C. The dehydrated liquid salol was loaded using a syringe and a 0.22 μm millipore Teflon filter into the sample cell, which was also dried in the oven overnight. With this procedure no crystallization occurred during the course of experiments, and the samples could be used for months. The sample cell has movable quartz windows [76] to minimize stress due to sample contraction upon cooling. This avoids cell window breakage and sample cracking that otherwise may occur upon cooling through the glass transition temperature. The sample cell was attached to the cold finger of a closed-cycle cryostat. Temperatures were measured using a platinum RTD immersed inside the sample, and temperature control was accurate to ±0.05K. Temperature variations within the sample were less than 0.2 K from top to bottom, as determined through ISTS measurement of the acoustic velocity in different sample regions. The experiments reported here were conducted with a quasi-CW probe system as shown in Fig. 2-2.

Data were collected with excitation angles of 1.31°, 2.17°, 3.03°, 4.68°, 7.22°, 12.25°, and 45.12°, corresponding respectively to scattering wavevectors of 0.1354, 0.2235, 0.3120, 0.4826, 0.7433, 1.260, and 4.532 μm^{-1}. The angles were measured mechanically using a calibrated rotation stage, and are accurate to ±0.05°. The corresponding wavevectors were determined through Eq. 2.1. For angles smaller than 10°, the relative error introduced by this method of angle measurement becomes unacceptably large and an alternative method for wavevector determination was used. The acoustic velocities $c = \omega_A/q$ at several high sample temperatures were first determined from ISTS measurements of the acoustic frequency ω_A at large wavevectors q. Similar measurements were then made at the lower wavevectors (smaller scattering angles). Since the acoustic velocity at high temperature is q-independent in our wavevector range, the lower wavevector values were then calculated. This procedure was repeated at several high temperatures, and the uncertainties in the smaller wavevector values were $\pm 0.0005\ \mu m^{-1}$. The wavevectors determined in this manner yielded values of the excitation angles which were in agreement with those measured using the rotation stage.

Data were collected upon cooling of the sample from 400K to 215K in intervals of 5K in high and low-temperature regions and 2.5K at temperatures which showed strong relaxation modes signals. Before recording data, the temperature was allowed to stabilize for about 10 minutes to within ±0.05K of the desired temperature.

Excitation at the highest scattering angle resulted in acoustic frequencies exceeding the 1-GHz bandwidth of the detection electronics. For this angle, the acoustic data were collected with the pulse probe system, and the relaxation and thermal diffusion responses were recorded with the quasi-CW probe system. The two sets of data were then combined to give the complete ISTS response at each temperature.

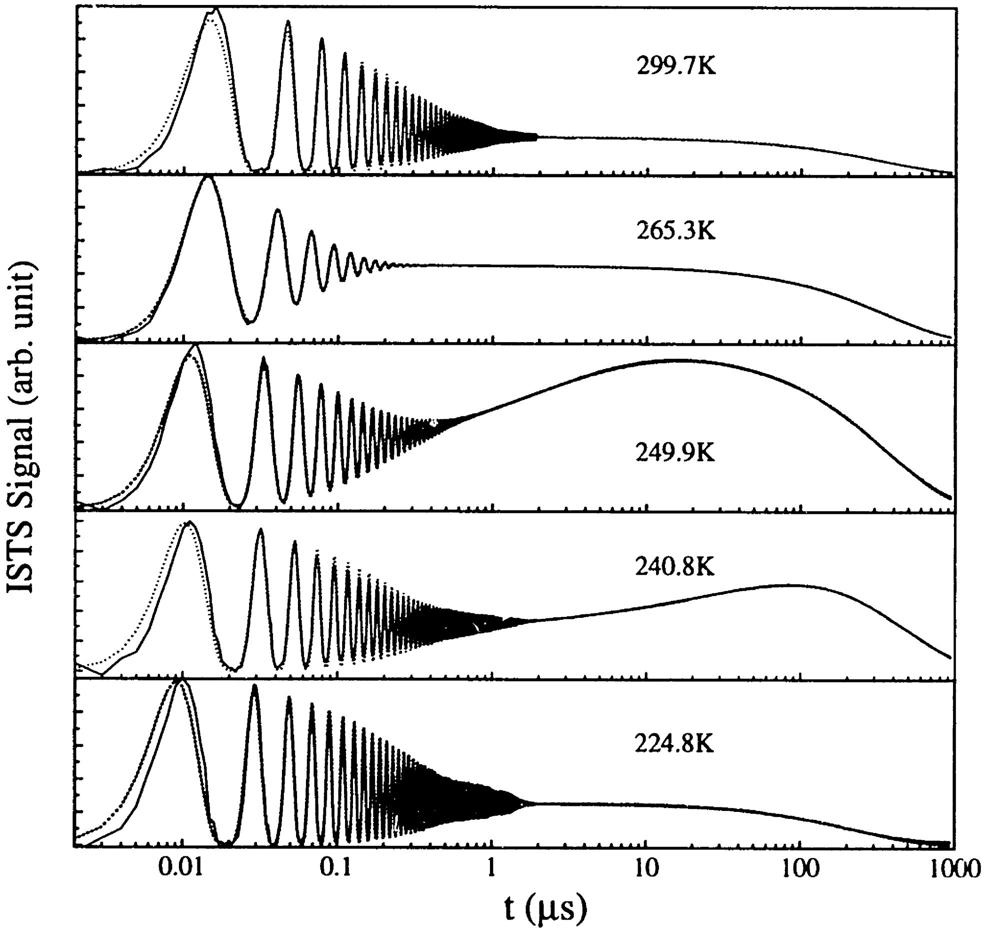

Figure 4-1: ISTS data (dotted curves) and fits (solid curves) from salol at wavevector $q = 0.1352\ \mu m^{-1}$ at several temperatures. At all temperatures, the signal shows damped acoustic oscillations at short times and thermal diffusion at long times. At intermediate temperatures, an additional structural relaxation mode which manifests itself as a gradual rise appears.

4.3 Qualitative Data Features

Typical ISTS data at high, intermediate and low temperatures at excitation wavevector magnitude $q = (0.1354 \pm 0.0005)\ \mu m^{-1}$ are displayed in Fig. 4-1. At all temperatures, the data exhibit damped acoustic oscillations and a steady-state signal level which decays due to thermal diffusion. At intermediate temperatures the steady-state signal level is reached gradually, reflecting slow, nonexponential structural relaxation dynamics,

At high temperatures (above 299.7K) where structural relaxation occurs on a time scale faster than half the acoustic oscillation period $\pi/\omega_A(q)$, the relaxing liquid behaves like a normal liquid and data can be described with the first ("A") term only in Eq. 3.49. Following sudden, spatially periodic heating, thermal expansion at the grating peaks leads to a density modulation which oscillates about the steady-state level. After the acoustic oscillations are fully damped, the steady-state density modulation (and ISTS signal) slowly decays through thermal diffusion. This corresponds to the low-frequency limit discussed in Chapter 3.

As the temperature is decreased, structural relaxation slows down. When its time scale becomes comparable to the acoustic oscillation period (i.e. the structural relaxation spectrum overlaps the acoustic frequency), the sample can no longer reach its steady-state response to the oscillating acoustic stress and so the sample compliance at the acoustic frequency is reduced. This increase in stiffness results in a higher acoustic velocity, which appears in ISTS data as a higher frequency. Mechanical lag between the oscillating acoustic strain and the other structural responses of the sample also give rise to additional acoustic damping. The temperature-dependent acoustic velocity and attenuation rate are shown in Fig. 4-2. In addition, the slow components of structural relaxation are observable directly in the ISTS data as a gradual rise in signal, described by the stretched exponential term in Eq. 3.49. This is the time-domain analog of the Mountain mode in the light-scattering spectrum. It can be observed in ISTS data when significant structural relaxation occurs on time scales slower than the acoustic oscillation period.

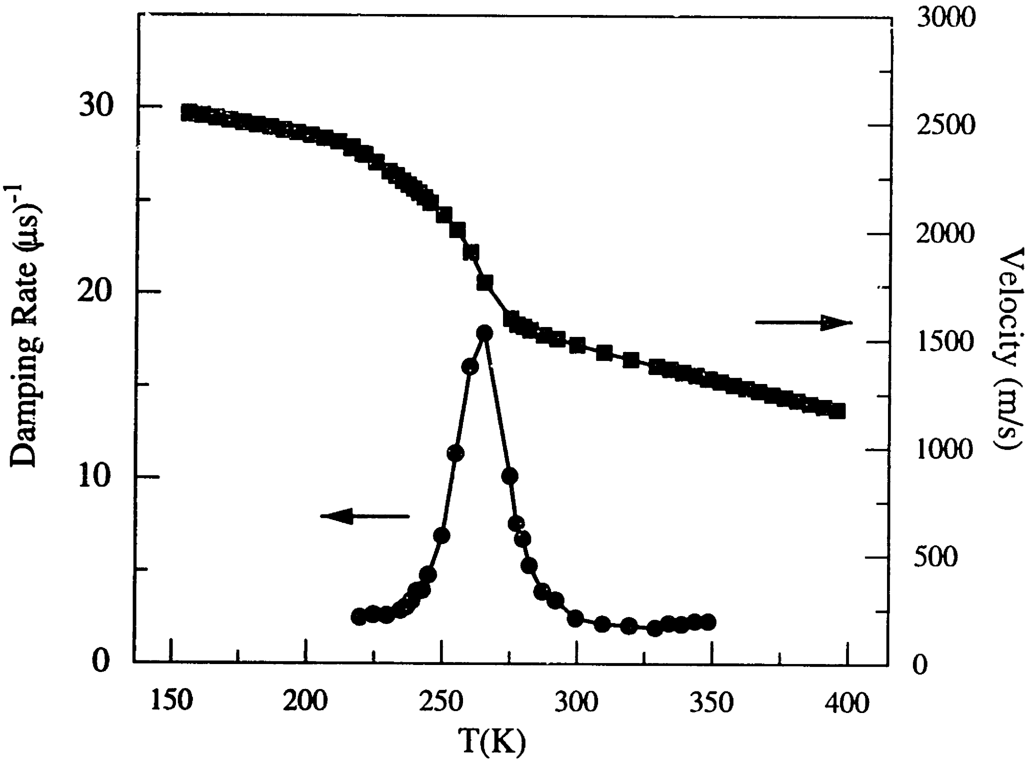

Figure 4-2: Temperature dependences of longitudinal acoustic velocities (solid circles) and damping rates (solid squares) from fits to ISTS data at $q = 0.1352\ \mu m^{-1}$. As the temperature is lowered, the sound velocity starts to deviate from $c_0(T)$ at about 295 K due to slowing structural relaxation dynamics which overlap the acoustic oscillation period. The sound velocity increases to $c_\infty(T)$ as the temperature is lowered further and the structural relaxation dynamics become very slow compared to the acoustic oscillation period. The damping rate shows a maximum when the relaxation spectrum overlaps with the acoustic frequency at about 265K. Solid lines are guides to eyes.

As the sample is cooled further, the structural relaxation dynamics become substantially slower than the acoustic period. On the time scale of the acoustic period, the sample is therefore solid-like and so displays a high acoustic velocity and low acoustic attenuation rate. On slower time scales, the gradual volume response to heating is observed directly. ISTS signal rises to its steady-state value, and finally decays due to thermal diffusion. The structural relaxation dynamics, i.e. Γ_R and β in Eq. 3.49, can be well characterized. Meanwhile, in the data recorded with the 1.31° scattering angle, as represented by Figs. 4-1 and 4-2, the Debye-Waller factor can be determined from the amplitude ratio through Eq. 3.46 in the 250-238.8 K temperature range within which the structural relaxation time Γ_R^{-1} is much longer than the acoustic period but much shorter than the thermal decay time. Thus, the condition $\omega_A \gg \Gamma_R \gg \Gamma_H$ for separation of the Brillouin, Mountain, and Rayleigh features and for Eq. 3.46 to hold is satisfied.

At temperatures below 238.8 K, the structural relaxation dynamics become comparable to or slower than the thermal diffusion time at the excitation wavevector chosen, and so the signal decays substantially due to thermal diffusion between grating peaks and nulls before the gradual rise of the Mountain mode has a chance to reach its steady-state level to the initial temperature jump at the peaks. This makes continued characterization of the relaxation dynamics or the Debye-Waller factor difficult. At very low temperatures, structural relaxation is substantially slower than thermal diffusion and, as at high temperatures, the signal can be described by only the "A" term of Eq. 3.49.

The temperature range over which structural relaxation dynamics and the Debye-Waller factor can be determined can be increased by varying the wavevector magnitude q, since the acoustic and thermal diffusion responses are q-dependent while in the range accessible to ISTS the Mountain mode is not. The range can be extended to lower T by using smaller wavevectors, at which the (q^2-dependent) thermal diffusion dynamics can be slowed considerably to permit observation of the gradual rise. With larger wavevectors, the (q^{-1}-dependent) acoustic period can be reduced to permit observation of the Mountain mode at higher temperatures. Varying the wavevector also permits characterization of the q-dependent acoustic velocities and attenuation rates, from which relaxation dynamics on the acoustic time scales can be deduced. In Fig. 4-3, we show the raw data (solid curves) and fits (dotted curves) by Eq. 3.49 for temperatures from 268.7K to 240.8K collected at highest and lowest wavevectors. It is evident from Fig. 4-3 that upon increasing temperature the relaxation shifts toward shorter times.

4.4 Quantitative Analysis and Results

Here we present analysis of the Mountain mode dynamics and amplitudes, and comparison of the results to MCT predictions. Analysis of the acoustic response will be presented in Chapter 6.

Since salol weakly absorbs the excitation light due to O-H vibrational overtone absorption at 1.064 $\mu m, G_{\rho T}(q,t)$ is the dominating term in Eq. 3.1, especially at small q due to the linear q-dependence of the amplitude of $G_{\rho\rho}(q,t)$. Data collected at angles below 15° were fit to Eq. 3.3 with $G_{\rho T}(q,t)$ given by Eq. 3.49. At large q corresponding to excitation angles above 15°, $G_{\rho\rho}(q,t)$ in Eq. 3.48 was included in the fits to data.

The solid lines in Fig. 4-1 represent the fits to data (dotted lines) at wavevector $q = 0.1354\ \mu m^{-1}$. The fitting parameters for acoustic velocity and damping rate at this wavevector are plotted as a function of sample temperature in Fig. 4-2. As discussed above, the acoustic velocity increases and the attenuation rate goes through a maximum as the temperature is cooled. At higher wavevectors, these changes occurred in higher temperature ranges at which the structural relaxation spectrum overlapped the higher acoustic frequencies.

The thermal decay rates Γ_H were determined from the long-time decays in ISTS signal. At each temperature, they showed the expected q^2-dependence as illustrated in Fig. 4-4. The slope of the linear fit ($\Gamma_H = D_T q^2$) gives the thermal diffusivity whose temperature dependence is plotted in Fig. 4-5, which shows a smooth variation above 238K and below about 230K, but a very rapid change between these temper-

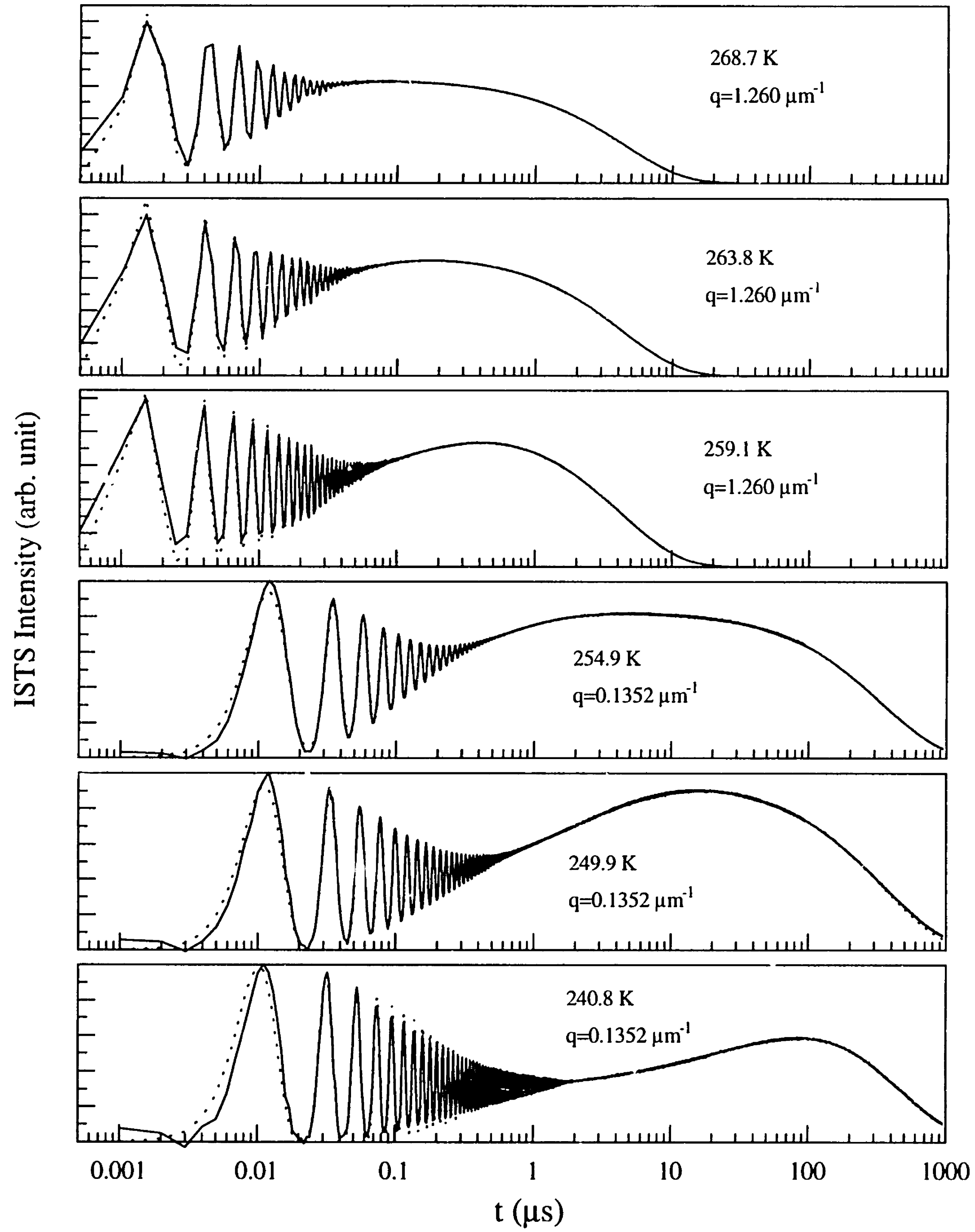

Figure 4-3: ISTS data (solid curves) and fits (dotted curves) by Eq. 3.49 of salol in the intermediate temperature range collected at two different wavevectors. Signal shows damped acoustic oscillations, and reaches a stead-state level rapidly at high temperatures and more slowly (due to slow structural relaxation or Mountain mode) at low temperatures. Signal decays at long times due to thermal diffusion.

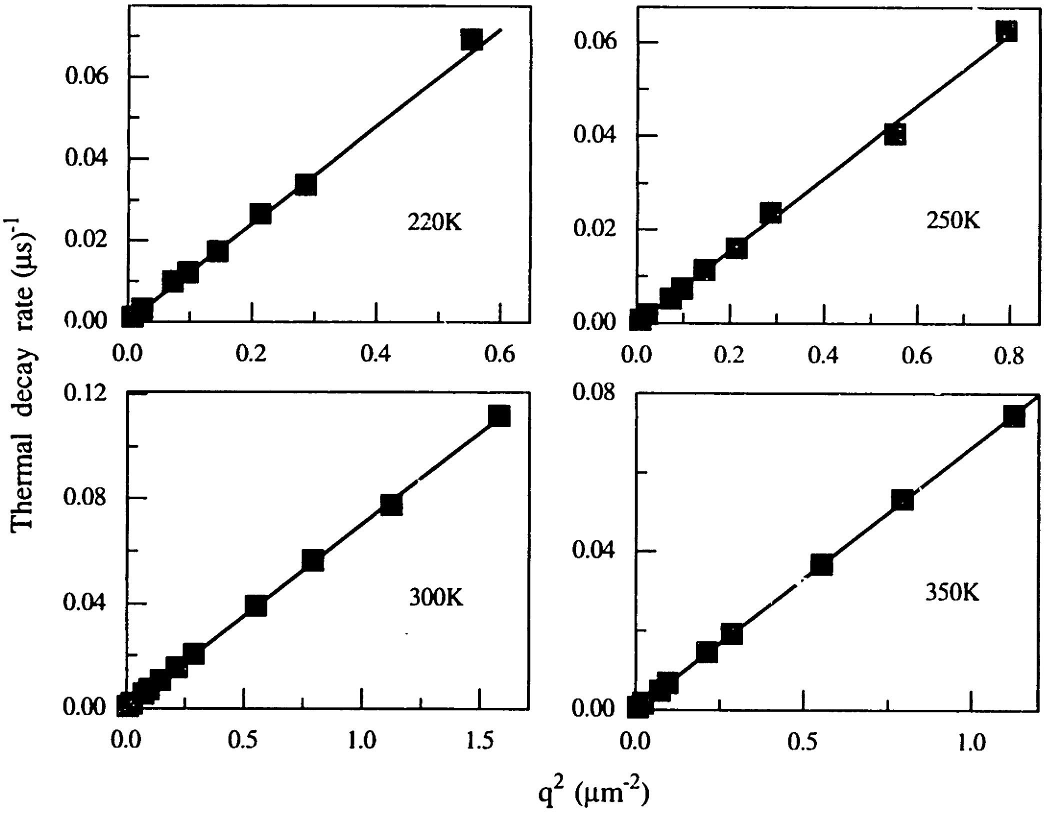

Figure 4-4: Thermal decay rates vs q^2 at four representative temperatures from 390K to 220K. At all temperatures, thermal decay rates show a linear q^2-dependence. The slope of the line determines the thermal diffusivity.

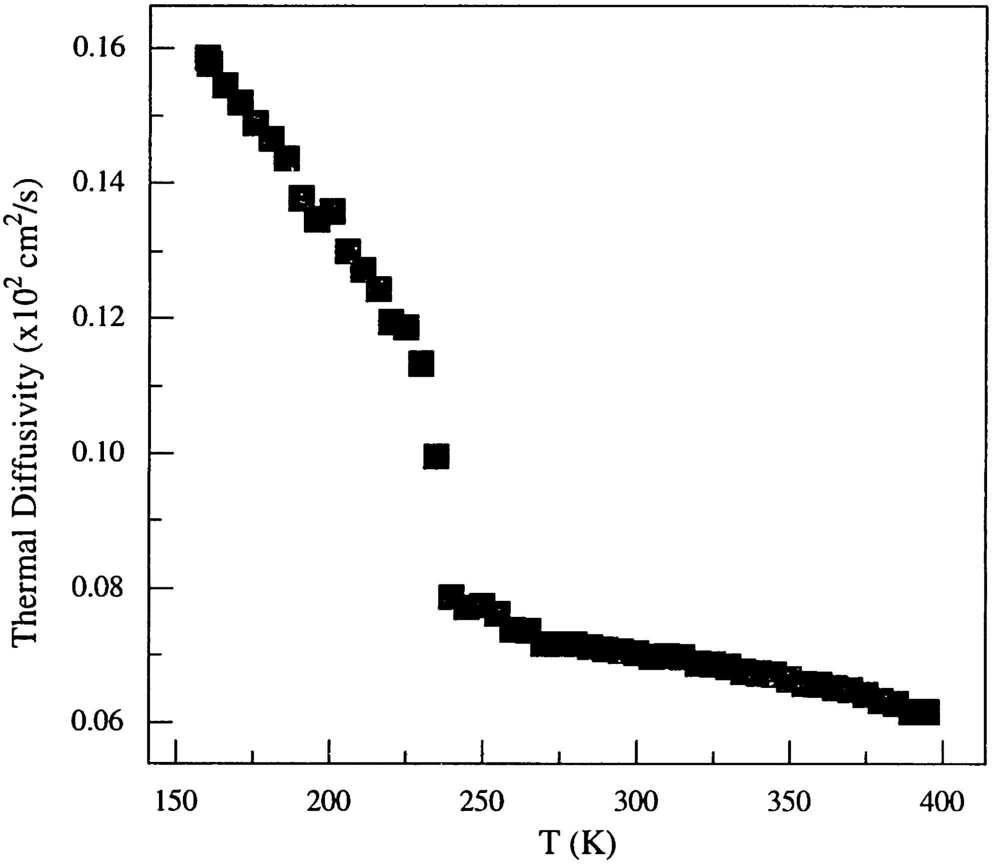

Figure 4-5: Temperature dependence of the thermal diffusivity D_T measured in this study, showing smooth variation above about 238 K and below 230K. As T is decreased between these values, a rapid rise in D_T is observed. Above 215 K, the thermal diffusivities were determined by the slopes of the linear q^2-dependent thermal decay rates and below 215 K, they were obtained from the measurement at one angle, i.e. thermal decay rate divided by q^2.

atures. This is presumably connected to the rapid drop in the value of the specific heat c_p measured through differential scanning calorimetry [77, 78], since thermal diffusivity D_T is determined by $\lambda/(\rho_0 c_p)$ and the thermal conductivity λ shows no dispersion through the liquid-glass transition [79]. Note that the temperature range of rapid variation is higher than the glass transition temperature $T_g = 218$K at which the specific heat, measured on very slow (many seconds) time scales, undergoes substantial change. This is because ISTS measurements of D_T are made on the time scales of thermal diffusion across micron distances, i.e. microsecond-millisecond rather than many second time scales. ISTS data show changes in D_T when the structural relaxation dynamics move through microsecond-millisecond time scales, which occurs at temperatures higher than those at which the relaxation dynamics reach time scales of many seconds.

4.4.1 Mountain Mode Dynamics

From fits to the data at temperatures where the Mountain mode is apparent, the dynamic parameters Γ_R and β as well as the relative amplitudes of A and B were determined. To display the structural relaxation function $\phi(t;T)$ directly, the acoustic and thermal diffusion signals, described by Eq. 3.49 and fitting parameters Γ_H, ω_A and Γ_A, were subtracted from the square root of the data. The resulting relaxation functions $\phi(t;T)$, whose strengths were determined by $B/(A+B)$, are shown for several temperatures in Fig. 4-6. To check the relaxation dynamics parameters, the relaxation functions shown in Fig. 4-6 were fit with the stretched experimental function (dashed curves) to determine again the values of Γ_R and β which in all cases agreed well with those from the original fits. It is evident from Fig. 4-6 that upon decreasing temperature the relaxation dynamics shift toward longer times.

To compare the relaxation dynamics determined from different techniques, the average relaxation times $<\tau_R>$ were calculated from the fitting parameters β and $\tau_R = \Gamma_R^{-1}$. The temperature-dependences of the dynamical parameters β, τ_R and $<\tau_R>$ are listed in Table 4.1. The values of β and τ_R were determined from data at several wavevectors wherever separation of the Mountain and other modes made this possible. The values are determined uniquely with reasonable accuracy in the 238-281K temperature range, although at the higher temperatures in this range the accuracy is reduced somewhat due to limitations in detection bandwidth.

The fitting parameter β, together with the values obtained from depolarized light scattering [9] and photon correlation spectroscopy [68] measurements, are plotted in Fig. 4-7. The β values from this study are essentially constant at 0.52 ± 0.03 in the 238.8-260.1K temperature range. This is verified in Fig. 4-8 which shows a rescaled plot of structural relaxation functions determined from data in this range.

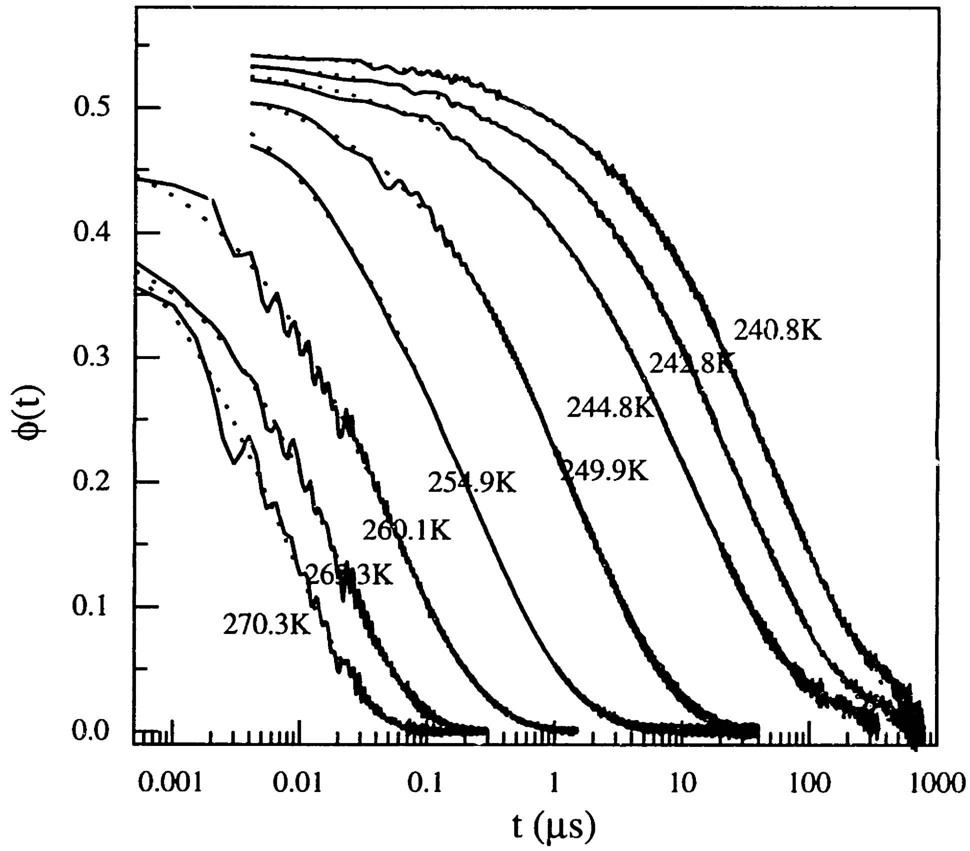

Figure 4-6: Structural relaxation functions $\phi(t;T)$ extracted from ISTS data (solid curves) and their KWW fits (dotted curves) of salol from 240.8 K to 270.3 K. Upon increasing temperature the relaxation time decreases.

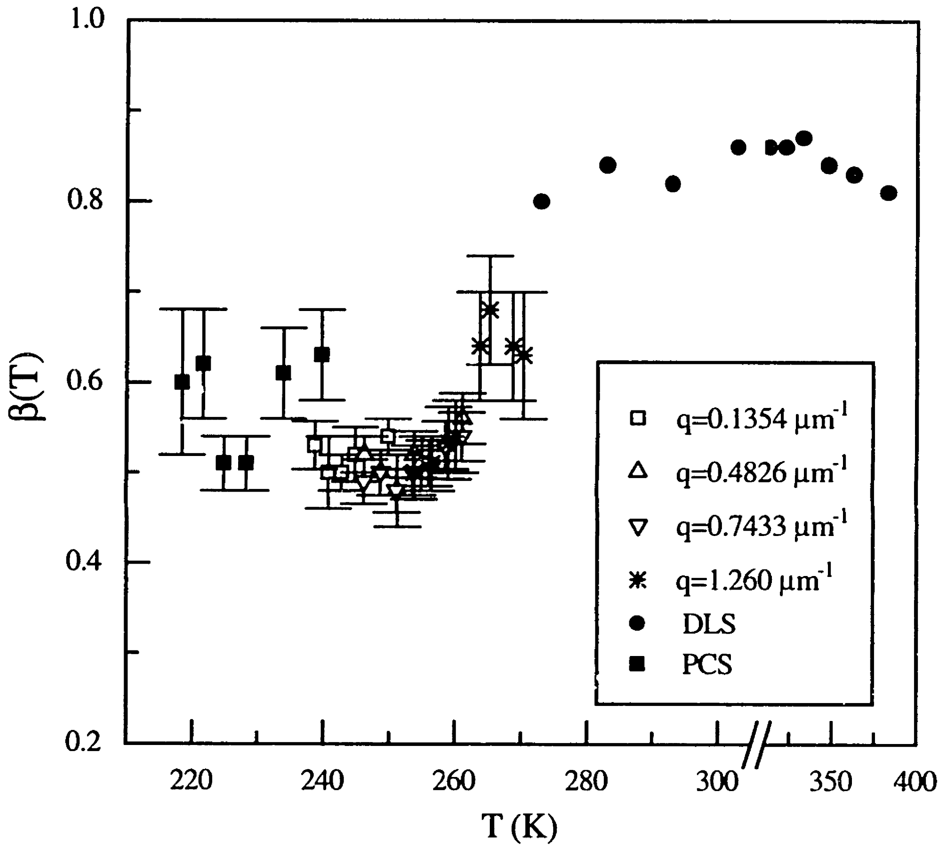

Figure 4-7: Stretching parameters β determined in this study, as well as from DLS and PCS as a function of temperature. Low-T data from this measurement show an essential T-independence with $\beta = 0.52 \pm 0.03$.

Table 4.1: Fitting parameters for the structural relaxation dynamics of salol and the average relaxation time at various temperatures.

T(K)	$\tau_R(\mu s)$	β	$<\tau_R>$ (μs)
270.3	0.0050	0.63 ± 0.07	0.007
268.6	0.0067	0.64 ± 0.06	0.009
265.2	0.0149	0.68 ± 0.06	0.019
263.7	0.0188	0.64 ± 0.06	0.026
260.0	0.0413	0.54 ± 0.04	0.072
259.0	0.0642	0.51 ± 0.04	0.124
256.0	0.0867	0.51 ± 0.03	0.165
253.6	0.1970	0.50 ± 0.02	0.400
251.2	0.4285	0.48 ± 0.04	0.915
249.9	1.291	0.54 ± 0.02	2.237
246.2	3.560	0.52 ± 0.02	6.588
244.8	9.556	0.52 ± 0.03	17.57
242.8	26.66	0.50 ± 0.02	49.57
240.8	67.09	0.50 ± 0.04	134.2

The β values at low T determined through ISTS are in agreement with those determined through from PCS measurements, within experimental uncertainties of the latter. The β values determined through PCS, ISTS, and DLS measurements show a sigmoidal shape with most of the variation at temperatures of around 265 K, which will be shown below to be near the crossover temperature T_c. MCT predicts temperature-independent α relaxation stretching above T_c [9], but makes no explicit predictions on T-dependent β values around and below T_c. Temperature-dependent behavior similar to that reported here has been observed in other materials, often with the strongest temperature dependence in the vicinity of T_c [39].

In Fig. 4-9 we show the average relaxation times $<\tau_R>$ (T) determined from ISTS measurements at several wavevectors, as well as the $<\tau_R>$ values from DLS [9] and PCS [68]. The data from ISTS cover the gap between PCS and DLS measurements and show a smooth variation between the two. The agreement between the β and $<\tau_R>$ values found from ISTS and PCS in the overlap region supports the assumption in Chapter 3 that both techniques measure a similar dynamical quantity, although the ranges of time scales differ and ISTS, but not PCS, gains access to

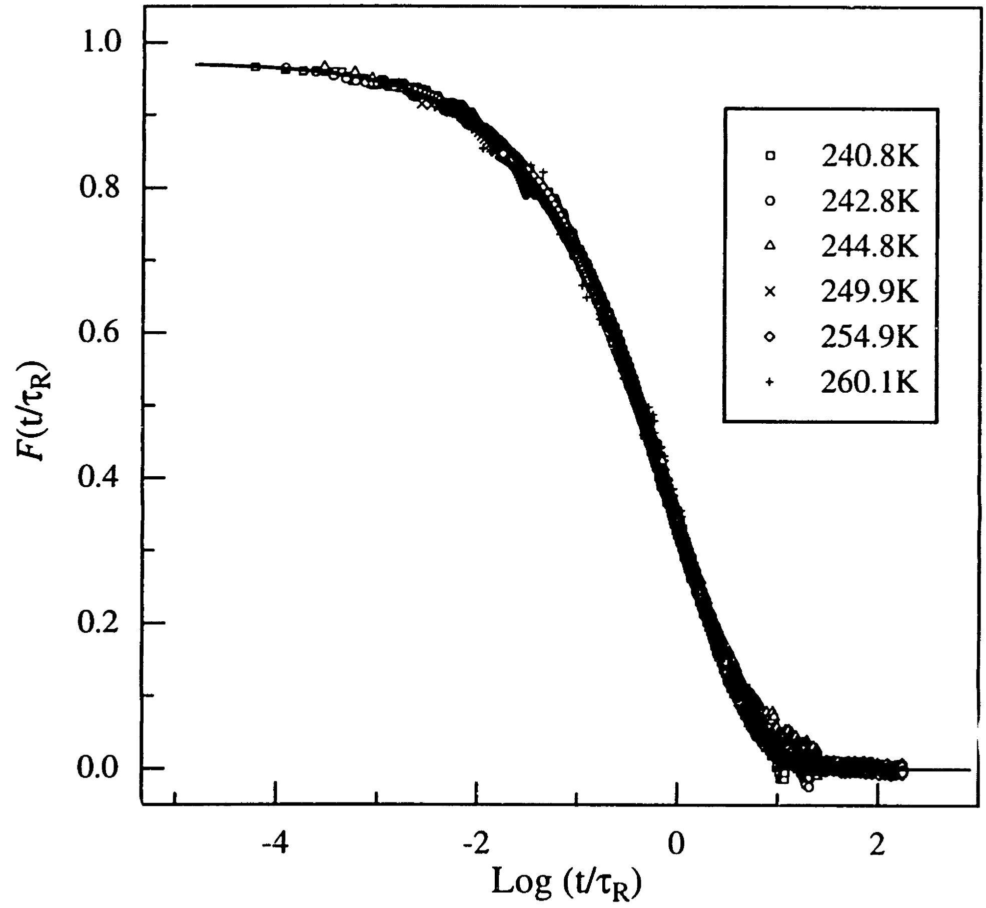

Figure 4-8: The rescaled plot of the data below 260.1 K shown in Fig. 4-6. The solid line represents a KWW master fit with $\beta = 0.52$.

the acoustic response and the Debye-Waller factor. While MCT predicts a power-law T-dependence of average relaxation time above T_c, its current status does not provide a straightforward prediction of the T-dependence of $<\tau_R>$ below T_c. We employ a widely used Vogel-Tamman-Fulcher Eq. 1.3 to fit data in the low-T regime, which yields $T_0 = 133 \pm 10$K, $T_{VTF} = 4790$ K, and $\tau^0_{VTF} = 3.0 \times 10^{-15}$ ns. These parameters are in accord with those obtained from dielectric measurements [5, 80] to within experimental uncertainties. The solid line in Fig. 4-9 represents the fit to Eq. 1.3. Although the VTF form appears to fit the low-T data very well, the unrealistically small value of $\tau^0_R = 3.0 \times 10^{-15}$ ns indicates that this functional form does not correspond to a physically meaningful model of the liquid-glass transition in salol.

4.4.2 The Debye-Waller Factor $f_{q\to 0}(T)$

It is straightforward to obtain the nonergodictiy parameter $f_{q\to 0}(T)$ from ISTS data where the condition $\omega_A(q;T) \gg \Gamma_R(T) \gg \Gamma_H(q;T)$ was found to be satisfied. For each wavevector q, we chose $\Gamma_R(T) \geq 10\Gamma_H(q;T)$ and $\Gamma_R(T) \leq 10\omega_A(q;T)$ as criteria for determination of $f_{q\to 0}(T)$ values through Eq. 3.46 from fitting parameters A and B. The resulting $f_{q\to 0}(T)$ values (symbols) are plotted in Fig. 4-10 along with a fit to the square-root cusp behavior (solid curve) predicted by MCT, described by Eq. 1.26. The fit yields parameters $f^c_{q\to 0} = 0.36 \pm 0.01$, $h_{q\to 0} = 0.55 \pm 0.05$, and $T_c = 266K \pm 1K$. Note that $f^c_{q\to 0}$, which may weakly depend on temperature, is held to be constant for simplicity. It is seen that the nonergodicity parameter shows a cusp at about 266K. This T_c value is in good agreement with neutron scattering results of $T_c = (263 \pm 7)$ K at $q = 1.5$ Å^{-1} and $q = 1.0$ Å^{-1} [75], which confirms a q-independent value for T_c. This result is also consistent with the previous determination $T_c = (256 \pm 5)$ K from DLS [9].

Note that MCT predicts two-step relaxation dynamics: the strongly T-dependent α relaxation as discussed here, and a weakly T-dependent, faster β relaxation. In principle, the response function $G_{\rho T}(q,t)$ is given by Eq. 3.67, which includes the β relaxation contribution. As described in Chapter 3, β relaxation has been found

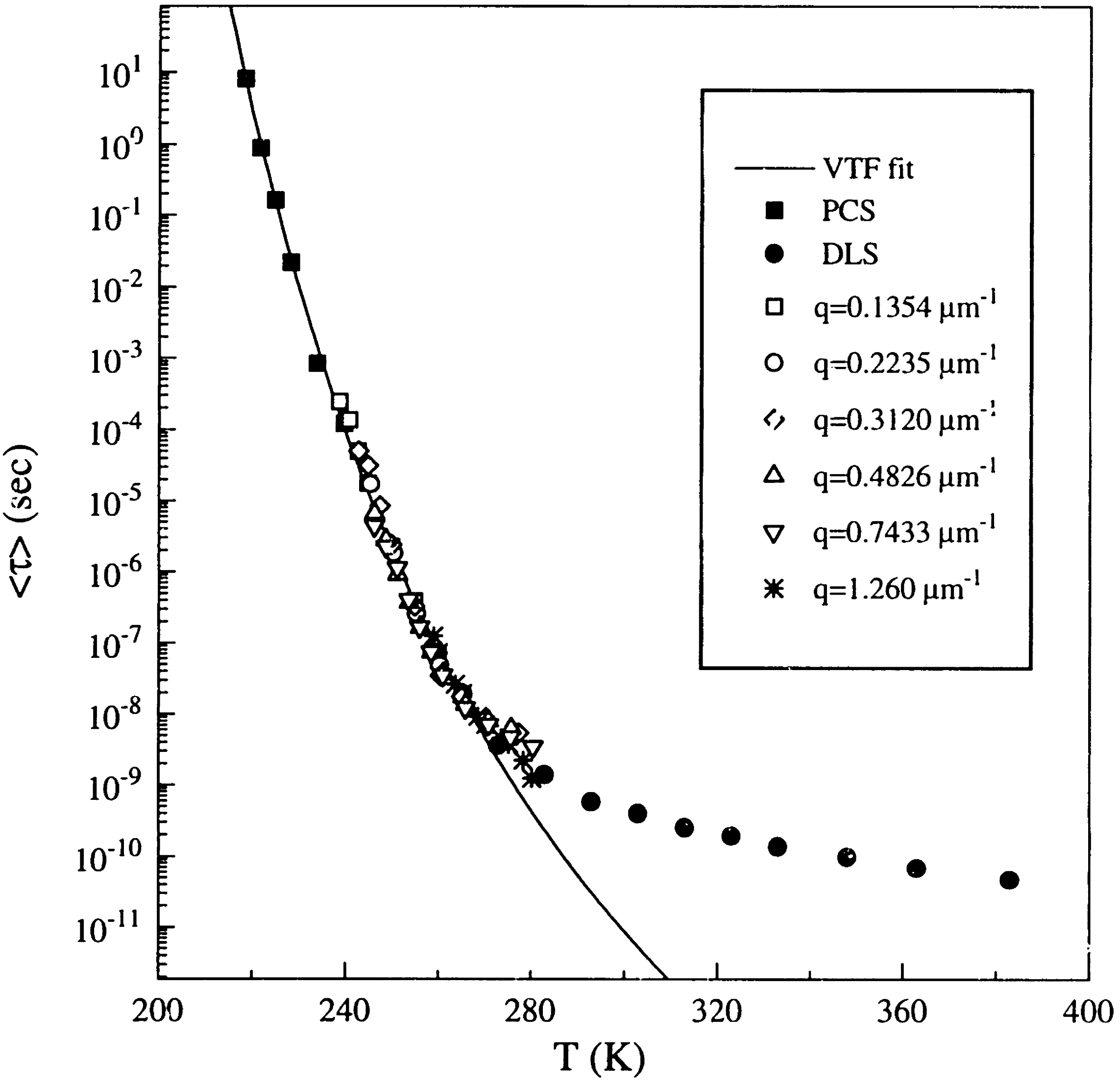

Figure 4-9: Temperature dependence of $<\tau>$ from ISTS data at several wavevectors, previous depolarized light scattering, and photon correlation spectroscopy. Data from ISTS cover the gap between DLS and PCS and form a smooth curve. The solid line represents a VTF fit to the low-T data. The fit follows the low-T data very well. However, the fit yields an unrealistically small value of the quantity $\tau^0_{VTF} = 3.0 \times 10^{-15}$ ns. This indicates that VTF does not provide a useful physical description of the temperature dependence of the average relaxation time of salol.

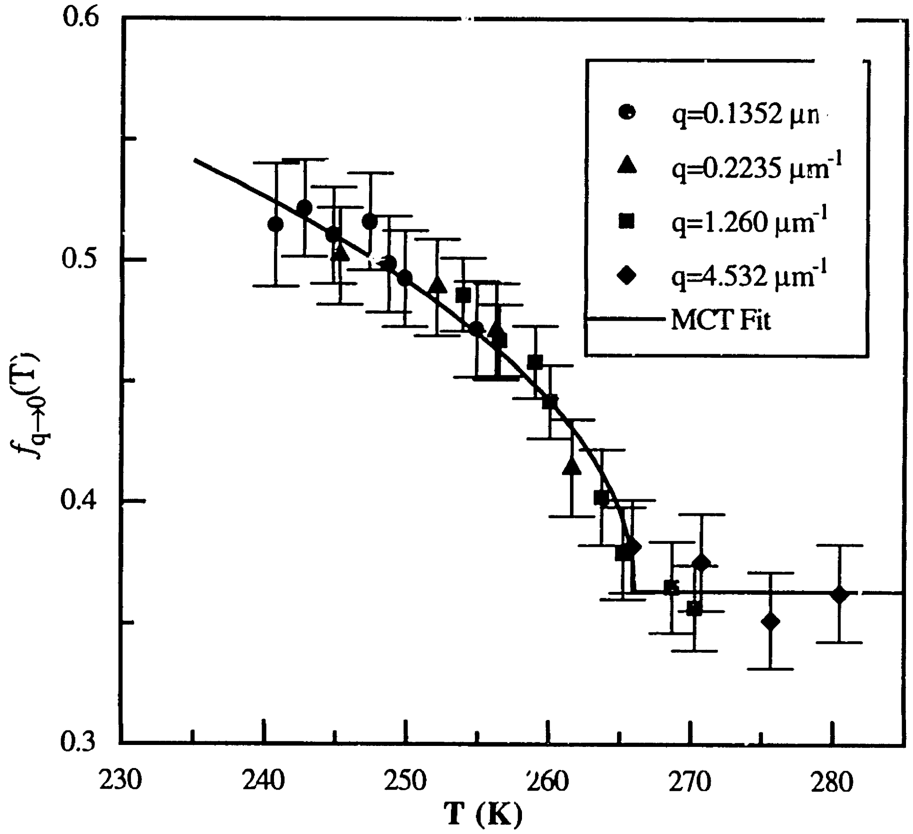

Figure 4-10: Debye-Waller factor $f_{q\to 0}(T)$ (symbols) of salol versus T, obtained from ISTS data at several wavevectors via Eq. 3.46. The results show a square-root cusp at about 266K. The solid line represent a MCT fit to Eq. 1.26.

in salol [9] and propylene carbonate [69] at all temperatures to occur on faster time scales than those observed in the ISTS experiments reported here. β relaxation has been found to affect the acoustic part of ISTS signal [34], consistent with the overlap between the β relaxation spectrum and acoustic frequencies of 1 GHz or higher which are observed at high wavevectors. In Chapter 6, we will present the analysis of the β relaxation through acoustic modulus spectra.

4.5 Discussion and Conclusion

ISTS experimental data recorded from the glass-forming liquid salol with a quasi-CW probe system have been presented. The data, extending over nanosecond-millisecond time scales, permit determination of the acoustic, thermal diffusion, and Mountain mode dynamics and the Debye-Waller factor over wide temperature ranges. The MCT prediction of a square-root cusp in the Debye-Waller factor at a temperature T_c was confirmed. The value of $T_c = 266$K is consistent with neutron scattering and DLS results, which indicates the q-independence of T_c.

The values determined for the width of the relaxation spectrum, measured by the stretching parameter β, show a sigmoidal shape with most of the variation at temperatures around T_c, indicating dynamical changes suggested by MCT.

ISTS provides nearly the only alternative to neutron scattering for determination of the Debye-Waller factor and therefore for testing of the central MCT prediction concerning its temperature-dependent behavior. Unlike neutron scattering, which requires a multi-user experimental facility and extensive time and material commitments, ISTS experiments can be conducted in a few seconds on a single laser table with standard lasers and high time resolution. Besides, the cutoff frequency problem encountered in neutron scattering is avoided in ISTS by collecting the data at different wavevectors. It is the wide wavevector range accessible to ISTS and the wide dynamical range that make it possible for the determination of the Debye-Waller factor and the relaxation dynamics over a wide temperature range.

The current apparatus of ISTS provides a window from ns to ms which permits characterization of the α relaxation mode directly in the time domain. Besides the acoustic and thermal diffusion modes, the α relaxation strength and dynamics can be measured whose results can be used to compare to the MCT predictions. In this initial demonstration, measurements were made which confirmed earlier neutron scattering results and showed the wavevector-independence of the T_c value. The results also confirmed our theoretical analysis of the ISS on glass-forming liquids described in Chapter 3. In Chapter 5, we will extend ISTS studies onto an ionic glass former.

Chapter 5

The α Relaxation Dynamics and the Debye-Waller Factor Anomaly in $Ca_{0.4}K_{0.6}(NO_3)_{1.4}$

In Chapter 4 we have presented our very first ISTS experiment study of an organic molecular glass former salol for the determination of the α relaxation strength, or the Debye-Waller factor, as well as the relaxation dynamics. The wide dynamical and wavevector ranges make it possible in ISTS data for the separation of the acoustic, relaxation or Mountain, and thermal diffusion modes in time. Thus it permits precise measurements of the relaxation dynamics and the relaxation strength, in addition to the acoustic and thermal diffusion dynamics. From the temperature dependence of the Debye-Waller factor, a crossover temperature T_c is identified which is consistent with other measurements. This finding, on the one hand, provides support for the MCT idea of the dynamical crossover at a wavevector independent temperature T_c. On the other hand, it confirms our theoretical analysis of the ISS technique described in Chapter 3. Previous experiments [33, 48-53] have shown that ISS is a useful tool for characterizing acoustic dynamics in the MHz-GHz frequency window. Our theoretical and experimental studies described in Chapters 3 and 4 have first demonstrated that ISTS is also a powerful tool for measuring the relaxation mode dynamics in a time range from nanoseconds to milliseconds and, most importantly, the amplitude of the relaxation mode or the Debye-Waller factor. Both the dynamical information in this time range and the temperature dependence of the Debye-Waller factor are crucial to the testing of MCT predictions.

For the second model system, we chose the much studied ionic glass-former $Ca_{0.4}K_{0.6}(NO_3)_{1.4}$. In this Chapter[1] we present results of our impulsive stimulated thermal scattering study of CKN concerning the Mountain mode dynamics and strength.

5.1 Introduction

The ISTS experiment provides information on structural relaxation dynamics spanning sub-nanosecond through millisecond time scales, connecting the higher-frequency (sub-GHz and above) regimes ordinarily studied through depolarized light scattering and Brillouin scattering with the microsecond and slower time scales examined through photon correlation spectroscopy. Access to this temporal range permits critical testing of MCT predictions concerning α relaxation dynamics and strength.

ISTS measurements are complementary to those of several other experimental techniques. In terms of the range of time scales, ISTS provides access to sub-nanosecond through millisecond regimes and therefore can complement dynamical information obtained through polarized and depolarized light scattering spectroscopies (sub-GHz through several THz regimes for the latter) and photon correlation spectroscopy ($10^{-6} - 10^{2}$ second temporal range). DLS measurements have permitted testing of MCT predictions of α and β relaxation scaling for several glass-forming materials including CKN [10, 82]. PCS experiments [11, 12] have revealed stretched-exponential α relaxation dynamics in CKN on microsecond and slower at temperatures near the liquid-glass transition temperature T_g. Impulsive stimulated scattering measurements on CKN, conducted with an early version of the experimental apparatus [34, 48], provided access to some of the intermediate temporal range with a signal-to-noise ratio insufficient for examination of the Debye-Waller

---

[1] Some of the materials in this Chapter have been published in Refs. [72, 81].

factor. In Chapter 4, we present an ISTS measurements on the molecular glass former salol and demonstrate the current capabilities for reliable determination of $f_q(T)$, and showed the predicted temperature-dependent square-root cusp at a temperature which matched the value of T_c determined through neutron scattering measurements of $f_q(T)$. In addition, the α relaxation dynamics were found to be fit well by a stretched exponential function with values of the exponent β that were essentially temperature-independent except near T_c, where they decreased rapidly with temperature. These results supported the MCT picture of a change in the diffusion mechanism at temperatures around T_c.

The Debye-Waller factor can be determined at high wavevectors from the integrated area of the quasi-elastic feature (due to α relaxation) in the neutron scattering spectrum. In CKN, a crossover temperature T_c was estimated at about 370K through measurements of $f_q(T)$ [2]. In addition, neutron spin-echo and time-of-flight results [3] showed the two-step (α and β) relaxation process and the scaling properties predicted by MCT.

In determinations of $f_q(T)$ through the integrated area of the quasielastic neutron scattering peak, there is a cutoff frequency ω_c which is often given by the size of the experimental frequency window. As discussed in Ref. [1] and in Chapter 1, the value deduced for f_q in practice depends on the precise choice of ω_c. If the value of ω_c is too large, β relaxation processes or even phonon features may be attributed to the α peak. If ω_c is too small, part of the α peak may be omitted. The problem becomes more serious at higher temperatures, since the α peak broadens to include higher frequencies. When this happens, a correction is needed [73] which introduces additional uncertainty in the f_q value. Similarly in neutron spin-echo measurements, if the α relaxation moves in the experimental window there is no obvious plateau in the correlation function $\Phi(q,t)$. As a consequence, the reading of the plateau value, i.e. the Debye-Waller factor is difficult. In this case one needs to know the inflection point t_i^β at which the β relaxation gives way to the α relaxation. But with the limited time range available to the measurements, it is difficult to determine t_i^β by itself. Sometimes one has to use the value from other measurements [75]. That is the case for CKN. In the first publication [2], the data $f_q(T)$ showed rapid decrease as increasing temperature, but did not exhibit an obvious cusp at T_c. Later, the data were given a more cautious interpretation [41].

The acoustic frequency in ISTS plays a role similar to the cutoff frequency in neutron scattering. However, the cutoff frequency problem can be avoided to some extent in ISTS. Since the acoustic frequency is proportional to the wavevector q, the cutoff frequency can go much higher by using large wavevectors so that the α relaxation can still be observed at elevated temperatures. Therefore the temperature range over which the Debye-Waller factors are determined is extended. In addition, since the acoustic response at light-scattering wavevectors is underdamped, it is easily identified and distinguished from the relaxational response.

In Sec. 5.2, we discuss the details of experimental arrangement. The experimental data are presented in Sec. 5.3. In Sec. 5.4 we present data analysis and comparison to theoretical predictions. Concluding remarks follow in Sec. 5.5.

5.2 Experiment

High-purity KNO_3 (99.999%) and $Ca(NO_3)_2\cdot 4H_2O$ (99.9995%) were purchased from Alfa Products. The appropriate amounts of KNO_3 and $Ca(NO_3)_2\cdot 4H_2O$ were dissolved in deionized water to make a (60 mol%) KNO_3 - (40 mol%) $Ca(NO_3)_2$ mixture. A small amount of $Na_2CrO_4\cdot 4H_2O$ (less than 5×10^{-3} mol%) was added to increase the absorption of the 355 nm excitation pulses. The mixture was filtered with a 0.22 μm millipore filter and dried in an oven ($\sim$ 550K) for at least 24 hours. The sample was then transferred into a 20 mm path-length cylindrical glass cell which was preheated to about 400K. A platinum RTD was held by a copper stopper and immersed inside the sample for temperature measurement. The sample cell was embedded inside a copper block which was heated with resistive heaters. Another platinum RTD was used to monitor the temperature of the copper block which was regulated with a Lakeshore temperature controller. The entire sample assembly was enclosed under vacuum. The sample was exposed to the vacuum environment through a small hole in the copper stopper of the optical cell. Before collecting data, the sample was slowly heated up to and kept at about 560K overnight in order to remove any residual water. With this procedure, no crystallization occurred during the entire course of experiments, even when the sample was cooled down to T_g very slowly and left at each temperature for several hours.

The ISTS experiments reported here were carried out with a system similar to that described in Chapter 2, but with a 355 *nm* excitation wavelength. The excitation source is a Q-switched, mode-locked, and cavity-dumped Nd:YAG laser which yields a 500 μJ, 1064 *nm* pulse of 100 *ps* duration at a repetition rate of up to 1 kHz. This output is first passed through a lithium triborate (LBO) crystal to yield light at 532 *nm*. The green light is then mixed with the remnant 1064 *nm* radiation in a β-barium borate (BBO) crystal to yield excitation pulses of approximately 10 μJ at 355 *nm*. The pulse is split with a 50% beamsplitter into two excitation pulses that are cylindrically focused and crossed at an excitation angle θ_E. The laser spots are about 100 μm high and 5 *mm* wide at the focus. As discussed in Chapter 2 the large width is necessary so that the laser-generated acoustic waves observed in ISTS measurements do not leave the excitation region before they are fully damped.

The quasi-CW probe system described in Chapter 2 was employed to detect the ISTS signal. That is, the electro-optically gated laser beam from a single-mode argon laser at 514 *nm* is incident at the Bragg angle for diffraction from the transient grating induced by the excitation pulses. Diffracted signal is directed into an amplified fast photodiode and temporally resolved with a digitizing oscilloscope. The digitized signal is transferred to a computer for storage and subsequent analysis.

ISTS measurements were performed with excitation angles of 2.90°, 2.01°, 1.33°, 1.09°, 0.76°, 0.75°, and 0.74°, which correspond to scattering wavevectors of 0.896, 0.623, 0.423, 0.336, 0.235, 0.232, and 0.227 μm^{-1}, respectively. The angles were measured mechanically using a calibrated rotation stage with an accuracy of $\pm 0.05°$. The corresponding scattering wavevectors were determined as follows. The acoustic velocities $c = \omega_A/q$ at several high temperatures were first determined from ISTS measurements of the acoustic frequencies ω_A at several large wavevectors whose values were determined through mechanical measurement of the excitation angle θ_E . Similar measurements of the velocities were then made at lower wavevectors. Since the acoustic velocity at high temperature is q-independent in our wavevector range, the lower wavevector values were calculated based on the velocity values. The measurements were repeated at several high temperatures and the results were averaged, yielding wavevector uncertainties of ± $0.002\mu m^{-1}$. Data were collected upon cooling of the sample from 560K to 345K in intervals of 5K in high-temperature regions and 2K at temperatures where the relaxation mode appeared strongly in signals. Before recording data, the temperature was allowed to stabilize for about 10 minutes to within ± 0.05K of the desired temperature.

5.3 ISTS Data

Fig. 5-1 shows typical ISTS data at q=0.336 μm^{-1} and T = 388.2K. The acoustic, thermal diffusion and structural relaxation modes are all present. Figure 5-1A exhibits damped acoustic oscillations at short times and the structural relaxation mode (slowly reaching a steady-state level in signal) on a longer time scale. Figure 5-1B displays thermal diffusion dynamics which are even slower. These two parts of the data were joined by matching the signal intensities in their overlapping temporal region. The connected data are displayed on a logarithmic time scale in Fig. 5-2, together with data at other temperatures at this excitation wavevector. It is seen that the ISTS signal reaches a steady-state level rapidly at 392.6K and much more slowly at 367.0K, which reflects the slowing down of the structural relaxation dynamics. At temperatures higher than 392.6K, structural relaxation occurs on a time scale comparable to or faster than half the acoustic oscillation period $\pi/\omega_A(q)$ at this scattering wavevector. Further characterization of the relaxation mode at this wavevector is not possible. Characterization of the relaxation mode at higher temperatures was achieved with larger scattering wavevectors, at which the acoustic frequency was higher. Figure 5-3 displays the data collected at two higher wavevectors. As shown in Figs. 5-2 and 5-3, the lower the temperature, the

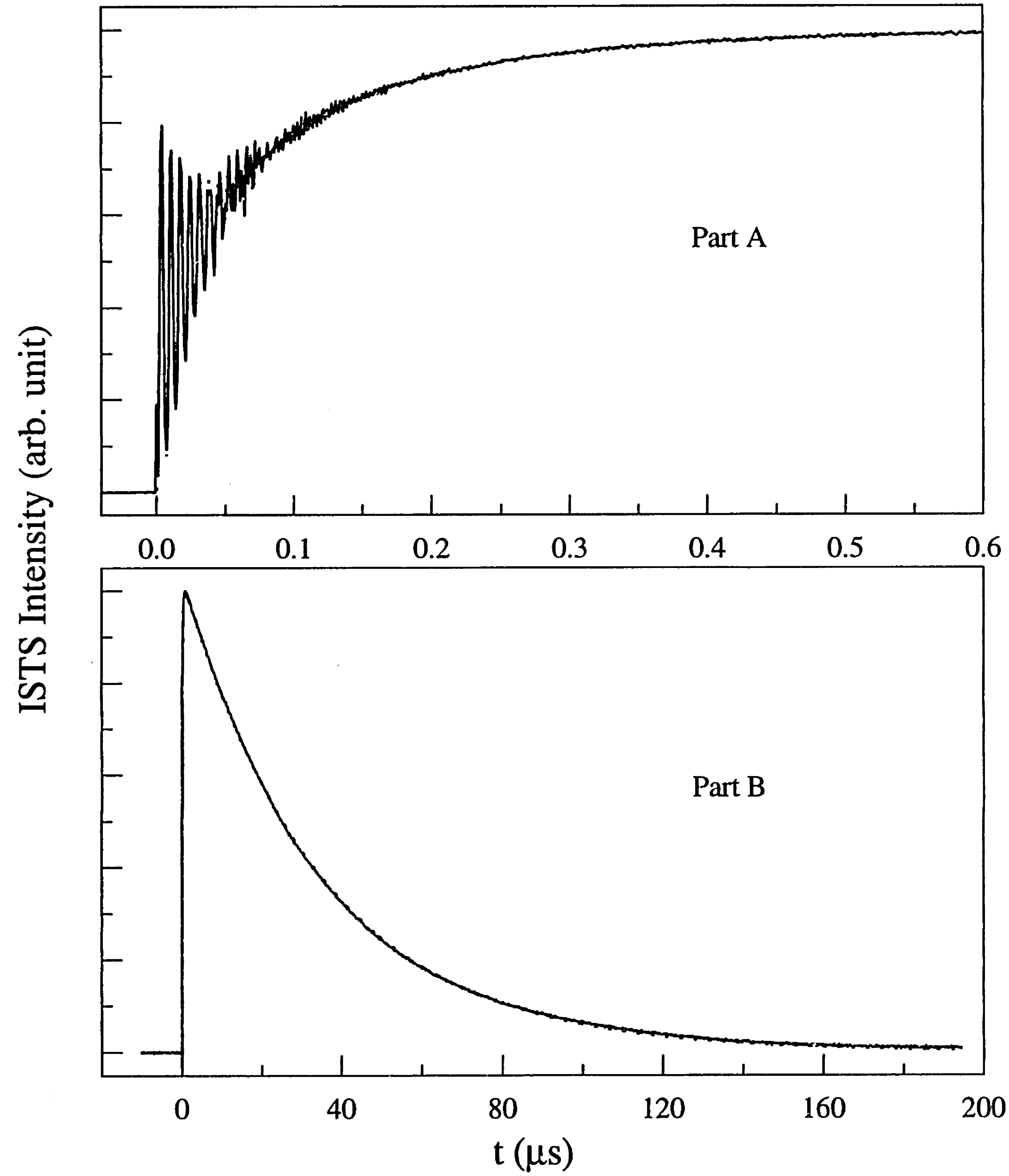

Figure 5-1: Typical ISTS data (solid curves) and fits (dotted curves) from CKN at 388.2K at a wavevector q=0.336 μm^{-1}, resulting from density responses to sudden heating by the two crossed ps laser pulses. (A) Damped acoustic oscillations at short time scales and the nonoscillatory, gradually rising signal due to structural relaxation on longer time scales. (B) Thermal diffusion dynamics at long times.

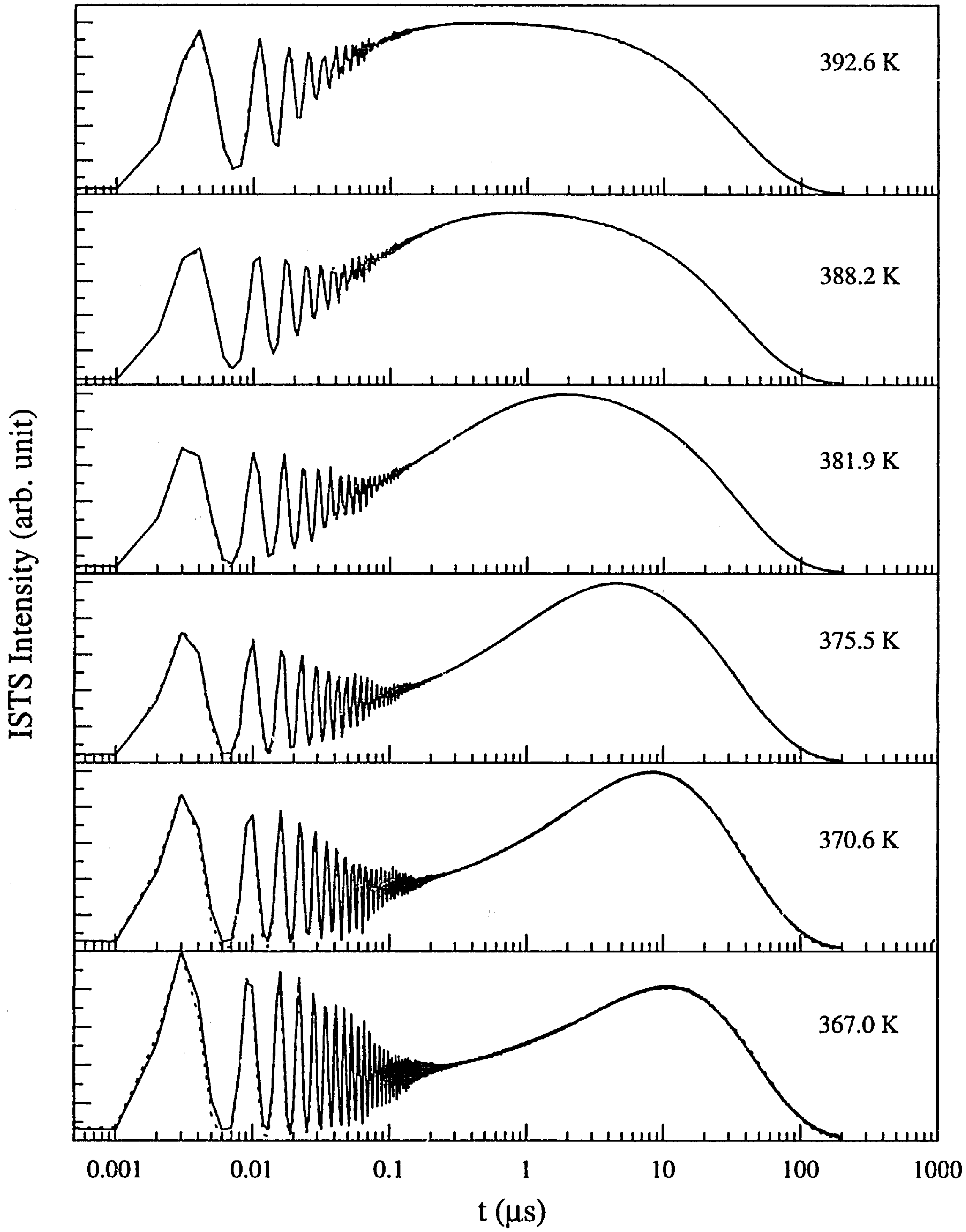

Figure 5-2: Data of Fig. 5-1 shown on logarithmic time scale including the acoustic, relaxation, and thermal diffusion modes, along with the data at several other temperatures collected at the same $q = 0.336\ \mu m^{-1}$. Upon cooling, the acoustic oscillations become faster and the thermal diffusion rates show a very weak temperature dependence. In addition, the signal reaches its steady-state level rapidly at high temperatures and more slowly at low temperatures, the latter revealing slow and nonexponential structural relaxation dynamics.

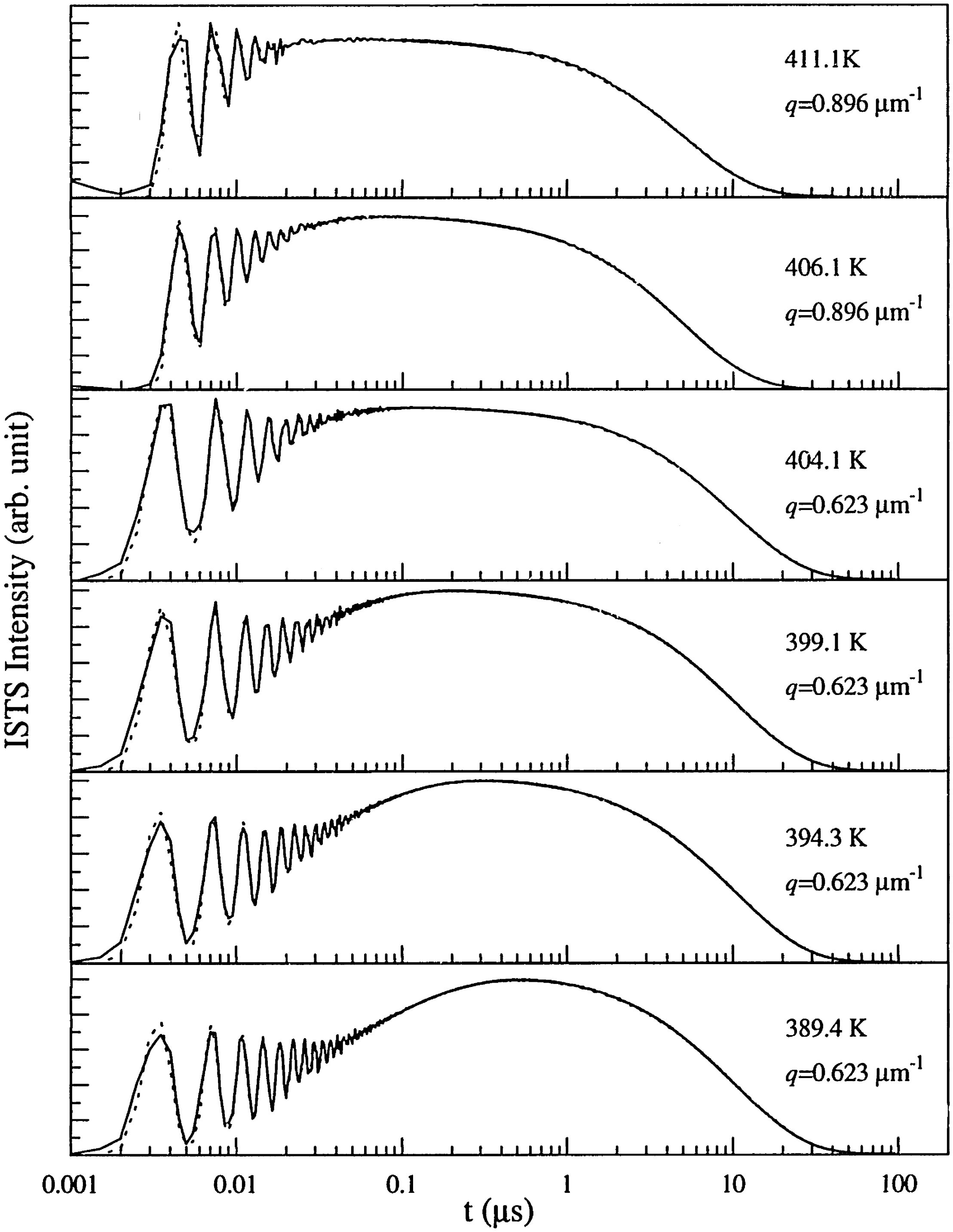

Figure 5-3: Logarithmic plots of ISTS data (solid curves) and fits (dashed curves) from CKN, collected at wavevectors of 0.623 and 0.896 μm^{-1}. These data permit characterization of structural relaxation at higher temperatures than the data collected at smaller q since the acoustic frequencies are higher. This extends the temperature range over which structural relaxation dynamics can be determined.

longer time scales at which the signal reaches a steady-state level, which reflects the slowing down of the structural realxation. Below 367.0K, the structural relaxation dynamics become comparable to or slower than the thermal diffusion rate Γ_H, which prevents further characterization of the relaxation mode at this wavevector. Lower wavevectors were used to extend characterization of the relaxation mode to lower temperatures. Above 411.1K, the relaxation mode cannot be characterized because the relaxation time is comparable to or shorter than half the acoustic oscillation period at the highest q reached in this experiment.

We now present detailed analyses of the α relaxation strength and dynamics, and compare the results with MCT predictions.

5.4 Data Analysis and Discussion

Equation 3.3 with ISTS response function $G_{\rho T}$ given by Eq. 3.49 yielded excellent fits to the raw data collected at all temperatures and scattering wavevectors, as illustrated by the dotted lines in Figs. 5-2 and 5-3. Fits to the data yielded the dynamical parameters describing the acoustic, thermal diffusion, and α relaxation modes as well as the relative amplitude A/B from which the relaxation strength or Debye-Waller factor $f_{q\to 0}$ can be derived. With good temporal separation of the acoustic, relaxation, and thermal diffusion modes, the fitting parameters were determined uniquely with reasonable accuracy. Uncertainties in each of the parameters were determined by fixing individual parameter values progressively farther from their best-fit values and refitting the data, letting the other parameters vary, until adequate fits could no longer be obtained. The uncertainties determined in this manner were supported by statistical analysis through use of the F statistic test [83, 84].

In no data were there any significant contributions to signal arising from impulsive stimulated Brillouin scattering, an alternative photoacoustic excitation method used in earlier experiments on pure CKN [48] but substantially weaker than ISTS in the doped CKN solution used for the present experiments.

5.4.1 The Debye-Waller Factor $f_{q\to 0}(T)$

The Debye-Waller factor $f_{q\to 0}$ was determined through Eq. 3.46 by using the fitting parameter A/B, which was obtained from those data in which the conditions $\omega_A(q;T) \gg \Gamma_R(T) \gg \Gamma_H(q;T)$ held. In Fig. 5-4, $f_{q\to 0}(T)$ values (symbols) obtained with different wavevectors are plotted. It is evident that $f_{q\to 0}(T)$ shows a weak cusp-like anomaly as predicted by MCT. The solid curve in Fig. 5-4 represents the best fit to Eq. 1.26 with the fitting parameters $f^c_{q\to 0} = 0.575 \pm 0.005$, $h_{q\to 0} = 0.36 \pm 0.02$, and $T_c = 378K \pm 2K$. In the inset of Fig. 5-4, we display the Debye-Waller factor obtained at a single wavevector of 0.235 μm^{-1}, and the fit to Eq. 1.26 which gave the same crossover temperature T_c within uncertainty. This T_c value is in good agreement with the results from depolarized light scattering [10, 82], neutron scattering [2], and Brillouin scattering [45]. Note that the Debye-Waller factor in Fig. 5-4 does not show a sharp cusp anomaly at T_c, presumably due to activated thermal hopping processes which are accounted for in the extended MCT We have, for simplicity, still used Eq. 1.26 to fit $f_{q\to 0}(T)$ and to identify the crossover temperature T_c.

5.4.2 α Relaxation Dynamics

The dynamical parameters Γ_R and β describing α relaxation were obtained by fitting data at various wavevectors in the temperature range 362.7-411.1K. The average relaxation times $<\tau_R>= (\tau_R/\beta)\Gamma(1/\beta)$ ($\Gamma(x)$ denoting the gamma function) were then calculated. The results are listed in Table 5.1. The temperature dependence of $<\tau_R>$ is shown in Fig. 5-5, and indicates no q-dependence in the wavevector range examined. Also plotted in Fig. 5-5 are $<\tau_R>$ values determined from DLS [10] and PCS [11, 12]. The data in this study span the gap between DLS results at high frequencies and PCS measurements on longer time scales, and show a smooth variation between them. Note that $<\tau_R>$ values from DLS have been properly scaled as discussed in Ref. [10]. The $<\tau_R>$ values from this study coincide with those from DLS and PCS in their overlapping regions, which suggests that the three

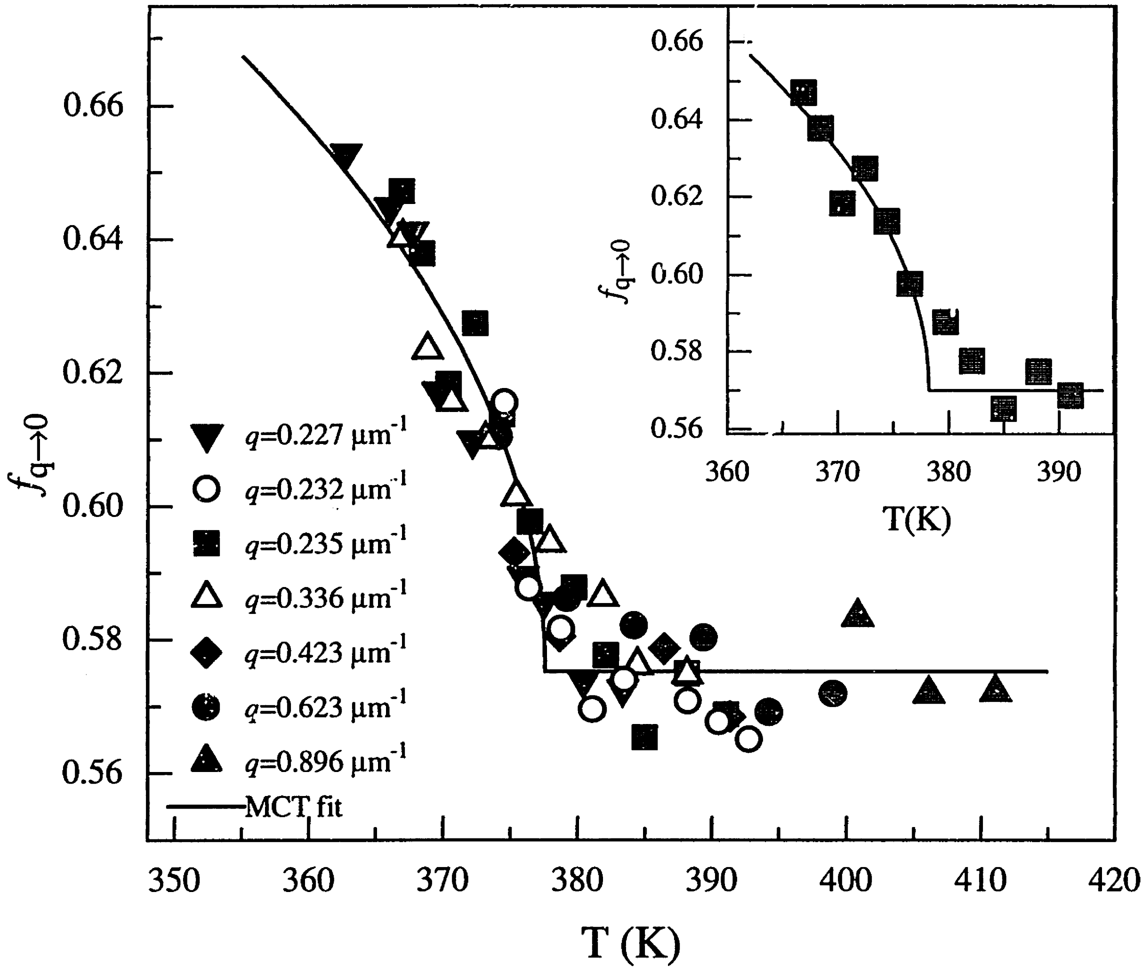

Figure 5-4: Temperature dependence of the Debye-Waller factor $f_{q\rightarrow0}$ (symbols) determined from ISTS data at several wavevectors via Eq. 3.46. The best fit (solid line) to Eq. 1.26 yields a crossover temperature $T_c = 378 \pm 2K$.

Table 5.1: Fitting parameters for the structural relaxation dynamics of CKN and the average relaxation time at various temperatures. The uncertainties in temperature are ± 0.1K; in Γ_R, ±8%; in β, ±0.03; and in $<\tau_R>$, ±10%.

T(K)	$\Gamma_R(\mu s^{-1})$	β	$<\tau_R>$ (μs)
411.1	456.	0.58	3.45×10^{-3}
406.1	231.	0.58	6.82×10^{-3}
404.1	151.	0.58	1.04×10^{-2}
399.1	79.5	0.58	1.98×10^{-2}
394.7	59.1	0.58	2.66×10^{-2}
392.6	43.0	0.58	3.67×10^{-2}
388.2	19.5	0.58	8.02×10^{-2}
384.5	9.84	0.58	1.61×10^{-1}
381.9	5.33	0.58	2.93×10^{-1}
379.8	2.58	0.59	6.04×10^{-1}
377.9	2.28	0.57	7.13×10^{-1}
375.5	1.28	0.58	1.28
373.2	6.96×10^{-1}	0.57	2.32
370.6	3.72×10^{-1}	0.56	4.46
367.0	9.81×10^{-2}	0.52	19.0
364.8	6.18×10^{-2}	0.52	30.2
362.7	1.25×10^{-2}	0.52	150.

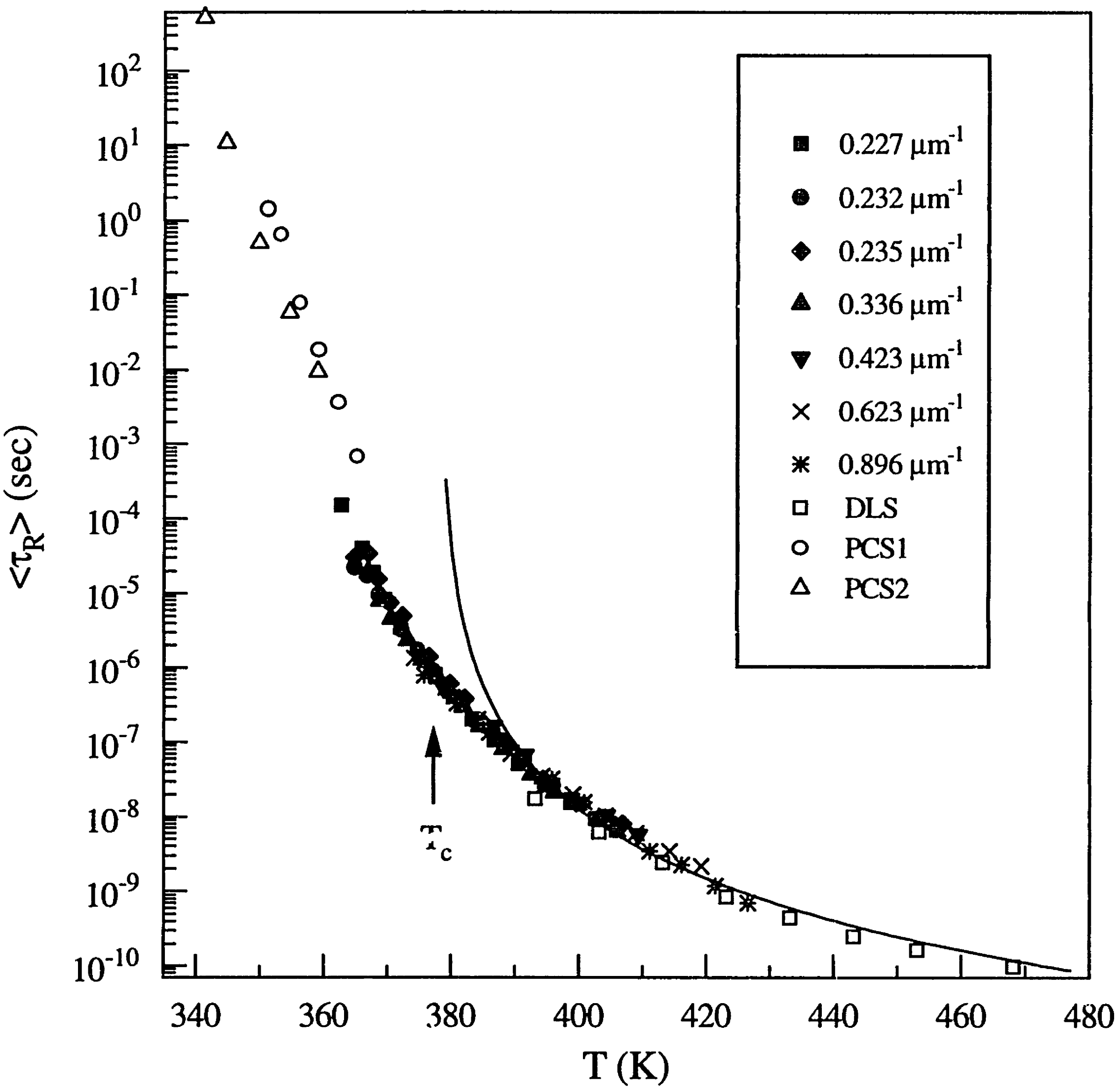

Figure 5-5: Temperature dependence of the average relaxation times $<\tau_R>$ from the present ISTS, previous DLS, PCS (from Ref. [11]), and PCS (from Ref. [12]) measurements. The solid line represents a fit to Eq. 1.28, in which T_c was given by the value determined from $f_{q\to 0}(T)$. The fitting parameters are $\gamma = 3.3 \pm 0.2$ and $<\tau_R^0> = (0.9 \pm 0.3)$ ps.

measurements probe similar dynamical processes.

According to the MCT scaling prediction, the α relaxation scale τ_R (or $<\tau_R>$) above T_c is given by the power-law (Eq. 1.28) since $\tau_R = \tau_\alpha c_\infty^2/c_0^2$ and the temperature dependences of τ_R and τ_α should be the same. A fit of $<\tau_R>$ (T) values above T_c to Eq. 1.28 is shown in Fig. 5-5 (solid curve) with T_c fixed at the value determined above. The data at high T are consistent with the MCT prediction, with values of the power-law exponent $\gamma = 3.3 \pm 0.2$ similar to those determined from the DLS data [82]. In the context of the extended MCT, activated hopping processes are assumed to be responsible for moderation of the power-law divergence at temperatures close to T_c. As discussed in Ref. [29], Eq. 1.28 is not valid below and close to T_c.

The stretching exponent values β are plotted in Fig. 5-6, together with values obtained from DLS [10], PCS [11, 12], and neutron scattering [2]. The values obtained from this study are approximately constant with $\beta = 0.58 \pm 0.03$ for $T > T_c$. The β values obtained from ISTS, neutron scattering, and DLS, show no temperature dependence within their uncertainties from just above 378K ($= T_c$) to 468.2K, yielding the value of $\beta \approx 0.58$ (dotted line in Fig. 5-6) in this temperature range . This finding provides support for the MCT prediction of constant α relaxation stretching above T_c.

As the temperature is reduced to below T_c, the β values deduced from this study decrease. In a narrow range of overlap at low temperatures, they agree well with results from PCS [12]. At still lower temperatures, two PCS studies [11, 12] indicated somewhat different, constant values for β in the 351-365K and 341-359K ranges. In any case, we may conclude from our results and those of PCS that the β values change significantly at temperatures near and below T_c. This is consistent with the physical picture of very different mechanisms for α relaxation above and below T_c. Experiments on a very different glass former, the organic molecular liquid salol presented in Chapter 4, showed qualitatively similar results.

Before closing this subsection, we briefly review a couple of previous light scattering results on CKN. One was from a frequency-domain Brillouin scattering study [85,

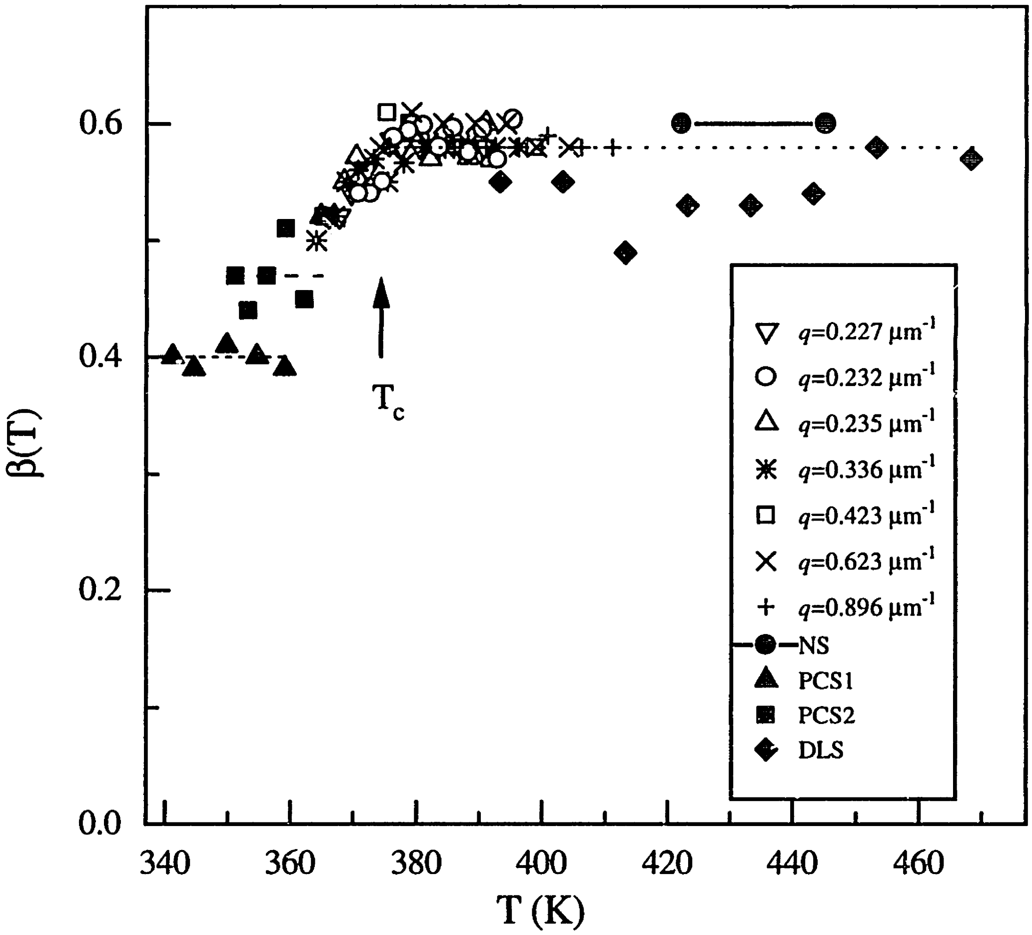

Figure 5-6: Temperature dependent relaxation stretching parameters β from the present ISTS study at several wavevectors, neutron scattering, DLS, and PCS (from Ref. [11]), and PCS (from Ref. [12]. The dotted line represents the constant β value of 0.58 above T_c determined from this study, neutron scattering and DLS.

86] and the other was from a time-domain impulsive stimulated Brillouin scattering study [48]. While the former performed measurements of the acoustic frequency and the acoustic attenuation rate as a function of temperature at two different wavevectors, the latter mapped out the acoustic modulus spectrum by making measurements at multiple wavevectors covering more than two decades of wavevector range. Both studies suggested single exponential relaxation dynamics at high temperatures and a stretched relaxation at low temperatures. The finding of single exponential structural relaxation at any T is contradictory to the combined results from our present ISTS study, DLS, and neutron scattering, which all show constant stretching from about 378K to 468.2K. Although our ISTS study does not concern the acoustic dynamics, several comments may be in order. As experimentally well established, the relaxation dynamics in viscous liquids span more than 2 orders of magnitude in time or frequency at a single temperature and more than 14 orders from the melting point T_m to the calorimetric glass transition T_g. Therefore, one has to examine the relaxation dynamics over a sufficiently broad range of time or frequency scales and sample temperatures to permit reliable description of material behavior or heuristic models. Brillouin scattering studies like the one performed on CKN [85] only cover about two decades of frequency range, which certainly does not permit characterization of the Mountain mode dynamics or determination of the two limiting velocities c_0 and c_∞ over a wide temperature range. In the ISBS study, acoustic velocities and attenuation rates on CKN were determined from 50 MHz to 4 GHz. This range, including the Brillouin spectra [85], permitted adequate elucidation of the relaxation spectrum at some temperatures, but at high temperatures, at which Debye relaxation dynamics were reported, the relaxation spectra were cut off at the 4 GHz frequency which was the highest that could be observed. However, it is particularly important to map out part of the high frequency wing of the relaxation spectrum. This is because relaxation spectra with different functional forms differ mostly in the high frequency region. They are almost identical in the low frequency wing. Therefore the acoustic data at high temperatures where only the low frequency wing of the relaxation peak was observed cannot be used to deduce single-exponential decay.

5.4.3 α Relaxation Scaling above T_c

To illustrate the α relaxation function $\phi(t;T)$ and its scaling directly, the acoustic and thermal diffusion contributions to ISTS signal can be subtracted from the square root of the data as indicated in Eq. 3.49. The results divided by $A + B$ give the relaxation function $\phi(t;T)$, which is shown in Fig. 5-7 from 411.1K to 367.0K. The dotted curves in Fig. 5-7 represent the stretched exponential fits. The resulting dynamical parameters Γ_R and β were found to be in good agreement in all cases with those from the original fits.

Time-temperature scaling of the α relaxation function at $T > T_c$ according to Eq. 1.27 is shown in Fig. 5-8. The rescaled results $F(t/\tau_R;T)$ versus t/τ_R are shown for the relaxation functions in Fig. 5-7 except those at the lowest two temperatures (well below T_c), with $\tau_R^{-1} = \Gamma_R$ values determined from the fits. All the experimental data from 375.5K to 411.1K fall on a stretched exponential master curve (solid curve) with $\beta = 0.58$. It is not possible to scale the data below 375.5K on the same master curve. This is consistent with the fact that the β values below 375.5K were found to be significantly smaller than 0.58. Note that we have included the data at 375.5K, since this temperature is just below T_c (378.1K) and the β value is still very close to 0.58.

5.5 Conclusions

Impulsive stimulated thermal scattering has been used to explore the α relaxation dynamics as well as the relaxation strength, or the Debye-Waller factor $f_q(T)$, of the glass former CKN. A cusp-like anomaly in the temperature dependence of $f_{q\to 0}(T)$, rounded somewhat near the crossover temperature $T_c = 378\text{K}$, was observed, consistent with the prediction of mode-coupling theory. The value of T_c is in good agreement with results from neutron scattering and DLS studies, which indicates the q-independence and technique-independence of this result.

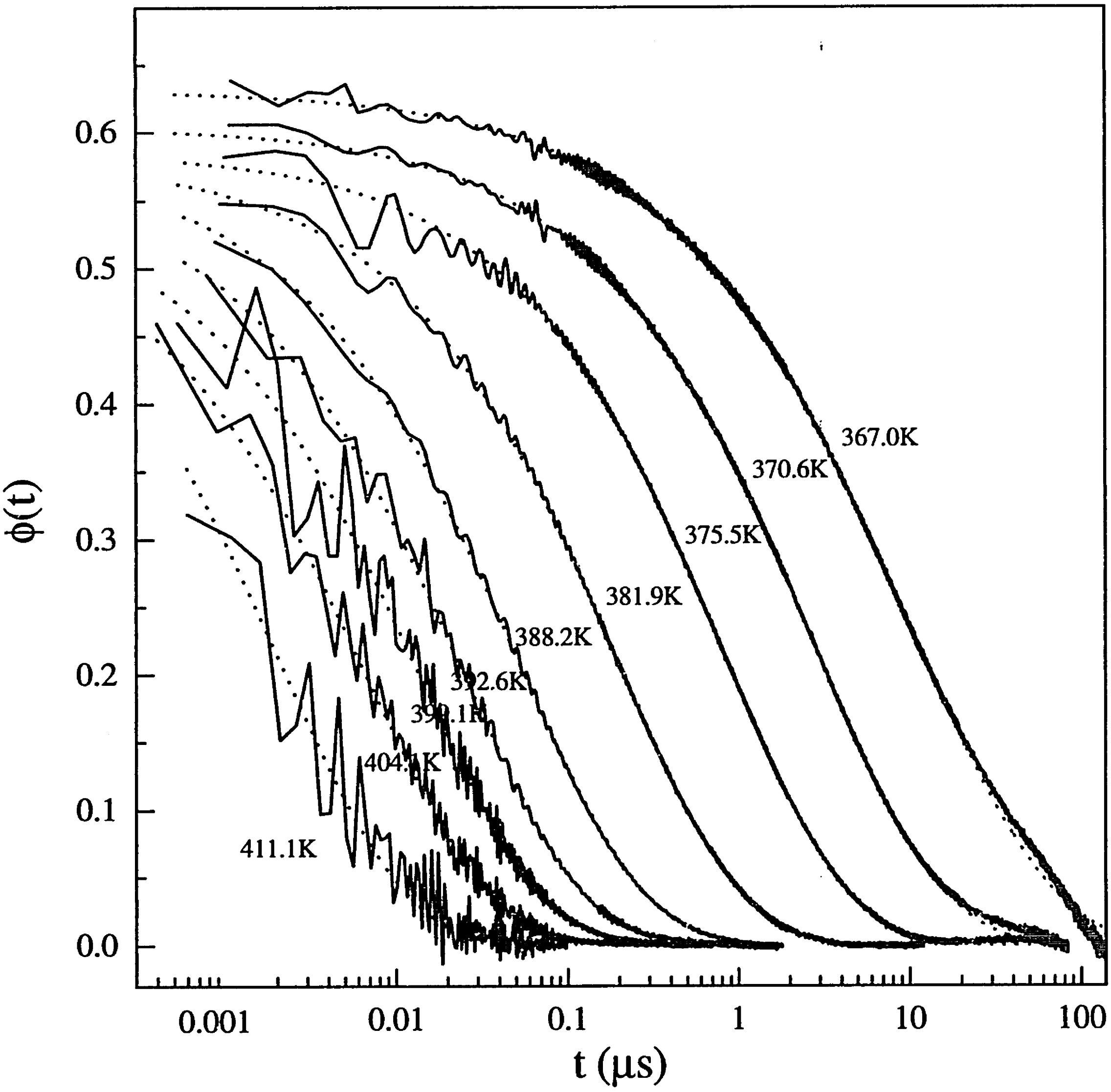

Figure 5-7: Structural relaxation functions $\phi(t;T)$ of CKN from 367.0K to 411.1K, extracted from ISTS data shown in Figs. 5-2 and 5-3 (solid curves) and their stretched exponential fits (dotted curves).

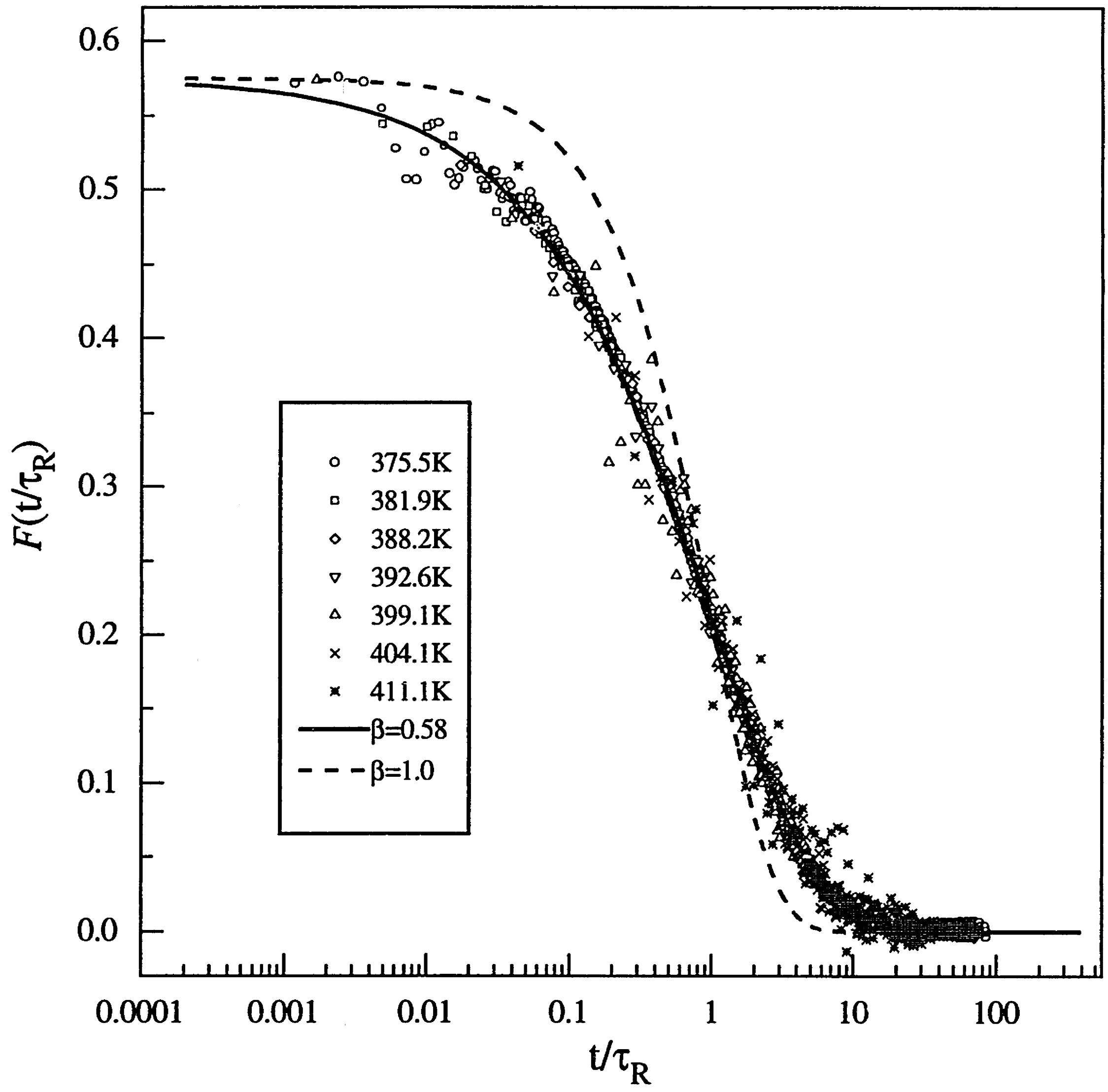

Figure 5-8: Rescaled plot of $\phi(t/\tau_R;T)$ (symbols) vs t/τ_R, with $\tau_R = \Gamma_R^{-1}$ values determined from the fits shown (except for those from the two lowest temperatures) in Fig. 5-7. The solid line is a stretched exponential function with β=0.58 and the dashed line is the Debye relaxation function shown for comparison.

The α relaxation dynamics in the 411.1-362.7K temperature range, within which they change from several-nanosecond to many-microsecond time scales, are described well by the stretched exponential function. In the wavevector range of 0.227-0.896 μm^{-1} used in this study, the relaxation dynamics are independent of wavevector. Above T_c, the stretching parameter shows no temperature dependence with $\beta \approx 0.58$, in good agreement with the scaling law prediction of MCT. Below T_c, β decreases with decreasing temperature. It may continue to decrease for temperatures below 262.7K, the lowest temperature at which the α relaxation dynamics could be determined in our experiments. The average relaxation times well above T_c are consistent with the power-law dependence predicted by MCT.

The experimental findings in this study are consistent with the scenario for the liquid-glass transition which emerges from mode-coupling theory. There exists a crossover temperature T_c at which the temperature dependence of the α relaxation strength or Debye-Waller factor shows a square-root singularity. Above T_c, nonlinear interactions between the density fluctuations, but not thermally activated processes, determine the α relaxation dynamics and their temperature variation (i.e. scaling laws and the power law divergence of the relaxation time scales). Without thermally activated hopping, a sharp transition from an ergodic liquid to a non-ergodic ideal glass state would occur at T_c. With thermally activated processes, α relaxation is restored at $T < T_c$ while the divergence of the relaxation time scale and the singularity in the Debye-Waller factor are moderated. Instead of being an ideal transition temperature, T_c marks a crossover of the mechanism for α relaxation .

In summary, the predictions of mode-coupling theory tested by ISTS in this work are well supported by the results. ISTS is well suited for determination of the Debye-Waller factor and the crossover temperature, as well as the structural relaxation dynamics which are characterized by direct observation as in this Chapter and Chapter 4, or through observations of the acoustic mode which will be described in Chapter 6. ISTS provides a wide dynamic range, extending from nanoseconds (or less if a pulsed rather than CW probe is used) to many milliseconds, some of which is difficult to access with other light-scattering methods. In addition, the wide range of scattering angles that can be used permits separation of signal contributions that often overlap when the range is more restricted. A current experimental challenge is extension of the method to shorter time scales and to both higher and lower acoustic frequencies, with the objective of elucidation of relaxation dynamics (including the faster β relaxation) over wider time and temperature ranges.

Chapter 6

Structural Relaxation in Salol from Acoustic Dynamics

6.1 Introduction

As reviewed in Chapter 1, in a mesoscopic frequency window, the so-called β-relaxation regime, there is predicted to be a common β-correlator $G(t)$ for correlation functions $\phi_{XY}(t)$ of any variables X and Y as long as they couple to the density fluctuations. The time and temperature dependences of $\phi_{XY}(t)$ are given by the β-correlator $G(t)$ in leading order. It has been shown [82, 87] that in the glass former $Ca_{0.4}K_{0.6}(NO_3)_{1.4}$, $G(t)$ derived from DLS spectra provides a consistent description of neutron scattering data.

Structural relaxation in glass formers induces a frequency dependence of the elastic moduli $M(\omega)$. Thus one can obtain structural relaxation information by studying the frequency-dependent behavior of $M(\omega)$. Since the elastic modulus is the autocorrelation of a stress tensor component which is coupled to the density fluctuations through the Navier-Stokes Eq. 3.5, the frequency dependence of the acoustic modulus $M''(\omega)$ in the β-relaxation regime should follow the corresponding β-susceptibility spectrum of $G(t)$: $\chi''(\omega) = \omega G''(\omega) = \omega \int_0^\infty \cos(\omega t) G(t) dt$, which is common for any susceptibility spectrum $\chi''(\omega)$ like that from DLS or neutron scattering. So far to our knowledge there has been no such comparison reported.

This is partly because mechanical measurements in the β-relaxation window (from MHz to GHz above) are difficult. Over the last several years it has been shown that an optical technique, impulsive stimulated light scattering including ISTS and ISBS, is applicable to the study of the elastic properties in liquids and amorphous materials [33, 48-53]. From ISS measurements of acoustic frequencies and damping rates, the complex elastic modulus spectra were constructed in the 10 MHz -10 GHz range to examine relaxation dynamics in this range.

As described in Chapter 3, ISTS provides not only acoustic dynamics, but also the structural relaxation function directly. Under favorable conditions it also gives the α relaxation strength, or Debye-Waller factor, whose temperature dependence is predicted to exhibit a square-root cusp at a crossover temperature T_c within the MCT. In Chapters 4 and 5, we have presented ISTS experiments on the glass formers salol and CKN and analysis of the structural relaxation mode concerning its dynamics and strength. In this Chapter, we shall present the second part of our ISS studies on glass former salol: characterization of the acoustic mode dynamics and comparison of the acoustic modulus spectra with the MCT predictions.

Salol is a fragile liquid in Angell's strong-fragile classification scheme [88]. It has been the object of numerous studies including ISTS described in Chapter 4, dielectric spectroscopy [5], DLS [9, 82], neutron scattering [75], and photon correlation spectroscopy [68]. In particular, the susceptibility spectra of salol from DLS [9, 82] were compared with MCT. The β-susceptibility spectra $\chi''(\omega)$ were obtained in their experimental spectral window of sub-GHz to 4 THz and extrapolated to even lower frequencies. According to MCT, the derived β-susceptibility $\chi''(\omega)$ should show the same frequency dependence as any other susceptibility spectra, including the acoustic modulus $M''(\omega)$ or compliance $J''(\omega)$. A comparison $M''(\omega)$ or $J''(\omega)$ to the results obtained from DLS measurements is therefore possible.

This Chapter is organized as follows. In Sec. 6.2, the experimental methods are discussed. Section 6.3 describes the qualitative features of ISTS data. The acoustic modulus and compliance spectra are presented in Sec. 6.4. In Sec. 6.5 the analysis and comparison to theoretical predications and DLS spectra are shown. Finally the results are discussed in Sec. 6.6.

6.2 Experimental Methods

We used the excitation system with short IR pulses as pump sources as described in Chapter 2 and employed two alternate probe systems to detect the material excitations. For excitation angles θ_E smaller than 13°, at which the acoustic frequencies are within the bandwidth of the fast photodiode and transient digitizer, the quasi-CW probe beam was used. For θ_E above 13°, the acoustic frequencies are high so that the pulse probe system was used to collect the acoustic data. Other details of the experimental setup and sample preparation have been described in Chapters 2 and 4.

To map out the frequency dependence of the acoustic modulus $M(\omega_A)$ over a wide frequency range, data were collected with 20 excitation angles θ_E from 0.5° to 45°. The angles and the corresponding wavelengths are listed in Table 6.1. The wavelengths corresponding to the angles above 10° were determined through Eq. 2.1 with the angle θ_E measured mechanically using a calibrated rotation stage. For angles smaller than 10°, the wavelengths are determined in the way described in Chapter 4.

Since salol weakly absorbs the excitation light due to O-H vibrational overtone absorption at 1.064 μm, ISTS is the dominating excitation mechanism, especially at small q. Therefore the signal is primarily contributed by $G_{\rho T}(q,t)$ given by Eq. 3.49. Only at large wavevectors must the $G_{\rho\rho}(q,t)$ (Eq. 3.48) contribution to signal be included.

6.3 Qualitative Features of ISS Acoustic Data

Figure 6-1 shows typical ISTS data at various temperatures with an excitation wavevector magnitude $q = 0.7433\ \mu m^{-1}$. On the left-hand side are displayed damped acoustic oscillations at short times and on the right-hand side are exhibited

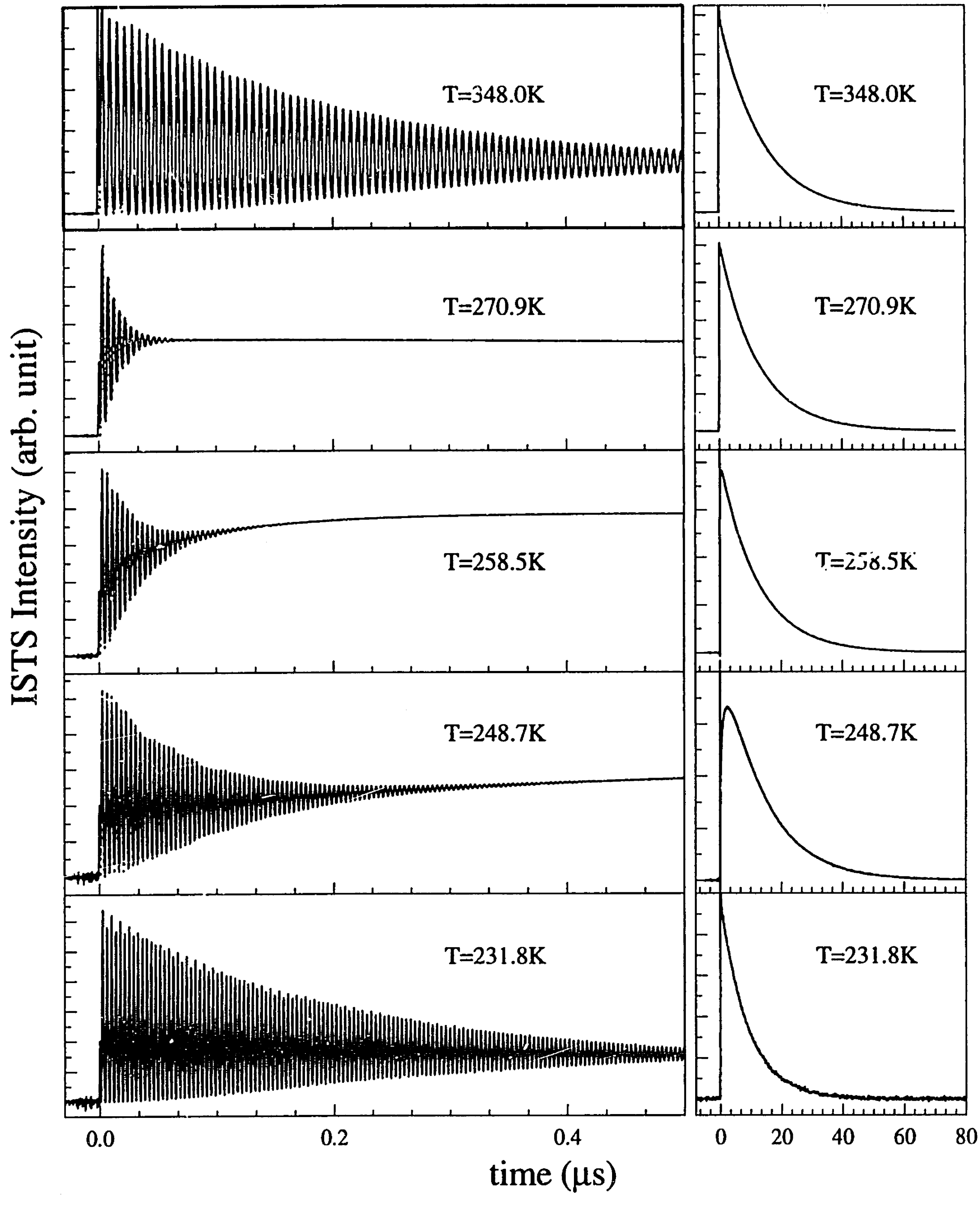

Figure 6-1: ISTS data (solid curves) and fits (dotted curves) to Eq. 3.3 with $G_{\rho T}(q, t)$ given by Eq. 3.49 of salol at wavevector $q = 0.7433$ μm^{-1} at several temperatures recorded with the quasi-CW probe system. The short time acoustic oscillations are shown in the left-hand side and the long time thermal diffusion dynamics are displayed in the right-hand side. In the intermediate temperature range, ISTS signal slowly reached the steady-state level and even slower at lower T, which reveals slow and nonexponential structural relaxation dynamics.

Table 6.1: Summary of excitation angles θ_E and their corresponding grating wavelengths used in ISTS experiments on salol.

Angle θ_E (degrees)	Wavelength (μm)	Angle θ_E (degrees)	Wavelength (μm)
0.50	123.3	3.85	15.81
0.87	70.19	4.52	13.58
1.23	46.47	5.12	11.74
1.47	41.20	7.22	8.453
2.10	29.08	8.65	7.061
2.13	28.02	10.30	5.922
2.62	23.21	12.25	4.995
3.05	20.13	19.50	3.149
3.45	17.63	37.90	1.640
3.73	16.44	44.93	1.393

longer-time dynamics including the structural relaxation mode (slowly reaching a steady-state level in signal) and the thermal diffusion mode. Note that the acoustic data are shown only up to 0.5 μs for clarity. The features of all three modes change as the sample temperature is reduced. The acoustic frequency ω_A increases with decreasing temperature and the acoustic damping rate Γ_A reaches a maximum at about 270.9 K. The relaxation mode, which manifests itself as a gradual rise in signal, appears only in the intermediate temperature range and becomes slower as T is decreased. The thermal decay rate monotonically increases with lowering temperature and shows a rapid increase around 241K at this q.

These changes occur because structural relaxation dynamics dramatically slow down upon cooling. At high T, relaxation occurs on a time scale faster than half the acoustic oscillation period $\pi/\omega_A(q)$, so local liquid structure adiabatically follows the acoustic oscillations. Following sudden, spatially periodic heating, thermal expansion at the grating peaks leads to a density modulation which overshoots and oscillates about the steady-state level. After the acoustic oscillations are fully damped, the steady-state density modulation decays due to thermal diffusion. The low-ω-limit acoustic velocity c_0 and thermal diffusivity of the liquid are measured.

As T is decreased, structural relaxation slows down and the structural relaxation spectrum passes through the acoustic frequency. The overlap between the structural relaxation spectrum and acoustic frequency induces dispersion in the acoustic frequency and attenuation rate. As the sample is cooled further, the structural relaxation spectrum moves away from acoustic frequency toward lower ones. On the time scale of the acoustic oscillations no significant structural relaxation can occur and the sample is therefore stiffer which results in a higher acoustic velocity, i.e. higher frequency in ISS data. Meanwhile the acoustic damping rate becomes smaller. In addition, the sample can no longer reach its steady-state density response to the oscillating acoustic stress. Instead, the density modulation slowly rises to its steady-state value and finally decays through thermal diffusion. This permits direct observation of the slow components of structural relaxation, called the relaxation mode in Chapters 3-5.

At even lower T, the structural relaxation spectrum overlaps the thermal decay rate, which results in dispersion of the thermal diffusion mode. For the lowest temperatures, close to T_g, the relaxation spectrum shifts to frequencies below even the thermal diffusion rate. Structural relaxation is then frozen on the experimental time scale, so the relaxation mode does not appear in ISTS data. The sample behaves like a solid. The high-ω-limit acoustic velocity c_∞ and thermal diffusivity of the solid-like sample or glass are obtained.

For all wavevectors, data exhibit the same T-dependent trends, but at different wavevectors the acoustic dispersion and attenuation maxima occur at different temperatures. The larger the wavevector, the higher the temperature for the greatest acoustic dispersion and damping rate maxima. The same is true for the rapid change of thermal diffusion rate. Since $\omega_A \propto q$ and $\Gamma_H \propto q^2$, the large q means high acoustic frequency ω_A and fast thermal diffusion rate Γ_H. As sample temperature decreases, the structural relaxation spectrum which shifts to lower frequencies therefore overlaps with the higher ω_A or Γ_A first, then the lower one Γ_H.

6.4 Acoustic Dynamics

By employing the Levenberg-Marquardt nonlinear least-squares algorithm, we have fitted the data to Eq. 3.1 with $G(q,t) = G_{\rho T}(q,t)$ given by Eq. 3.49 for $\theta_E < 15°$, and the other data are fitted with $G(q,t) = G_{\rho T}(q,t) + G_{\rho\rho}(q,t)$ where $G_{\rho\rho}(q,t)$ is given by Eq. 3.48. From the fitting parameters, the acoustic dynamics, thermal diffusion dynamics, and relaxation dynamics and strength in the intermediate T range were obtained. In Chapter 4, we have presented the characterization of the relaxation mode dynamics and strength and the comparison of the results to MCT predictions. In addition, the thermal diffusion dynamics have been presented. Here we describe detailed analysis of the acoustic mode dynamics and comparison of the longitudinal acoustic modulus spectra with MCT predictions and depolarized light scattering spectra.

6.4.1 Acoustic Parameters

In Fig. 6-2, the acoustic frequency ω_A and damping rate Γ_A are shown as functions of temperature for ten of the twenty wavevectors used, which exhibit the features discussed above. All the damping rate curves display a very asymmetric peak, which is typical of relaxation-coupled behavior. The peak temperature moves to higher T for larger q. The variation of the acoustic frequency, or acoustic velocity shown in Fig. 6-3 is closely related to the acoustic damping data. No frequency dispersion appears at low and high temperatures, and in the relaxation region at intermediate T a well marked change occurs from liquid-like to solid-like values. The liquid-like velocity from 275K to 400K follows a linear T dependence given by $c_0(T) = 2419m/s - 3.15m/(s \cdot K) \times TK$, which is represented by a solid line in Fig. 6-3. In Chapter 4, T-dependent values of the Debye-Waller factor f_q in the low-q limit have been determined from the amplitude of the relaxation mode contribution to signal. These values show a square-root cusp described by Eq. 1.26. With c_0 and $f_{q\to 0}$, we can derive the solid-like value c_∞ through Eq. 3.46. The open triangles in Fig. 6-3 represent the values of c_∞ from 263K to 290K determined in

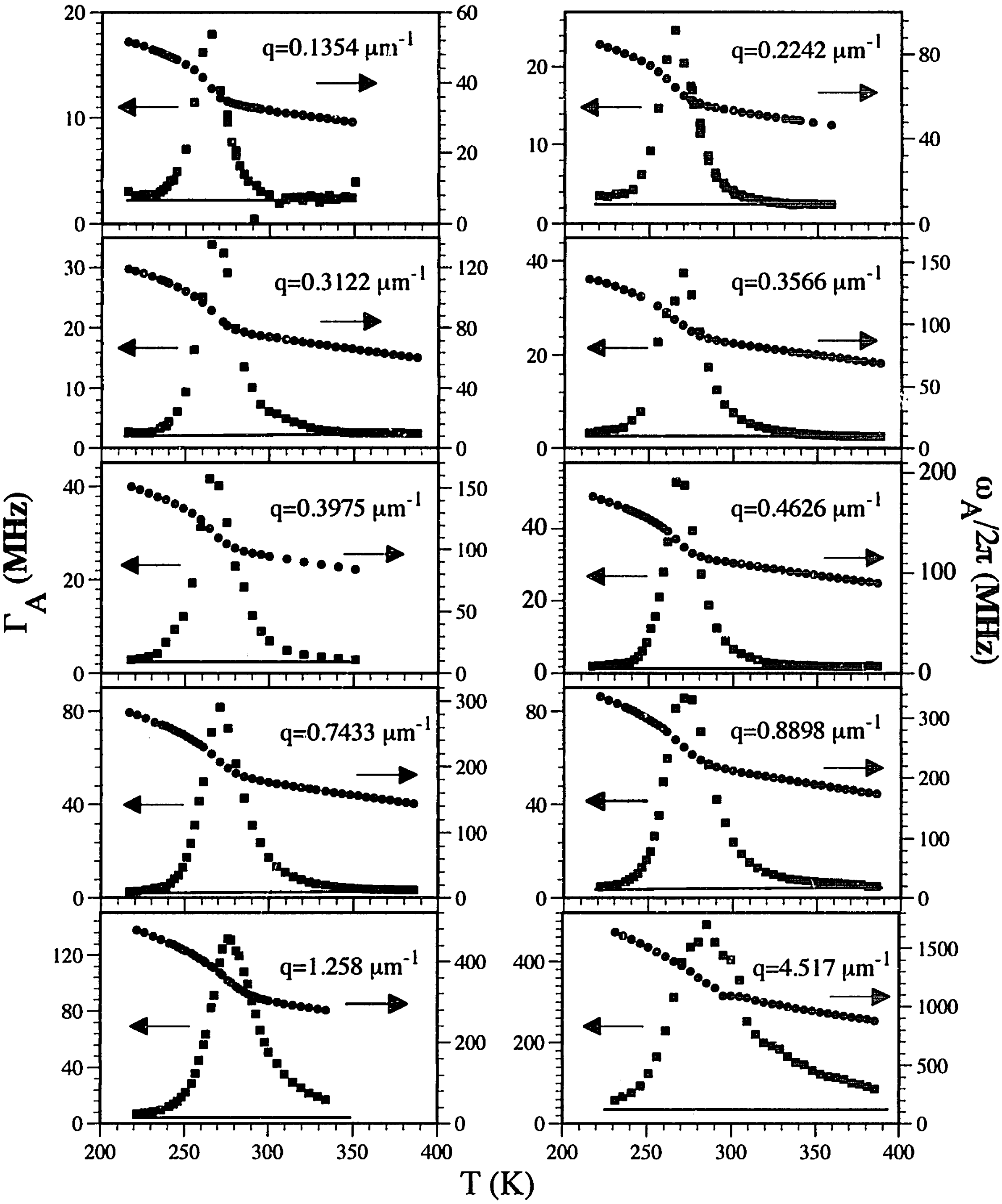

Figure 6-2: Temperature dependences of the longitudinal acoustic frequencies and damping rates of salol measured at different wavevectors. In all cases, the acoustic damping rate shows a maximum and the maximum position shifts to higher temperature for larger q. The variation of the acoustic frequency reflects the damping data. At the maximum of the damping rate, the acoustic frequency shows greatest dispersion.

this way. Note that the c_0 values (open Diamond in Fig. 6-3) used for calculating c_∞ of two lowest T were deduced through linear extrapolation. Later we will use the two limiting velocities of c_0 and c_∞ determined as described here to analyze the acoustic modulus spectra in terms of the KWW relaxation function.

As displayed in Fig. 6-2, the acoustic frequency ω_A and damping rate Γ_A were measured at fixed q. However, in the analysis that follows we need to examine the acoustic velocity and damping rate as functions of acoustic frequency at constant temperatures. To facilitate the generation of such data, we carried out spline interpolation for the T-dependences of the acoustic frequency and attenuation rate at each wavevector q. The parameters for a set of temperatures common to all q were thus obtained.

Before preceding, we need one more data preparation. As discussed in Chapter 3, the measured acoustic damping rate Γ_A originates from two different processes: structural relaxation contribution Γ_R and background contributions Γ_A^B. Obviously it is Γ_R which is that we are interested in. Therefore we need to separate Γ_R from Γ_A. Since at high or low T, the structural relaxation spectrum is either in a much higher or much lower frequency range compared to the acoustic frequency, the structural relaxation contribution to the acoustic damping rate is negligibly small and the measured acoustic damping rate gives the background contribution. We therefore made an assumption that the background contribution Γ_A^B is constant or weakly and linearly dependent on T, based on the damping rates at high and low T at each q (solid lines in Fig. 6-2). Then the difference between Γ_A and Γ_A^B gives the acoustic damping rate Γ_R due to structural relaxation.

In what follows we will focus our attention not on the acoustic velocities and attenuation rates themselves but on the reduced complex acoustic modulus $M(\omega_A)/\rho_0$, or reduced complex acoustic compliance $J(\omega_A)\rho_0 = (M(\omega_A)/\rho_0)^{-1}$ [62], as functions of acoustic frequency ω_A at fixed temperatures.

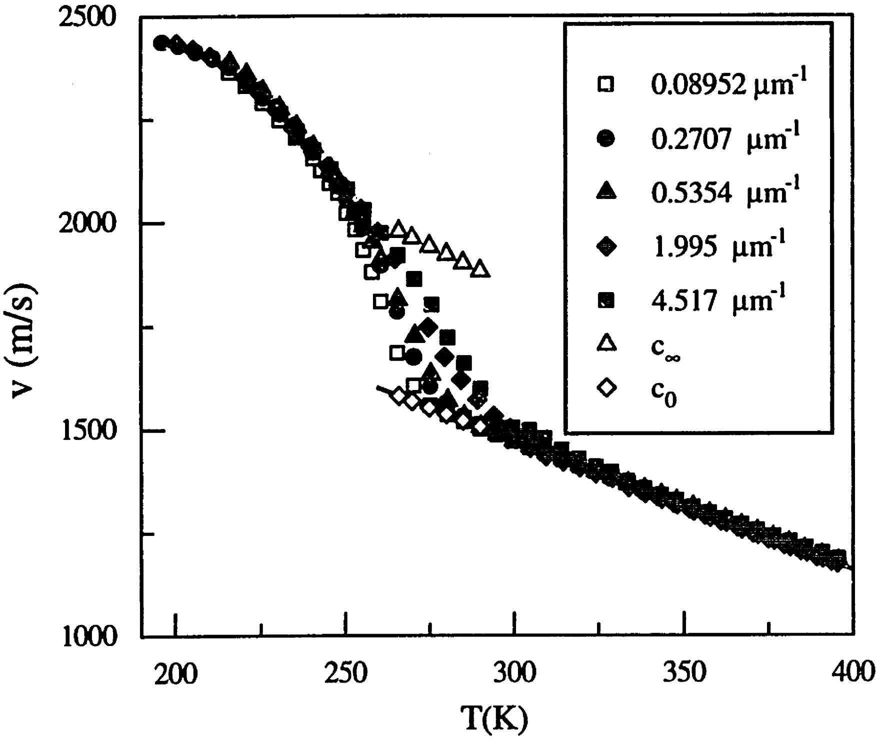

Figure 6-3: Speed of sound versus temperature in salol at several wavevectors. The high temperature data give the limiting velocity c_0 which follow linear T-dependence (solid line). The values of c_0 at the two lowest T are linear extrapolations. The infinite velocities c_∞ at intermediate T are the results from Eq. 3.46 based on c_0 and the Debye-Waller factor determined in Chapter 4.

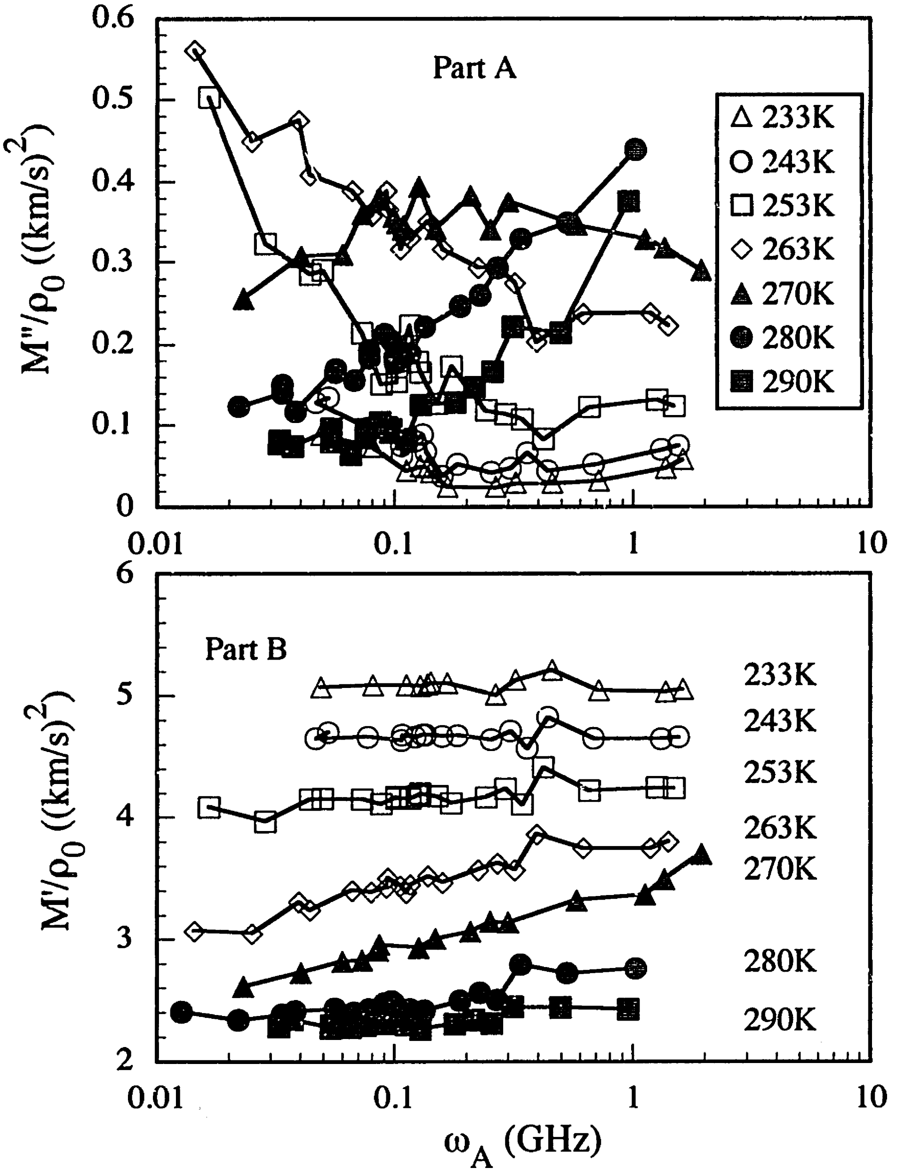

Figure 6-4: Complex longitudinal acoustic modulus of salol at several temperatures. (Part A) Imaginary part $M''(\omega_A)/\rho_0$ vs ω_A. (Part B) Real part $M'(\omega_A)/\rho_0$ vs ω_A. While a peak is observed at 270K in $M''(\omega_A)/\rho_0$, a minimum is visible at low T. However, the increase of $M''(\omega_A)/\rho_0$ as increasing ω_A cannot be attributed entirely to the β relaxation since $M''(\omega_A)/\rho_0$ contains the contribution from the viscosities and thermal diffusion, which alone could result in a minimum as shown in Fig. 3-1.

6.4.2 Total Acoustic Modulus Spectra

With the help of Eqs. 3.38 and 3.39, the reduced complex acoustic modulus $M(\omega_A)/\rho_0$ was calculated from the acoustic parameters for a set of temperatures common to all q. The results were tabulated as a function of acoustic frequency ω_A. Fig. 6-4 shows the real and imaginary parts of $M(\omega_A)/\rho_0$ at various temperatures. While the low-frequency side of the relaxation spectrum is observed at high T and the high-ω side is seen at low T, a peak is visible in the imaginary part $M''(\omega_A)/\rho_0$ (Part A of Fig. 6-4) at intermediate T in the range of acoustic frequencies probed. A minimum in $M''(\omega_A)/\rho_0$ versus ω_A is also observed at low T. But as discussed in Chapter 3, this minimum is not entirely due to the crossover of the α and β relaxation processes. There is a contribution from a linear-ω-dependent term, since $M''(\omega_A)/\rho_0$ displayed here is the total imaginary part of acoustic modulus.

6.4.3 Structural Relaxational Part of Acoustic Modulus

The structural relaxational part of the reduced acoustic modulus $M_R(\omega_A)/\rho_0$ can be easily obtained from ω_A and Γ_R through Eqs. 3.44 and 3.45. The real and imaginary parts of $M_R(\omega_A)/\rho_0$ at various T are plotted as a function of the acoustic frequency ω_A in Figs. 6-5 and 6-6. Again, as in the total reduced acoustic modulus spectra M''/ρ_0, we observe the low frequency wing of the relaxation spectra at high T, a relaxation peak at about 270K, and the high frequency side at low T. However, there is a major difference between the spectra M''/ρ_0 and M_R''/ρ_0 at low T. That is, the minimum in the M''/ρ_0 spectrum either disappears in our experimental frequency window or shifts to higher frequency in the M_R''/ρ_0 spectrum. Later we will come back to discuss the positions of the minima.

One can also analyze the acoustic dynamics through the complex acoustic compliance. Since $J\rho_0 = (M/\rho_0)^{-1}$, we have a simple relation between them: $J_R' \approx M_R'/|M_R|^2$ and $J_R'' \approx M_R''/|M_R|^2$. From these relations the compliance spectra were generated. As will be shown below, the spectra $J_R'\rho_0$ and $J_R''\rho_0$ around the α relaxation peak are much different from M_R'/ρ and M_R''/ρ, respectively. However, away

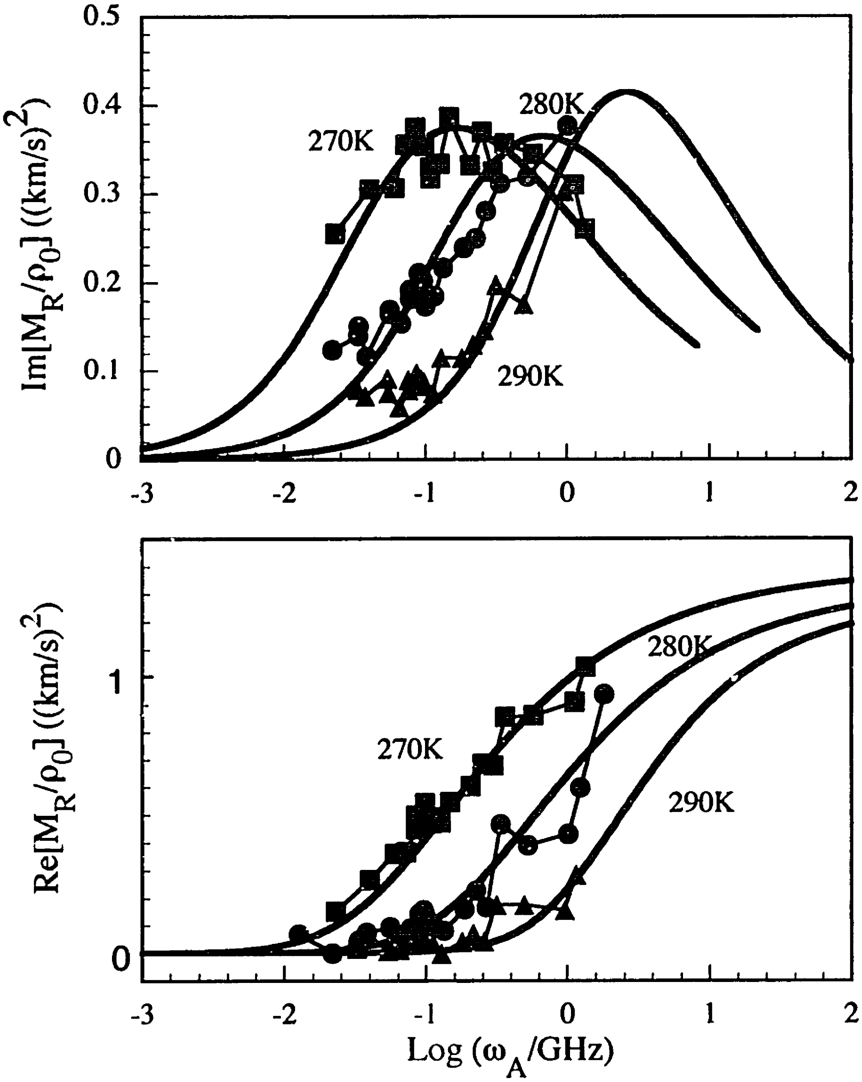

Figure 6-5: The structural relaxational part of the reduced longitudinal acoustic modulus above 270K. The imaginary part is shown in the top and the real part in the bottom. The solid lines are fits of the data to Eq. 6.1 with the KWW relaxation function. Note that the two limiting velocities c_0 and c_∞ are fixed at the values given in Fig. 6-3. Therefore only two parameters are left, the stretching parameter β and the characteristic relaxation time τ_L. Within the experimental uncertainty, β is found to be constant from 265K to 290K.

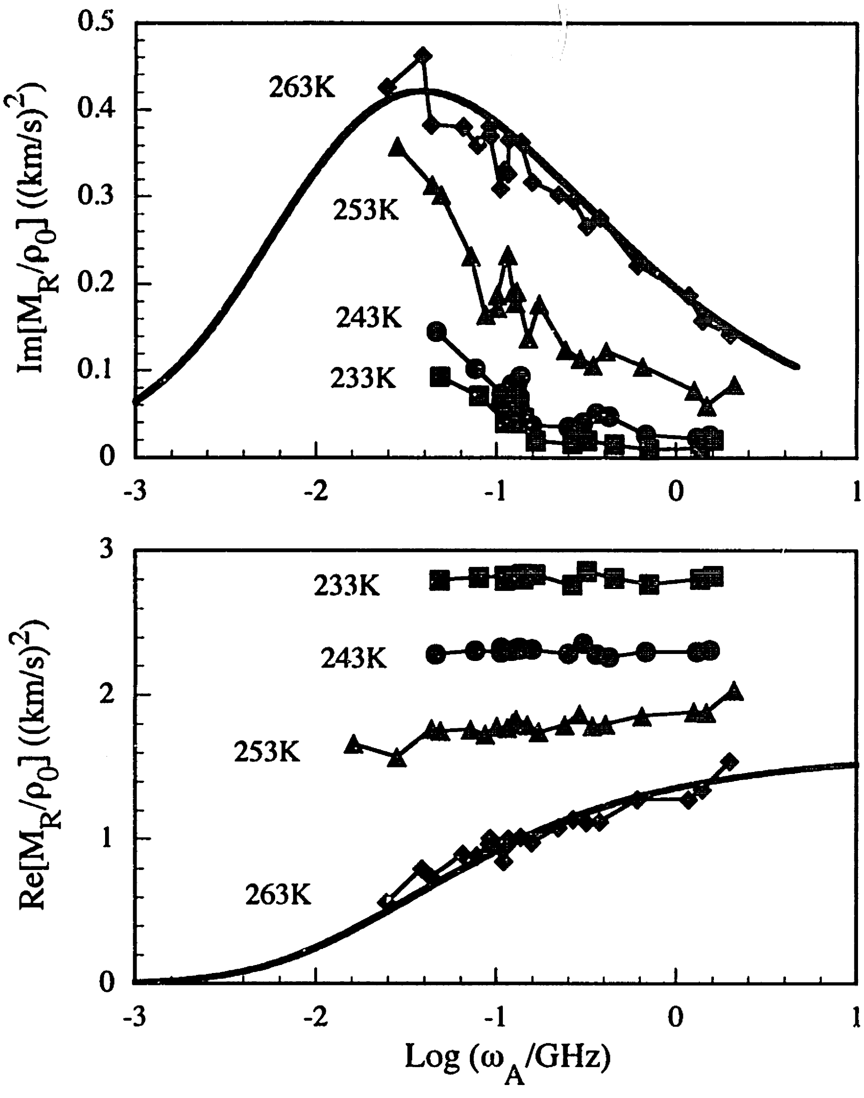

Figure 6-6: The frequency dependence of the structural relaxational part of the reduced longitudinal acoustic modulus below 263K. As shown in the bottom, the real part M_R'/ρ is nearly frequency independent in the acoustic frequency window probed, except at 263K. We therefore fit the data at 263K to Eq. 6.1 with an α-relaxation-only KWW function (solid lines), although β relaxation might already have effects on the measured spectrum.

from the α relaxation peak in the high frequency range both M''_R/ρ_0 and $J''_R\rho_0$ follow the common frequency dependence $\chi''(\omega)$ as predicted by MCT.

6.5 Analysis of Acoustic Modulus Spectra

6.5.1 α Relaxation Peak

We first present the analysis of the acoustic modulus spectra above 263K where the peak or the high-ω wing were observed. Around the α relaxation peak, the acoustic modulus can be expressed in terms of the relaxation function spectrum $h(z)$ as

$$M_R(z)/\rho_0 = (c_\infty^2 - c_0^2) - (c_\infty^2 - c_0^2)h(z), \tag{6.1}$$

$h(z)$ is related to the relaxation function $\varphi(t)$ such as the KWW function through the relaxation

$$h(z) = \int_{-\infty}^{+\infty} dte^{zt}[-d\varphi(t)/dt]. \tag{6.2}$$

Both the real and imaginary parts of spectra were simultaneously fitted to Eq. 6.1 with the stretched exponential relaxation function $\varphi(t)$. The solid lines in Figs. 6-5 and 6-6 represent the fits. Note that with the two limiting velocities c_0 and c_∞ fixed at the values determined as described above, there are only two free parameters left: the structural relaxation time τ_L and stretching parameter β. Within experimental error, the stretching parameter shows no T-dependence with $\beta \approx 0.50$ in the temperature range of 263K to 290K. Above 290K, the relaxation spectra move out of our experimental frequency window to much higher frequencies, which do not permit characterization of the relaxation dynamics. Below 263K, the relaxation peak is farther away at low frequency and only a portion of the high-ω wing is observed in M''_R/ρ_0. Also, M'_R/ρ_0 (Part B of Fig. 6-6) is almost constant across the acoustic frequency window probed in this T range. Therefore we have not tried to fit the spectra with Eq. 6.1. Within MCT at low T these parts of spectra should be located in the β-relaxation regime and should follow the β relaxation dynamics described

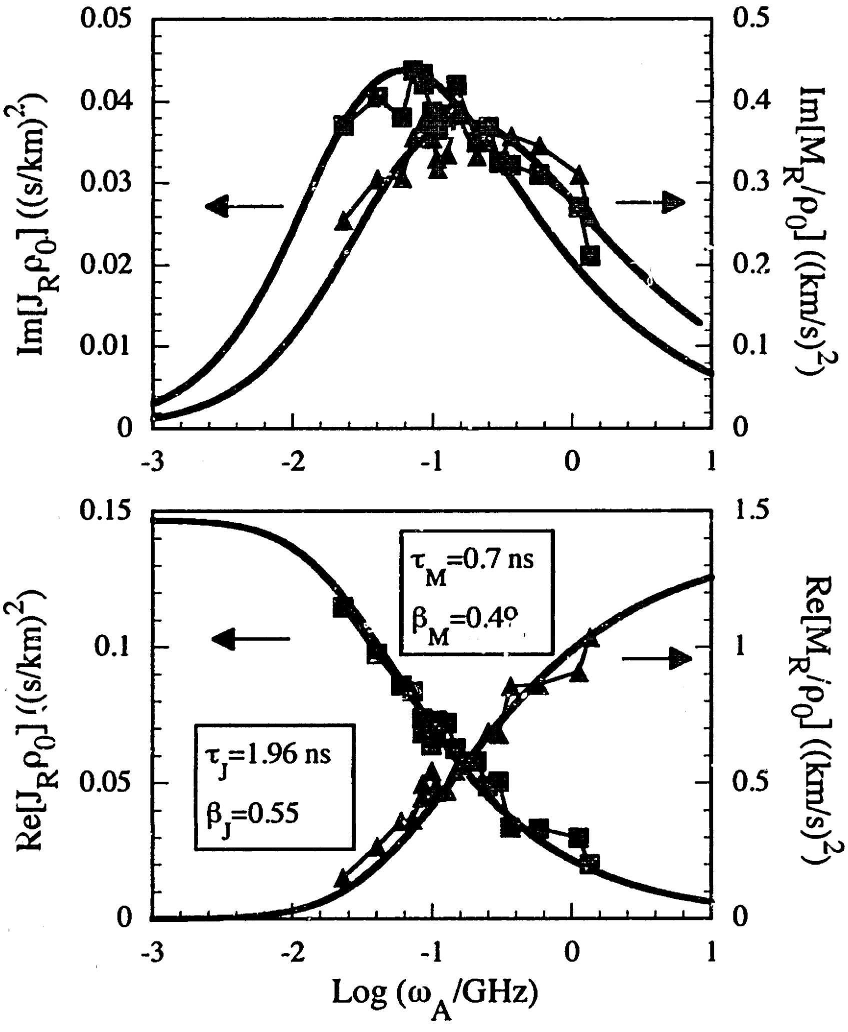

Figure 6-7: Comparison between the longitudinal acoustic modulus and compliance spectra of salol at 270K. The compliance spectrum is narrower than the modulus spectra and peaks at lower frequency.

by Eq. 1.45. We will present the analysis of those spectra at $T \leq 263$K in Sec. 6.5.2.

The compliance spectra above 263K show features similar to their counterpart modulus spectra: a peak at 270K, low-ω wing at higher T, and high-ω side at lower T. However, they are significantly different from each other quantitatively. The difference between them is exemplified in Fig. 6-7, where the real and imaginary parts of the compliance and modulus at 270K are shown along with the fits. The modulus spectrum is broader and has a maximum at higher frequency. The average relaxation times $<\tau_J>$ and $<\tau_L>$ satisfy the relaxation $<\tau_J>=<\tau_L> M_\infty/M_0$ approximately, where the average relaxation time $<\tau>=\tau\Gamma(1/\beta)/\beta$. The average relaxation times $<\tau_J>$ and $<\tau_L>$ are plotted as functions of temperature in Fig. 6-8, together with those from ISTS (Chapter 4), DLS [9], and PCS [68]. While $<\tau_J>$ values at 263K and 270K are approximately equal to $<\tau_R>$ values from ISTS, they seem to deviate from $<\tau_R>$ above 270K. This suggestion, however, needs further experimental investigation because only part of the relaxation spectra at these temperatures was observed. Thus there are large uncertainties for the $<\tau_J>$ determined at these temperatures.

6.5.2 β-Relaxation Regime

Figure 6-9 displays the real and imaginary parts of the reduced acoustic modulus M_R/ρ_0 and compliance $J_R\rho_0$ at temperatures below 263K. The real parts of both modulus and compliance spectra exhibit nearly no frequency dependence at any T except 263K where the relaxation peak is close to the experimental window. However, the imaginary parts show significant changes across our experimental frequency range. We thus focus on the imaginary part of the spectrum. First we plot both M_R''/ρ_0 and $J_R''\rho_0$ in a double log-log scale in Fig. 6-10. As can be seen, the shapes of both spectra at lower three temperatures resemble each other in the entire frequency range. This is not surprising, given the relation $J_R'' = M_R''/|M_R|^2$. Since $|M_R|^2 \approx |M_R'|^2$ away from the α peak and M_R' is almost frequency-independent as shown in Part B of Fig. 6-9, one thus has $J_R'' \propto M_R''$. According to MCT, these parts of the spectra are in the β-relaxation regime and can be described by the

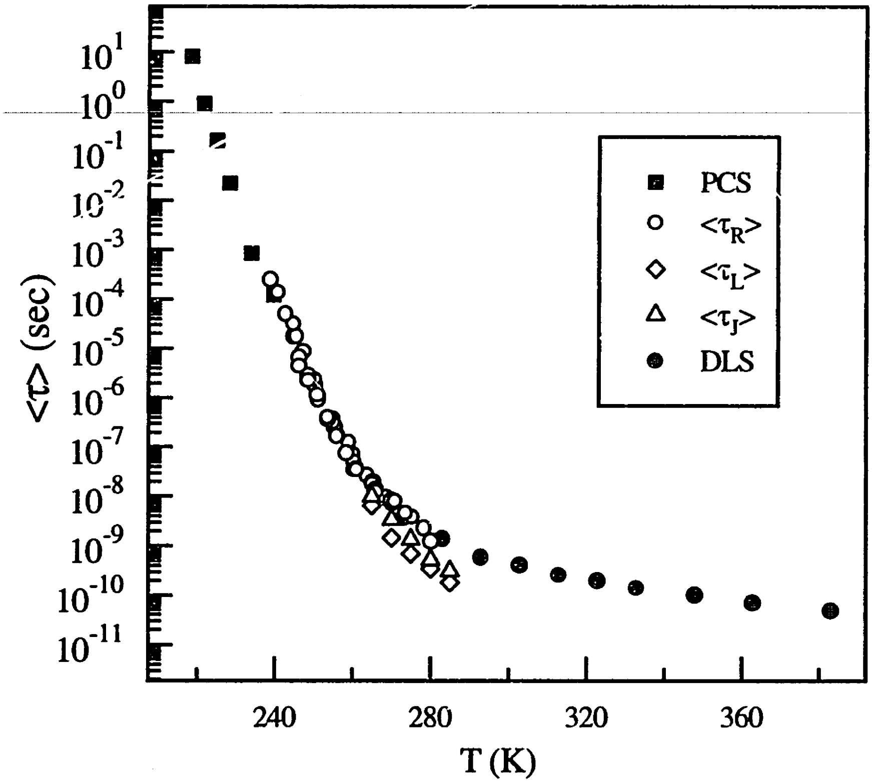

Figure 6-8: The temperature dependence of $<\tau>$ of salol from ISS acoustic data (open diamonds, open triangles), ISTS relaxation mode in Chapter 4 (open circles), depolarized light scattering (solid circles), and photon correlation spectroscopy (solid squares). $<\tau_J>$ is approximately equal to $<\tau_L> M_\infty/M_0$.

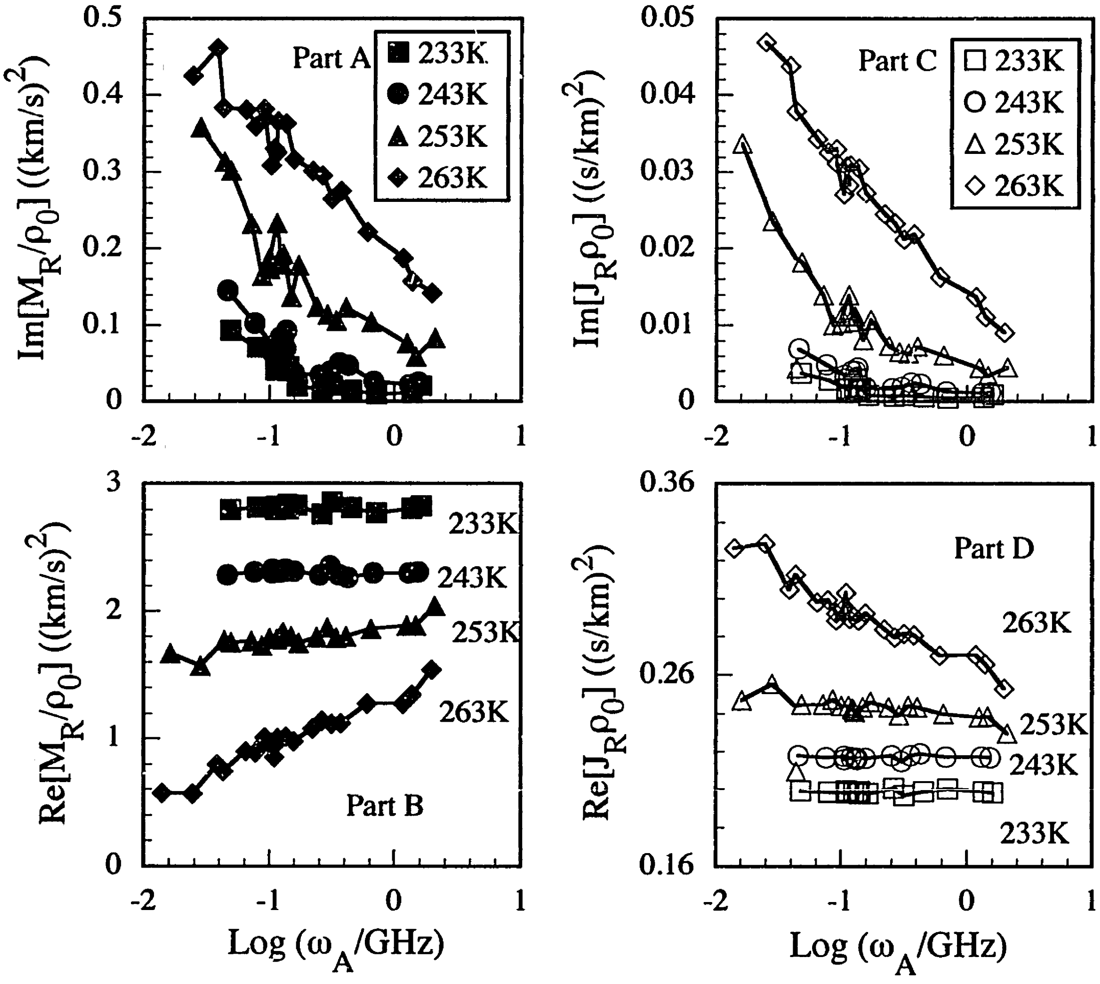

Figure 6-9: The relaxational parts of the reduced longitudinal acoustic modulus and compliance of salol below 263K. Both of the real parts (Part B and Part D) show almost no frequency dependence except at 263K. Their imaginary parts, however, show noticeable changes with frequency.

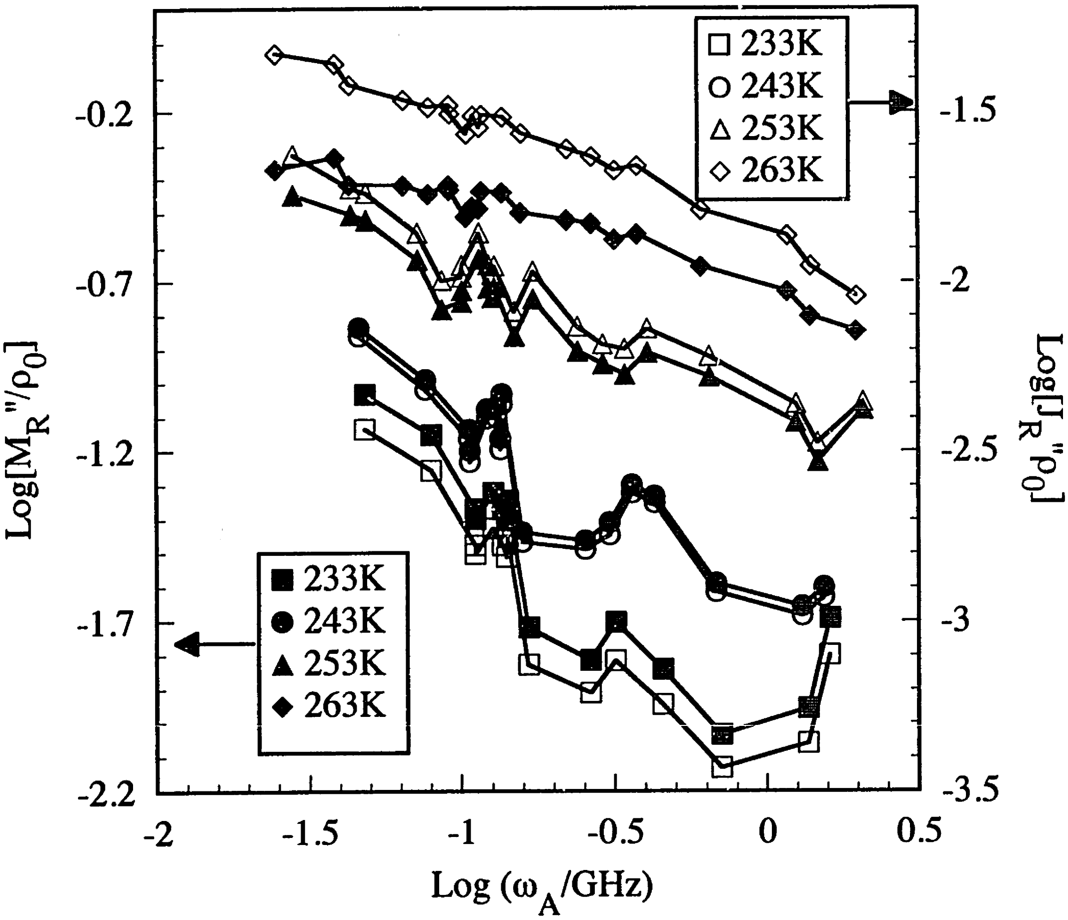

Figure 6-10: The imaginary parts of the reduced longitudinal acoustic modulus and compliance of salol shown in Fig. 6-9 are plotted on the log-log scale. Except at 263K, the shapes of both spectra resemble each other in the whole frequency range.

interpolation function of Eq. 1.45. Due to our limited frequency window, fitting of the spectra to Eq. 1.45 is not practical. Instead, we will follow theoretical guidelines to compare the acoustic modulus and compliance spectra with the β-susceptibility spectra obtained from DLS, which covers a higher frequency range than ISS.

As predicted by MCT, the acoustic modulus spectrum (see Eq. 1.34), the compliance spectrum, and the susceptibility spectrum from DLS can be described by a single β-susceptibility spectrum $\chi''(\omega)$ up to a multiplying factor. In the $\log \chi''$ versus $\log \omega$ plot, all the spectra should overlap by shifting the spectra along the ordinate. The β-susceptibility spectra $\chi''(\omega; T)$ have been obtained from the depolarized light scattering spectra in the range sub-GHz to 5THz [82]. We therefore plot in Fig. 6-11 the DLS spectra (thin solid curves), reduced acoustic modulus spectra M''_R/ρ_0 (open symbols), and reduced compliance spectra $J''_R\rho_0$ (solid symbols) along with the β-susceptibility spectra $\chi''(\omega)$ (thick solid curves) deduced from the DLS susceptibility spectra, including extrapolation to lower frequencies than those covered by the DLS spectra, at several temperatures on a log-log scale. As can be seen from Fig. 6-11, the acoustic spectra M''_R/ρ_0 and $J''_R\rho_0$ at three lower temperatures overlap with the low-frequency part of DLS spectra and coincide with the predicted β-susceptibility spectra $\chi''(\omega)$. At 263K, only part of data overlaps with $\chi''(\omega)$, presumably because it is close to the α relaxation peak. Although only part of the β-susceptibility spectra was observed in M''_R/ρ_0 and $J''_R\rho_0$, which do not permit determination of the minimum frequency, the results nevertheless show that the acoustic data are consistent with β-susceptibility spectra $\chi''(\omega)$ derived from DLS.

To overlap the spectra at each T, we have shifted M''_R/ρ_0 and $J''_R\rho_0$ along the ordinate. The temperature dependences of the amount shifted, $\log(h_{DLS}/h_M)$ and $\log(h_{DLS}/h_J)$, are shown in Fig. 6-12. Since we are dealing with M''_R/ρ_0 and $J''_R\rho_0$, not M''_R and J''_R directly, we have not accounted for T-dependence of density ρ_0. Also, as discussed in Ref. [87], the critical amplitude h_{DLS} from fitting of the DLS spectra with the MCT predictions is temperature dependent. T-dependences of both density ρ_0 and amplitude h_{DLS} may therefore contribute to the smooth temperature dependence of $\log(h_{DLS}/h_M)$ and $\log(h_{DLS}/h_J)$.

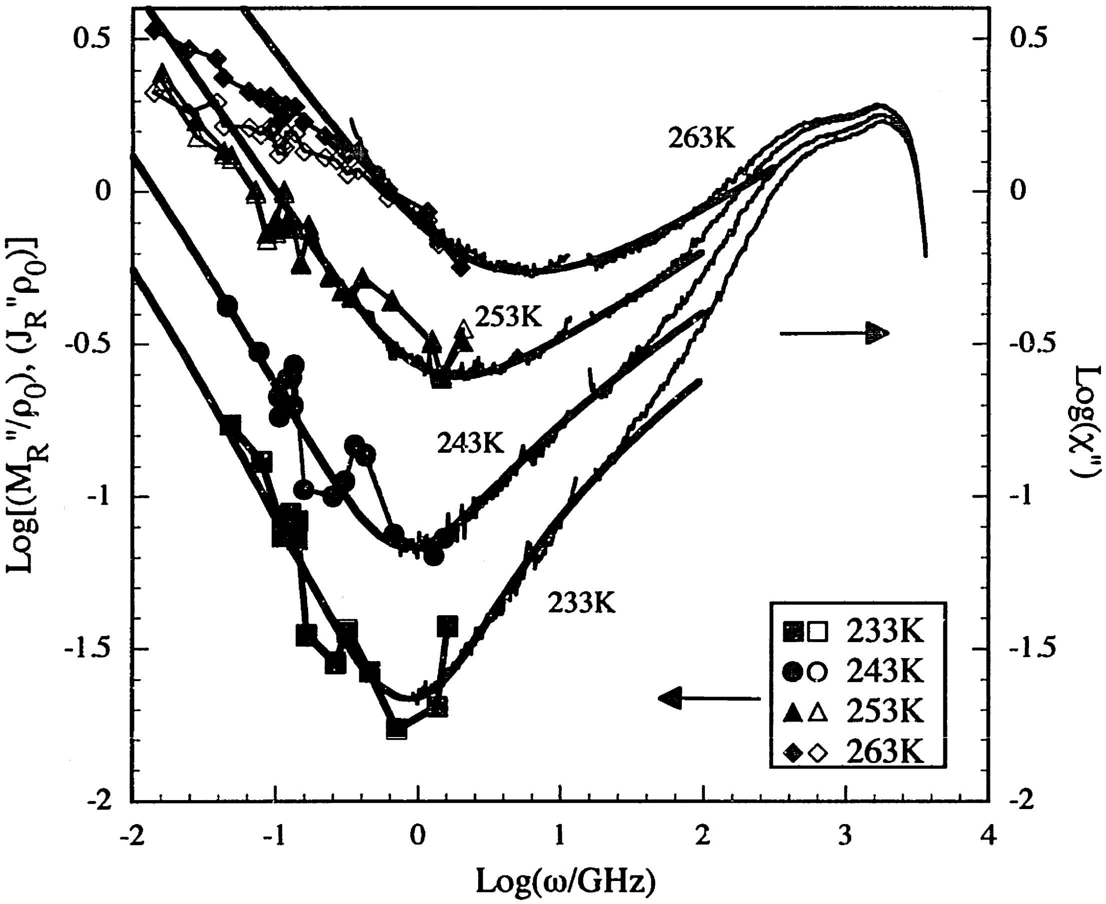

Figure 6-11: Relaxational spectra of salol from ISS acoustic data (symbols), together with DLS susceptibility spectra (thin lines) and the extended MCT fits (thick lines). The spectra shown in Fig. 6-10 have been shifted along the ordinate to overlap the DLS susceptibility spectra.

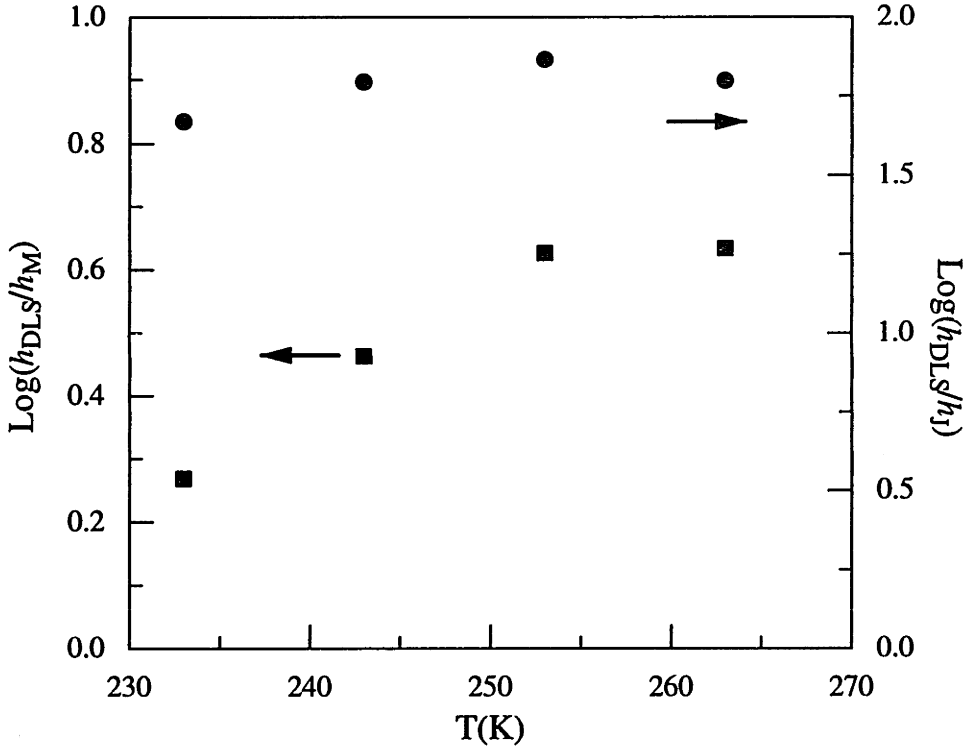

Figure 6-12: The temperature dependences of $\log(h_{DLS}/h_M)$ and $\log(h_{DLS}/h_J)$. These two quantities are the amounts shifted along the ordinate to overlap the acoustic modulus spectra and compliance spectra with the β-susceptibility spectra derived from the DLS experiment.

6.6 Conclusions

Impulsive stimulated light scattering experiments have been carried out to study the structural relaxation of a supercooled organic liquid, salol. Longitudinal acoustic modes are characterized over 2 decades of acoustic frequencies from 10 MHz to several GHz. The relaxation dynamics are analyzed through the frequency-dependent structural relaxational part of acoustic modulus and compliance spectra, which are constructed from the measured acoustic frequencies and modified damping rates (after subtracting the background contribution). The observed structural relaxation parts of the acoustic modulus and compliance above 263K are fitted to the α relaxational spectrum described by the KWW function. Within experimental error, the stretching parameter β is found to be T-independent in the range from 263K to 290K. The spectra below 263K are found to be coincident with β-susceptibility spectra derived from DLS up to a multiplying factor.

While our results are consistent with one of the MCT predictions that any correlation functions of quantities coupled to the density fluctuations have the factorization property shown in Eq. 3.29 in the β-relaxation regime, only part of the β-susceptibility spectra was measured in our acoustic experiment. The important β relaxation parts were not mapped out thoroughly and thus the minimum frequencies could not be determined. Previous studies on salol by Brillouin scattering have been reported [36, 46]. One was performed at a 90° scattering angle [36] and the other at 173° [46]. From these studies we can extend our acoustic modulus spectra to much higher frequency range. However, one study did not give the width of the Brillouin peaks [46] and the other did not cover a wide enough temperature range [36]. Thus estimation of the background contribution to the width of the Brillouin peaks is not possible. In the latter case, if we neglect the background contribution and calculate the acoustic modulus, the data points at 253K and 263K are well above our highest-frequency data points in Fig. 6-11 (Data were not reported below 248K.). Therefore, more acoustic measurements in the high frequency range are needed to test the MCT predictions in the entire β-relaxation regime. Our study simply shows that the results are consistent with other measurements, but does not provide strong new evidence in support of MCT. The most stringent test would be to map out the acoustic modulus spectrum in the β-relaxation regime including the β relaxation, to determine the power law exponents, to measure the minimum frequency and minimum acoustic modulus, and then to compare the results with those from DLS. Much effort in this direction is needed to elucidate the acoustic dynamics in the β-relaxation regime.

In conclusion, we have demonstrated, by using the glass-former salol as an example, that ISS is useful for measuring the acoustic dynamics over a range of MHz-GHz frequencies which is inaccessible to other techniques. We have also presented a guideline for analyzing the acoustic dynamics. The measured acoustic damping rate contains a background contribution, which is often ignored, and a contribution from the structural relaxation. One way to account for this, as in the present chapter, is to subtract the background contribution from the measured total acoustic damping rate and then calculate the structural relaxation part of the longitudinal acoustic modulus spectra. The other way is to calculate the total acoustic modulus spectra and then analyze the spectra by including a linear-ω-dependent term and a structural relaxation term in the fitting function. Through this data analysis, we have shown that our results are in agreement with the results from depolarized light scattering studies and the prediction of the mode coupling theory.

Chapter 7

Orientational Relaxation and Transverse Acoustic Wave Propagation in Salol

7.1 Introduction

In Chapters 2-6, we have described VV impulsive stimulated light scattering from viscous liquids. The VV ISS data of supercooled liquids as presented in Chapters 4-6 show characteristic viscoelastic features. Upon cooling, transport coefficients such as viscosity and thermodynamic derivatives such as acoustic modulus as we have modeled in Chapter 3 become frequency dependent. We have demonstrated that VV ISS is very useful for studying structural relaxation in glass-forming materials.

The slowing down of structural relaxation is also manifest in depolarized light scattering spectra. A particular signature of structural relaxation is the Rytov Dip, i.e. a negative central line observed in the depolarized spectrum [35, 89]. It is generally explained in terms of coupling between the molecular anisotropy density and the transverse current [90-92]. However, if the elasto-optic, Pockels constants are assumed to be frequency dependent, one would obtain a Rytov Dip [93] even for point particles with scalar polarizability [94, 95]. In the latter case for an isotropic system, multiple scattering from density fluctuations or dipole-induced-dipole (DID) contribution is the origin of the depolarized light scattering, in addition to the contribution from the transverse acoustic mode at low temperatures. Recently, depolarized light scattering spectra of supercooled liquids with more than four decades of frequency range have been recorded on a number of glass formers including salol [9], CKN [10], propylene carbonate [69], glycerol [96], Zinc Chloride [97], o-terphenyl [98], tricresyl phosphate and glycerol [99], and m-toluidine [100], and have been found to exhibit many of the characteristics predicted by mode coupling theory. In order to compare the DLS spectra directly with the predictions of MCT which concerns the density fluctuation dynamics, the spectra for some of the materials have been interpreted as arising primarily from multiple scattering or DID mechanism. A recent study [101] has shown that DLS spectra in salol arise predominantly from orientational fluctuations instead of DID. The question becomes why the orientational correlators measured in DLS exhibit the same properties as the density correlators predicted in MCT.

Features analogous to those in VH Rayleigh-Brillouin scattering have been observed in time-resolved depolarized impulsive stimulated depolarized light scattering (VH ISS) on the glass-forming liquid triphenyl phosphite [51]. The orientational dynamics and the structural relaxation spectrum associated with the transverse acoustic motion have been investigated at a number of excitation wavevectors. In this Chapter, we report preliminary results of a VH ISS study on salol. Our main objective is to study the structural relaxation processes which couple to the shear acoustic mode. By mapping out both the longitudinal acoustic modulus spectrum and transverse acoustic modulus spectrum, one would obtain the compressibility spectrum which cannot usually be measured directly. We also want to characterize the orientational relaxation processes and compare the results with those from other measurements.

7.2 Experimental Procedures

The experimental setup is similar to the one with the pulse probe system (Fig.2-3) as described in Chapter 2. There the two excitation beams, probe beam and the signal beam are all *s*-polarized. Here the two excitation beams are cross-polarized. One is *s*-polarized and the other *p*-polarized. They are crossed at an excitation angle θ_E to create a periodically changing polarization field with the wavevector q determined by Eq. 2.1. Molecular orientational motion and shear motion are excited through impulsive stimulated Rayleigh-Brillouin scattering. The probe pulse is incident upon the grating at the Bragg angle with *p*- or *s*- polarization, chosen to be opposite that of the polarization of the closest excitation beam. The signal beam is cross-polarized with respect to the probe beam. The time-dependent material responses are monitored by recording the diffraction efficiency of the probe pulse as a function of the delay time between the pump and probe pulses. The time delay between the pump and probe pulses is controlled electronically as described in Chapter 2.

The salol sample was prepared as described in Chapter 4. The excitation angles used in this study are 1.45°, 8.65°, 37.90°, 44.93°, and 54.63°, corresponding to wavelengths of 42.04, 7.062, 1.640, 1.393, and 1.159 μm, respectively.

7.3 Preliminary Data and Analysis

The data collected at the smallest angle of 1.45° are shown in Fig. 7-1 from 340.4K to 280.2K. At temperatures above 350K, which are not included in Fig. 7-1, the signal contains only an instantaneous electronic response, a pulse-duration limited spike at $t = 0$. The nuclear response at these temperatures relaxes too fast to be observed with long laser pulses (about 100 ps). At about 340K, a relaxational tail appears following the $t = 0$ peak. As the temperature is reduced, the relaxation decay becomes slow and the intensity of the signal decreases. This is presumably because at low temperature the sample is stiffer so that the extent of orientational alignment induced by the impulsive excitation fields is less. Below 260K, the ori-

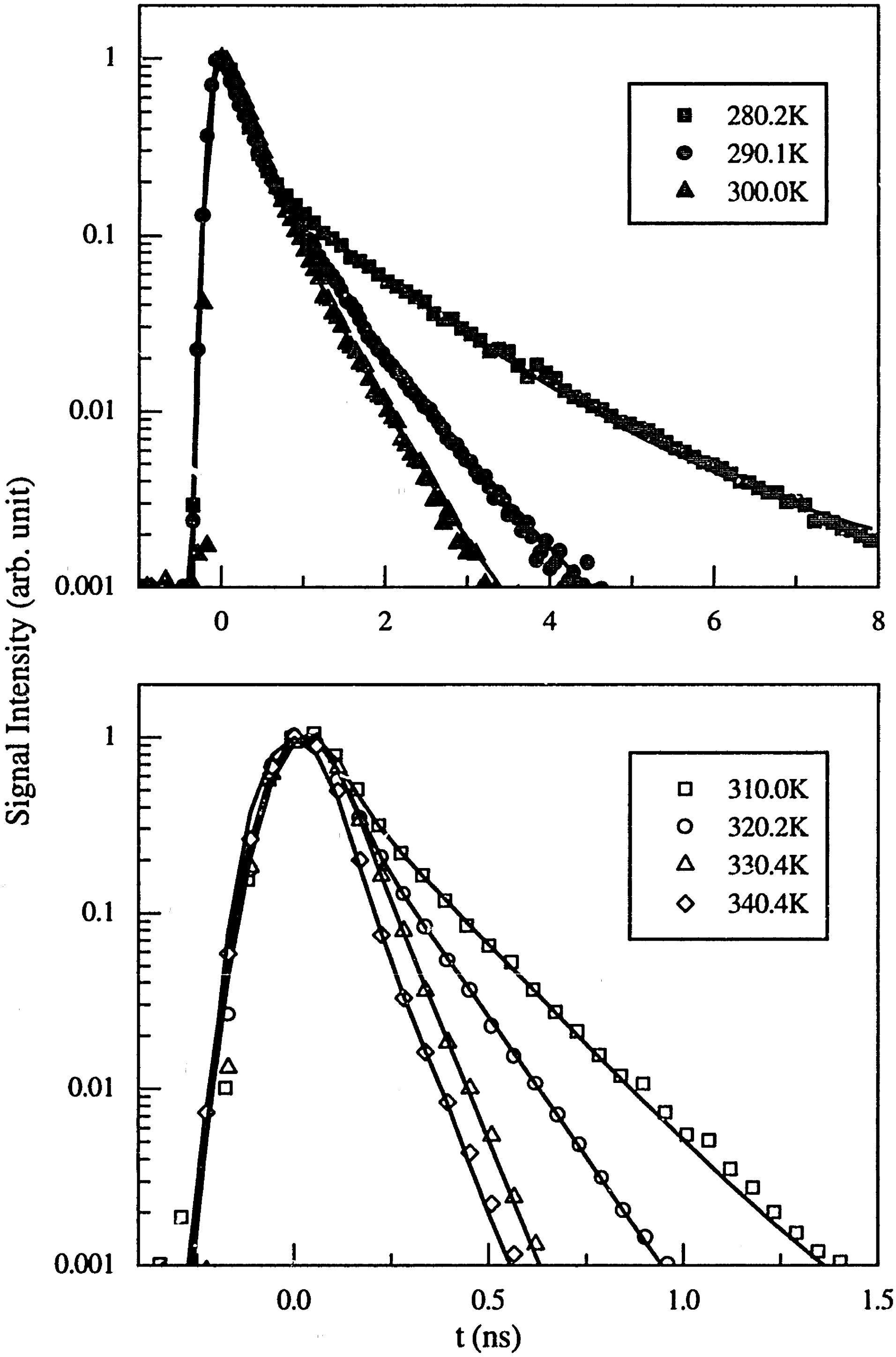

Figure 7-1: VH ISS data collected at an excitation angle of $\theta_E = 1.45°$ at high temperatures. The intensity is shown on a log scale. The symbols represent data at different temperatures and the solid lines are fits to the data with Eq. 7.1. Note that the intensities for different temperatures have been rescaled to 1 according to the electronic peak at $t = 0$.

entational response moves to even longer time scales and the signal intensity is too weak to be detected. This limits the temperature range over which the orientational dynamics can be measured with the current laser systems. We will discuss possible improvements in the next section.

At larger excitation angles, data at high temperatures show features similar to those shown in Fig. 7-1. But as temperature is decreased, an additional oscillatory feature grows in, which is due to transverse acoustic waves. The shear acoustic mode is excited through depolarized impulsive stimulated Brillouin scattering. The ISBS signal intensity is proportional to the square of the wavevector. This is the reason that the shear mode is not observed in the data at small excitation angles even at very low temperatures. This limits the range of wavevectors over which the shear acoustic mode can be observed, unlike the case of the longitudinal acoustic mode as described in Chapter 6, for which there is another excitation mechanism, impulsive stimulated thermal scattering, which is efficient at any wavevector.

Figure 7-2 shows the data collected at an excitation angle of 44.93° at low temperatures. Starting at about 280K, in addition to the orientational decay, the shear mode is observed but is heavily damped. As the temperature is reduced, the oscillatory feature becomes more obvious. At even lower temperatures, only the underdamped shear acoustic mode excited through ISBS is observed in the data. Due to the q^2-dependence of ISBS signal intensity from the shear mode and the q-dependence of the shear acoustic frequency, the transverse acoustic mode is observed at higher temperatures for larger excitation angles.

7.3.1 Orientational Relaxation Dynamics

For the orientational relaxation dynamics, we have employed an empirical response function $G_{VH}(t)$ to fit the data. As in the previous study [51], $G_{VH}(t)$ contains a bi-exponential decay for the orientational response and a delta-function for the instantaneous electronic response. The scattering intensity is then,

$$I_{\mathrm{VH}} = |G_{VH}(t)|^2 = \left[A_0\delta(t) + A_1 e^{-t/\tau_1} + A_2 e^{-t/\tau_2}\right]^2 . \tag{7.1}$$

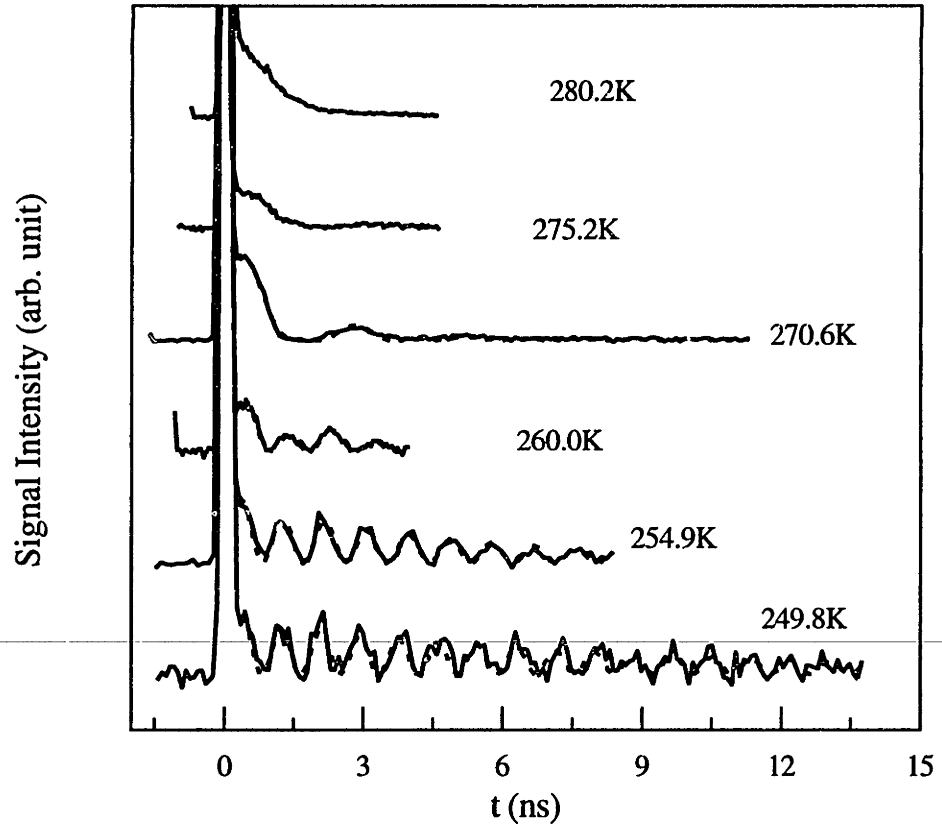

Figure 7-2: VH ISS data recorded with an excitation angle of 8.65° at low temperatures. The data show the oscillatory features which represent the excited shear acoustic mode.

Fits to Eq. 7.1 incorporating numerical convolution over pump and probe pulses are represented by the solid lines in Fig. 7-1. Of the two relaxation times, only the larger one is well characterized and is found to be q-independent. The temperature dependent behavior of this slower orientational relaxation time is shown in Fig 7-3, together with values obtained from previous studies by depolarized Rayleigh-Brillouin scattering [35] and optical Kerr spectroscopy [102]. The three sets of data are in good agreement in their overlap regions within their experimental errors. In Ref. [102], an Arrhenius law was suggested for the Kerr orientational relaxation times from 280.2K to 350.2K, which seems to be supported by the data in the same temperature region from this study and Ref. [35]. However, the Arrhenius law represented by the thick solid line in Fig. 7-3 is not obeyed if the reorientational times at the lower temperatures from this study are included. The lowest temperature reached in this study is 260.0K. Figure 7-3 also shows the average relaxation times from ISTS measurements of the relaxation mode (Chapter 4), depolarized light scattering [9], and polarized photon correlation spectroscopy [68]. The data covering more than 11 decades in time show smooth variation from 395.2K to 218.5K. Note that in the DLS study [9], the α relaxation peaks were measured over a wide frequency range and fitted to a KWW relaxation function. The DLS results shown in Figure 7-3 are the average relaxation times.

7.3.2 Transverse Acoustic Dynamics

For the data at low temperatures, we have included a sinusoidal term in the fitting function which accounts for the shear acoustic wave propagation. The nuclear response function is then given by

$$G_{\mathrm{VH}}(t) = A_1 e^{-t/\tau_1} + A_2 e^{-t/\tau_2} + A_S e^{-\Gamma_S t} \sin(\omega_S t), \tag{7.2}$$

where Γ_S and ω_S denote the shear acoustic damping rate and frequency respectively. Fits to the data are shown as the solid curves in Fig 7-2. Note that in fitting the data where there is an orientational relaxation contribution, we have fixed the ori-

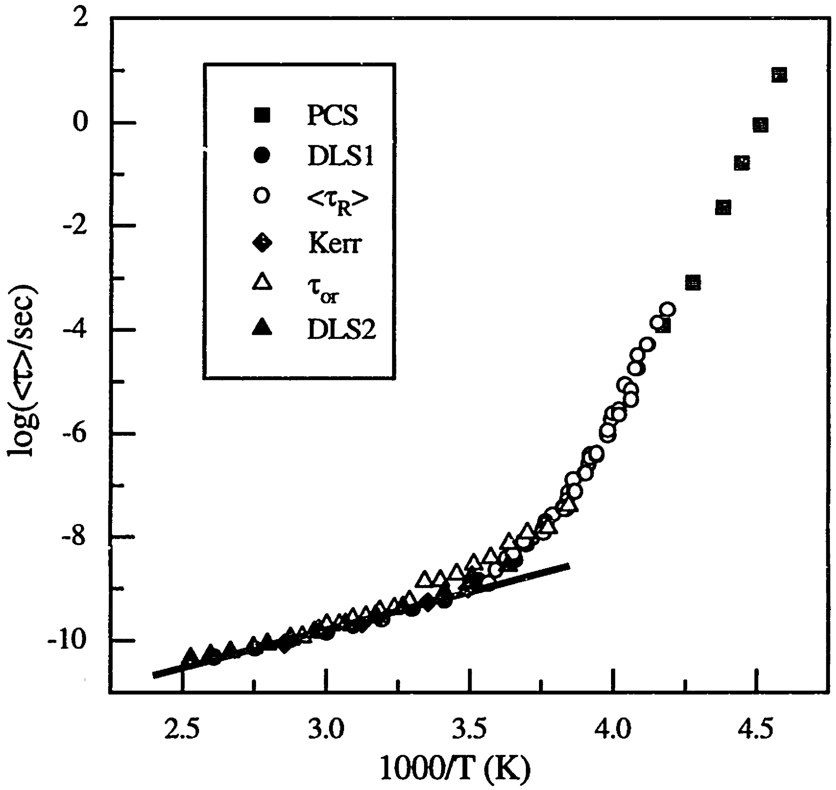

Figure 7-3: Arrhenius plot of the relaxation times in salol of the orientational mode measured in VH ISS (open triangles), the Mountain mode measured in ISTS (Chapter 4, open circles), depolarized light scattering (DLS1) [9] (solid circles), depolarized Rayleigh-Brillouin scattering (DLS2) [35] (solid triangles), the relaxational mode observed in polarized photon correlation spectroscopy [68] (solid squares), and orientational mode results from optical Kerr spectroscopy [102] (solid diamonds). The Arrhenius law which was suggested in Ref. [102] is presented by the thick solid line. Clearly it only describes the orientational dynamics in a narrow temperature range. The orientational relaxation time at 260.0K from this study deviates from the suggested Arrhenius law by more than 1 decade.

entational decay time as those determined from the data at the smallest angle in order to reduce the number of free fitting parameters. From the best fitting parameters Γ_S and ω_S, the shear acoustic modulus values $G(\omega_S)$ are determined through the Eqs. 3.38 and 3.39 with the shear acoustic frequency ω_S and damping rate Γ_S replacing their longitudinal counterparts. The real and imaginary parts of the reduced shear modulus $G'(\omega_S)/\rho_0$ and $G''(\omega_S)/\rho_0$ are plotted in Fig 7-4 as a function of temperature for the three different wavevectors. They exhibit similar qualitative features as the longitudinal acoustic modulus. The real part of the shear modulus increases (from near 0) as temperature is decreased, and the imaginary part shows a maximum at an intermediate temperature. These changes are induced by the structural relaxation whose spectrum sweeps across the shear acoustic frequency from high frequency at high temperatures to low frequency at low temperatures. Due to the limited shear acoustic frequency range probed, we are not able to quantitatively characterize structural relaxation coupled to the shear motion in the current stage.

7.4 Discussion

Orientational relaxation dynamics and transverse acoustic wave propagation are studied by impulsive stimulated depolarized light scattering. As it stands now, the study is incomplete both theoretically and experimentally. On the theoretical side, a model for the response function $G_{VH}(t)$ is needed to interpret the VH ISS data on glass-forming liquids. On the experimental side, emphasis should be placed on extending the method to longer and especially to shorter time scales. Depolarized light scattering spectra from salol [9, 82] from sub-GHz to THz have shown power-law dependences (α and β relaxations) of the orientational relaxation dynamics, which are consistent with the MCT descriptions of the liquid-glass transition. Since it still remains to be shown that the orientational correlations exhibit the same properties as the density correlators, more experimental results would help to resolve this issue. To do this will require the use of multiple laser systems. For very fast

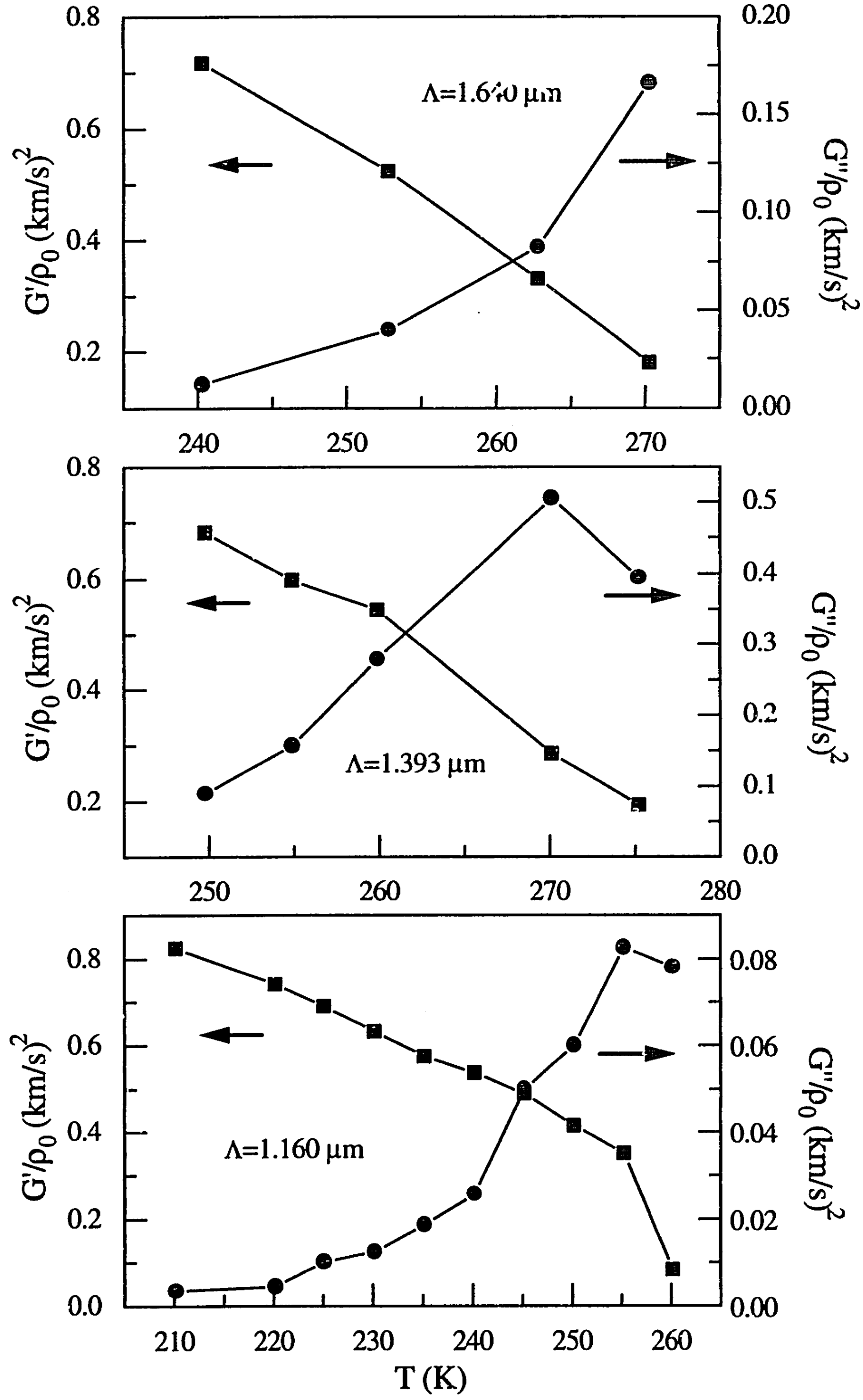

Figure 7-4: Real part $G'(\omega_S)/\rho_0$ (Part A) and imaginary part $G''(\omega_S)/\rho_0$ (Part B) of the shear acoustic modulus as a function of temperature for three wavelengths. The data show typical glassy behavior as for the longitudinal acoustic modulus discussed in Chapter 6.

librational and orientational dynamics, one must use femtosecond/subpicosecond lasers as excitation and probe sources. By using picosecond/nanosecond lasers, the dynamic range can be extended to microseconds or longer. Combination of the data collected with different systems yields orientational dynamics on fs to many μs time scales, which allows theoretical predictions to be critically tested. This is similar to the data collection of depolarized light scattering, in which different interferometers and spectrometers are used to resolve the dynamics in different frequency regions. The information content of ISS data is in principle identical to that of the DLS spectra. In some cases, however, there should be advantages of the time-resolved ISS method over DLS in the frequency domain. The short-time dynamics with vibrational character, so-called librational motion or Boson peak in glass, can be observed directly in the time domain [103, 104], while it is difficult to discern any vibrational mode in DLS. In addition, there are more combinations of different polarizations of the excitation and probe beams in ISS than those in depolarized light scattering. Therefore one can use different polarization combinations of the pump and probe pulses to probe different dielectric tensor components and possibly to separate contributions from shear, orientational, and other processes [103, 104].

We have characterized the shear acoustic mode for three different wavevectors. Clearly it is necessary to measure shear acoustic dynamics at more excitation wavevectors in order to extract the temperature and frequency dependences of the structural relaxations that couple to the shear motion. The results can then be compared to those from the longitudinal acoustic dynamics measurements.

Chapter 8

Conclusions and Suggestions for Future Research

8.1 Summary

In this thesis, we have reported both theoretical and experimental studies of time-resolved VV/VH impulsive stimulated light scattering on glass-forming liquids. We have developed a theoretical understanding of the viscoelastic properties measured in VV ISS experiments. We have investigated structural relaxation in two different kinds of glass formers. The experimental results have been compared with the predictions of the mode coupling theory of the liquid-glass transition.

In Chapter 3, we have presented a theoretical model for VV ISS on viscous liquids. By using the generalized hydrodynamics equations we have derived the density response functions to the impulsive heating (ISTS) and impulsive electrostrictive force (ISBS). There are three modes in the ISTS response function including the acoustic mode, thermal diffusion mode, and relaxation or Mountain mode. The ISBS response function primarily contains only one mode which is the acoustic mode. Characterization of the relaxation mode in ISTS gives the structural relaxation dynamics and the relaxation strength, or Debye-Waller factor, in the low wavevector limit. The latter is one of the important parameters specifying α relaxation, and its temperature dependence is predicted in MCT to show a square-root cusp at a crossover temperature. ISTS provides an alternate pathway to neutron scattering for measurement of the Debye-Waller factor and thus for testing of one of the central predictions of MCT.

Both ISTS and ISBS provide the same acoustic dynamics. When its spectrum overlaps the acoustic frequency, structural relaxation induces the greatest acoustic dispersion and yields a maximum in the acoustic damping rate. If the structural relaxation spectrum is well above or below the acoustic frequency, the sample behaves either like a normal liquid or like a glass, and the zero-frequency velocity c_0 or infinity-frequency velocity c_∞ is then measured. Therefore by studying the acoustic dynamics either from ISTS or ISBS, one can obtain structural relaxation dynamics information. Normally one introduces a frequency dependent longitudinal acoustic modulus, which can be constructed as a function of the acoustic frequency from the acoustic parameters measured at multiple wevevectors. We have outlined a basis for the acoustic data analysis. The acoustic damping rate comes from the structural relaxation contribution and the background contribution from viscosities and thermal diffusion processes. The latter is present at any temperature from the liquid state to the supercooled state to the glass state, while structural relaxation makes a contribution only when its spectrum overlaps with the acoustic frequency. Therefore care has to be taken to analyze the acoustic modulus spectrum. One can either include a linear-ω-dependent term, which represents the contribution of the viscosities and thermal diffusion, plus a relaxation function in the fitting function to the total acoustic modulus spectrum. Alternatively, one can subtract the background contribution first from the measured total acoustic damping rate to obtain the structural relaxational part of the acoustic damping rate, and then calculate the structural relaxational part of the longitudinal acoustic modulus.

The acoustic, thermal diffusion, and structural relaxation modes shown in ISTS data are closely analogous to the Brillouin, Rayleigh, and Mountain peaks, respectively, which appear in Rayleigh-Brillouin scattering spectra. Concerning the dynamics, the individual modes are related to each other through Fourier transformation. Therefore, they provide the same dynamical information in principle. The

ISTS and BS data differ in the amplitude ratios between the three modes, but again in principle the same information, from which the relaxation strength can be determined, may be obtained. However, in practice, the dynamic window and the wavevector range accessible to Rayleigh-Brillouin scattering are limited, especially at very small wavevectors. Due to the strong temperature dependence of the Mountain mode dynamics, the relaxation dynamics and strength cannot be determined over a wide temperature range.

There is a fundamental similarity between the structure of the theoretical formalism describing MCT and ISS. This indicates a mapping of the results of ISS measurements onto the MCT parameters. The examination of α-relaxation dynamics and strength reflected in the Mountain mode and acoustic behavior influenced by parts of the α and β relaxation spectra presented in this thesis represents some, but not all, of the possibilities for testing of MCT through ISS measurements. Extension of the temporal and wavevector ranges accessible to ISS will enlarge the scope of our critical testing of MCT.

In Chapters 4 and 5, we have reported experimental studies of VV ISS on an organic molecular liquid salol and an ionic salt mixture $Ca_{0.4}K_{0.6}(NO_3)_{1.4}$. The data show all the features discussed in our theoretical model in Chapter 3. Of all three modes including the acoustic, thermal diffusion, and structural relaxation modes, we have particularly characterized the structural relaxation mode concerning its dynamics and strength. When the three modes are well separated from each other in time, the relaxation mode dynamics and its strength or the Debye-Waller factor are determined. By collecting data at a wide range of wavevectors that allows all three modes to be separated in time in different temperature ranges, we are able to determine the relaxation mode dynamics and strength over a wide temperature range. The temperature dependences of the Debye-Waller factors $f_{q\to 0}$ of salol and CKN both show a square-root cusp at their crossover temperatures T_c. The values of T_c determined are consistent with those from neutron scattering studies. These findings support the MCT prediction that there is a dynamic crossover at a q-independent temperature T_c. The relaxation mode dynamics for both salol and

CKN are well fitted to a stretched exponential (KWW) function at all temperatures determined in our studies. In both cases, the relaxation dynamics as well as the Debye-Waller factor show no q-dependence in the wavevector range we used, which is essentially in the $q \rightarrow 0$ limit. The stretching parameters β which specify the structural relaxation spectral width show significant changes around T_c. However, the values of β are nearly constant at well above T_c and well below T_c. By combining the results from neutron scattering, depolarized light scattering, and photon correlation spectroscopy, these trends are seen to extend to even higher and lower temperatures. The stretching parameters β for salol and CKN from all four experiments show sigmodial shapes with most of the variation at temperatures of around T_c, indicating dynamical changes suggested by MCT. The average relaxation times from our studies on salol and CKN cover the gap between PCS and DLS measurements and show smooth variations between the two. The $<\tau_R>$ and β values from ISTS are found to be in agreement with those from PCS in the overlapping region, which supports the assumption in Chapter 3 that both techniques measure a similar dynamical quantity.

The results shown in Chapters 4 and 5 have thus provided support of the MCT predictions. They have also supported our theoretical treatments of VV ISS on relaxing/nonrelaxing liquids as presented in Chapter 3.

In Chapter 6 we have reported a detailed analysis of the acoustic mode in salol and a comparison of the results to the susceptibility spectrum obtained from depolarized light scattering. The longitudinal acoustic waves are characterized by VV ISTS in the 10 MHz - several GHz acoustic frequency range through the use of a wide range of wavevectors. By following the outline given in Chapter 3, the structural relaxational part of the longitudinal acoustic modulus spectra and the compliance spectra are obtained. The spectra at high temperatures are consistent with an empirical description of structural relaxation dynamics in terms of a stretched exponential relaxation function with exponent $\beta_M \approx 0.50$ for the modulus spectra and $\beta_J \approx 0.55$ for the compliance spectra. At low temperatures, the imaginary parts of modulus spectra $M''_R(\omega; T)$ and compliance spectra $J''_R(\omega; T)$ show the same frequency dependence, while the real parts are essentially constant across the acoustic frequency window probed. In log-log plots, the spectra $M''_R(\omega;T)$ and $J''_R(\omega;T)$ can be rescaled by shifting them along the ordinate to overlap with the β-susceptibility spectra $\chi''(\omega;T)$ predicted by the extended MCT, which are based on susceptibility spectra measured by DLS at high frequencies. Although $M''_R(\omega;T)$ and $J''_R(\omega;T)$ overlap with the DLS susceptibility spectra only in a small frequency region, the results nevertheless are in support of the MCT prediction: all the susceptibility spectra $\chi''_{XY}(\omega;T)$ for any variables X and Y which couple to the density fluctuations follow the same frequency dependence as the β-susceptibility spectra $\chi''(\omega;T)$ in the mesoscopic region.

In Chapter 7 we have presented preliminary results of a VH ISS study on salol. The VH ISS experiment provides orientational relaxation dynamics and shear acoustic wave propagation properties. Nonexponential orientational decay is observed at high temperatures. As the temperature is lowered, orientation relaxation slows down and the signal intensity decreases. Upon further cooling, the data show an oscillatory feature in addition to the orientational decay. Finally the orientational relaxation is so slow and its intensity is so low that only an oscillatory feature is observed in the data. The oscillatory feature represents transverse acoustic wave propagation in the medium. It is only seen in the supercooled liquid state when the structural relaxation dynamics are comparable to or slower than the oscillation period of the shear wave, so that the sample shows viscoelastic behavior or effectively behaves like a solid or a glass on the time scale of the acoustic period. Similar to the longitudinal acoustic mode, the transverse acoustic mode shows dispersion when the structural relaxation spectrum overlaps the shear acoustic wave frequency. Due to the limited frequency range available, we are not able to characterize the shear acoustic mode dynamics over a wide T range.

8.2 Suggestions for Future Research

This work has provided a comprehensive study of the viscoelastic properties of glass-forming liquids by VV/VH impulsive stimulated light scattering. Our theoretical model for VV ISS on viscous liquids and subsequent experimental studies on a couple of model glass formers have demonstrated the capability of ISTS for characterization of the Mountain mode dynamics, determination of the Debye-Waller factor $f_{q\to 0}(T)$ and crossover temperature T_c, and testing of mode coupling theory predictions. This method can be extended to other glass formers to measure the Debye-Waller factor and determine the structural relaxation dynamics. The temperature dependence of the Debye-Waller factor directly shows whether MCT applies. Since the current mode coupling theory reviewed in Chapter 1 is not expected to apply to glass formers with strong chemical bonds, it is interesting to see in which samples the MCT does not apply and if there is any correlation between the temperature dependence of the Debye-Waller factor and the strong/fragile classification scheme [88].

We have generalized, based on the MCT approximation, the ISTS response function $G_{\rho T}(q,t)$ to include β relaxation as given in Eq. 3.67. Therefore one should be able to observe the β relaxation directly in ISTS data. However, as we have shown in Chapters 4 and 5, the ISTS response function $G_{\rho T}(q,t)$ given in Eq. 3.49 including α relaxation only provides excellent fits to the data collected in both salol and CKN. This is because in our current system, the fastest time scale accessible for characterization of the relaxation mode is on the order of nanoseconds, which does not permit direct observation of the (subnanosecond) β relaxation. To detect β relaxation directly, one must extend the method to shorter time scales. This is possible now with femtosecond laser pulses as excitation and the streak camera which has a time resolution on the order of *ps* as detector.

We have also shown that the longitudinal and transverse acoustic mode dynamics can be probed in VV/VH ISS experiments, from which the structural relaxational part of the acoustic modulus spectra can be constructed. We have presented an acoustic data analysis for salol following an outline given in Chapter 3. The current experimental challenge is to extend the acoustic measurements to lower and, most importantly, higher acoustic frequencies. As we have shown in Chapter 6, the data in the high frequency region are much needed to elucidate whether there is a β relaxation contribution to the acoustic modulus and compliance spectra and, if there is, to determine the minimum frequency and minimum acoustic modulus values. This will permit testing of the power-law frequency dependences in the relaxation spectra predicted by MCT.

We have reported preliminary results of orientational relaxation dynamics in salol by VH ISS experiments. Much effort is needed to explore the capability of this time-resolved depolarized light scattering technique. First of all, a theoretical understanding of the light scattering mechanism is needed in order to give precise interpretation of the data. In Chapter 7, we fitted the data with an empirical bi-exponential function and we have also pointed out that the data can be fitted with a stretched exponential function. Secondly, one has to be able to collect the data over a very wide temporal range, from fs to μm time scales, in order to unambiguously determine the orientational relaxation dynamics. This would involve using multiple laser systems. One could use femtosecond lasers to detect the orientational relaxation dynamics in the fs-ns region. For the ns-μs dynamics one would use picosecond lasers or nanosecond lasers. By combining the two or more data sets, one would obtain the orientational relaxation function over more than 6 decades of time, which would then permit precise characterization of the α and β relaxations dynamics as reflected in orientational motion.

In conclusion, the work presented in this thesis has further increased our understanding of the viscoelastic behavior of the glass-forming liquids through time-resolved light scattering. It has demonstrated that ISS is a useful tool for studying the ancient but still unresolved problems of the liquid-glass transition. It has also been shown that the complex materials examined here may be described by current theoretical models. This work, in the meantime, has brought to our attention the need for extending the dynamical range to both shorter and longer time scales and wavevectors. We hope that the work presented in this thesis will encourage others to work toward this direction.

Appendix A

The First Order Solutions for ISS and Rayleigh-Brillouin Scattering

In this appendix, we give ISS response functions and the Rayleigh-Brillouin spectrum to first order in $\nu_L q^2/c_0 q$ and $\Gamma_H/c_0 q$. For simplicity, we will consider ordinary hydrodynamics equations for simple liquids. The spectral distribution for BS is then given by

$$\sigma(q,\omega) = \frac{(1-1/\gamma)2\Gamma_H}{\omega^2+\Gamma_H^2} + \frac{1}{\gamma}\left[\frac{\Gamma_A}{(\omega-\omega_0)^2+\Gamma_A^2} + \frac{\Gamma_A}{(\omega+\omega_0)^2+\Gamma_A^2}\right]$$
$$+q\left[\frac{\Gamma_A}{\gamma c_0 q^2} + \frac{\chi}{c_0}\left(1-\frac{1}{\gamma}\right)\right]\left[\frac{-(\omega-\omega_0)}{(\omega-\omega_0)^2+\Gamma_A^2} + \frac{\omega+\omega_0}{(\omega+\omega_0)^2+\Gamma_A^2}\right], \tag{A.1}$$

where the central or Rayleigh peak (the first term) arises from fluctuations at constant pressure and corresponds to the thermal diffusivity mode, and the two Brillouin doublets (next two terms) centered at $\pm\omega_0 = \pm c_0 q$ of half width $\Gamma_A = [\nu_L + (\gamma-1)\chi]q^2/2$ result from fluctuations at constant entropy and correspond to the acoustic modes. The last two terms give the first-order solution, whose amplitude is by several orders of magnitude smaller than that of the Lorentzians. These terms yield s-shaped curves centered at $\pm\omega_0$ and cause a slight pulling of Brillouin peaks towards the central peak. The two terms are consequences of the initial condition imposed on the system: the density correlation function must have a zero derivative at t=0 [64].

For ISBS and ISTS, the response functions to the first order are

$$G_{\rho\rho}(q,t) = \frac{q}{c_0}\left\{\frac{\Gamma_H(\gamma-1)}{c_0 q}\left[e^{-\Gamma_H t} - e^{-\Gamma_A t}\cos(\omega_0 t)\right] + e^{-\Gamma_A t}\sin(\omega_0 t)\right\} \qquad \text{(A.2)}$$

and

$$G_{\rho T}(q,t) = -\frac{\kappa}{c_p}\left\{e^{-\Gamma_H t} - e^{-\Gamma_A t}\left[\cos(\omega_0 t) + \frac{\Gamma_H - \Gamma_A}{c_0 q}\sin(\omega_0 t)\right]\right\}. \qquad \text{(A.3)}$$

Notice that the real part of the Fourier transform of the term in $\sin(\omega_0 t)$ gives the last two terms in Eq. A.1 up to a proportionality constant, while the thermal diffusion term and the acoustic modes correspond to the Rayleigh line and Brillouin doublets in BS. It follows therefore from Eqs. A.1 - A.3 that both response functions $G_{\rho\rho}(q,t)$ and $G_{\rho T}(q,t)$ are related to the BS spectral distribution through Fourier transformation although there are different relative contributions for each mode. To first order, BS is very similar to ISBS and ISTS in terms of the thermal diffusion and sound propagation modes. But in practice, there are some differences. As discussed above, the last two terms in Eq. A.1 cause a weak asymmetry in the Brillouin peak in BS spectrum, which induces a slightly peak frequency shift to the center from $\pm\omega_0 = \pm c_0 q$. If one fits the spectrum to Eq. A.1 without the last two terms, the peak frequency thereby determined is then smaller than true value of ω_0. In ISS, the additional oscillatory term does not alter the frequency or damping rate but only introduces a phase shift. Fitting the data to the response functions with or without the first-order correction yields the same values for the acoustic frequency and damping rate.

Also, from Eq. A.1 - A.3 it is seen that ISTS, not ISBS is more or less the same as BS in terms of overall information content. In both $G_{\rho T}(q,t)$ and $\sigma(q,\omega)$, the thermal diffusion mode and acoustic mode are dominating terms, and the term in $\sin(\omega_0 t)$ or the last two terms in Eq. A.1 are small. In ISBS, the opposite is true. The thermal mode and additional oscillatory term $\cos(\omega_0 t)$ are too small to be detected.

In conclusion, ISTS, but not ISBS in practice provides equivalent information as Rayleigh-Briilouin scattering. Both of them contain the Rayleigh mode, acoustic mode for simple liquids, and an additional Mountain mode for complex liquids. The dynamical parameters of these three modes from ISTS and BS are the same. The only difference between ISTS and BS lies in the relative amplitudes of three modes.

Bibliography

[1] W. Götze and L. Sjögren. Relaxation processes in supercooled liquids. *Rep. Prog. Phys.*, 55:241–376, 1992.

[2] F. Mezei, W. Knaak, and B. Farago. Neutron spin-echo study of dynamic correlations near the liquid-glass transition. *Phys. Rev. Lett.*, 58:571, 1987.

[3] W. Knaak, F. Mezei, and B. Farago. Observation of scaling behavior of dynamic correlations near liquid-glass transition. *Europhys. Lett.*, 7:529, 1988.

[4] S. R. Nagel. Susceptibility studies of supercooled liquids and glasses. In T. Riste and D. Sherrington, editors, *Phase Transitions and Relaxation in Systems with Competing Energy Scales*, pages 259–283. Kluwer, Dordrecht, 1993.

[5] P. K. Dixon. *Phys. Rev. B*, 42:8179, 1990.

[6] L. Wu. *Phys. Rev. B*, 43:9906, 1991.

[7] L. Wu and S. R. Nagel. *Phys. Rev. B*, 46:11198, 1992.

[8] H. Z. Cummins, G. Li, W. M. Du, and J. Hernandez. Relaxational dynamics in supercooled liquids: Experimental tests of the mode coupling theory. *Phys. A*, 204:169, 1994.

[9] G. Li, W. M. Du, A. Sakai, and H. Z. Cummins. Light-scattering investigation of α and β relaxation near the liquid-glass transition of the molecular glass salol. *Phys. Rev. A*, 46:3343, 1992.

[10] G. Li, W. M. Du, X. K. Chen, H. Z. Cummins, and N. J. Tao. Testing mode-coupling predictions for α and β relaxation in $Ca_{0.4}K_{0.6}(NO_3)_{1.4}$ near the liquid-glass transition by light scattering. *Phys. Rev. A*, 45:3867, 1992.

[11] S. L. Sidebottom and C. M. Sorensen. Dynamic light scattering study of non-exponenetial relaxation in supercooled $2Ca(NO_3)_2{\cdot}3KNO_3$. *J. Chem. Phys.*, 91:7153, 1989.

[12] E. A. Pavlatou, A. K. Rizos, G. N. Papatheodorou, and G. Fytas. Dynamic light scattering study of ionic KNO_3-$Ca(NO_3)_2$ mixtures. *J. Chem. Phys.*, 94:224, 1991.

[13] M. J. Stephen. *Phys. Rev.*, 187:279, 1969.

[14] E. Leutheusser. *Phys. Rev. A*, 29:2765, 1984.

[15] U. Bengtzelius, W. Götze, and A. Sjölander. *J. Phys. C*, 17:5915, 1984.

[16] S. P. Das and G. F. Mazenko. *Phys. Rev. A*, 34:2265, 1986.

[17] F. Spaepen and D. Turnbull. In N. J. Grant and B. C. Giessen, editors, *Rapidly Quenched Metals; Second International Conference*, page 205. MIT Press, 1976.

[18] A. Rahman, M. J. Mandell, and J. P. McTague. *J. Chem. Phys.*, 64:1564, 1976.

[19] J. Fox and H. C. Andersen. *J. Phys. Chem.*, 88:4019, 1984.

[20] C. A. Angell, P. H. Poole, and J. Shao. Glass-forming liquids, anomalous liquids, and polyamorphism in liquids and biopolymers. *Nuovo Cimento*, 16:993, 1994.

[21] C. A. Angell. The old problems of glass and the glass transition, and the many new twists. *Proc. Natl. Acad. Sci. USA*, 92:6675, 1995.

[22] S. Dattagupta. *Relaxation Phenomena in Condensed Matter Physics.* Academic, Orlando, 1987.

[23] R. Kubo. *J. Phys. Soc. Japan*, 12:570, 1957.

[24] K. Kawasaki. *Ann. Phys.*, 61:1, 1970.

[25] I. Oppenheim. Mode coupling and long time tails. *Transport Theory and Stat. Phys.*, 24:781, 1995.

[26] J. Schofield and I. Oppenheim. *Phys. A*, 204:555, 1994.

[27] J. P. Boon and S. Yip. *Molecular Hydrodyanmics.* McGraw-Hill, New York, 1980.

[28] J.P. Hansen and I.R. McDonald. *Theory of Simple Liquids.* Academic Press, London, second edition, 1986.

[29] W. Götze. Aspects of structural glass transitions. In J. P. Hansen, D. Leveseque, and J. Zinn-Justin, editors, *Liquids, Freezing and Glass Transition*, page 287. Elsever Science, North-Holland, 1991.

[30] Götze. private communications.

[31] J. Frenkel. *Kinetic Theory of Liquids.* Oxford Univ. Press, London and New York, 1946.

[32] N. J. Tao, G. Li, X. K. Chen, W. M. Du, and H. Z. Cummins. 44:6665, 1991.

[33] Y.-X. Yan, L.-T. Cheng, and K. A. Nelson. *J. Chem. Phys.*, 88:6477, 1988.

[34] I. C. Halalay, Y. Yang, and K. A. Nelson. Testing of mode-coupling theory through impulsive stimulated thermal scattering. *Transport Theory Stat. Phys.*, 24:1053, 1995.

[35] C. H. Wang. Depolarized rayleigh-brillouin scattering of shear waves and molecular reorientation in a viscoelastic liquid. *Molecular Physics*, 41:541, 1980.

[36] C. H. Wang and J. Zhang. Studies of depolarized and polarized rayleigh-brillouin spectra of a supercooled liquid: Salol. *J. Chem. Phys.*, 85:794, 1986.

[37] T. A. Litovitz and C. M. Davis. Structural and shear relaxation in liquids. In W. P. Mason, editor, *Physical Acoustics: Principles and Methods*, volume 2, pages 281–349. Academic, New York and London, 1965.

[38] E. Bartsch, F. Fujara, B. Geil, M. Kiebel, W. Petry, W. Schnauss, H. Sillescu, and J. Wuttke. Signitures of the glass transition in a van der Waals liquid seen by neutrons and NMR. *Phys. A*, 201:223, 1993.

[39] E. Rössler, A. P. Sokolov, P. Eiermann, and U. Warschewske. Dynamical phase transition in simple supercooled liquids and polymers - an NMR approach. *Phys. A*, 201:237, 1993.

[40] W. Petry and J. Wuttke. Quasielastic neutron scattering in glass forming viscous liquids. *Transport Theory and Stat. Phys.*, 24:1075–1095, 1995.

[41] F. Mezei. *Ber. Bunsenges. Phys. Chem.*, 95:1118, 1991.

[42] M. Fuchs, W. Götze, and A. Latz. *Chem. Phys.*, 149:185, 1990.

[43] M. Elmroth, L. Borjesson, and L. M. Torell. *Phys. Rev. Lett.*, 68:79, 1992.

[44] L. Borjesson, M. Elmroth, and L. M. Torell. *Chem. Phys.*, 149:209, 1990.

[45] G. Li, W. M. Du, J. Hernandez, and H. Z. Cummins. Locating the nonergodicity-parameter anomaly near the liquid-to-glass crossover temperature in $CaKNO_3$ by Brillouin scattering. *Phys. Rev. E*, 48:1192, 1993.

[46] C. Dreyfus, M. J. Lebon, H. Z. Cummins, J. Toulouse, B. Bonello, and R. M. Pick. Brillouin scattering in salol: Determining T_c of the mode coupling theory. *Phys. Rev. Lett.*, 69:3666, 1992.

[47] H. Z. Cummins, G. Li, W. M. Du, J. Hernandez, and N. J. Tao. Depolarized light scattering spectrosocpy of glassforming liquids: Experimental tests of MCT. *Transport Theory and Stat. Phys.*, 24:981–1016, 1995.

[48] L.-T. Cheng, Y.-X. Yan, and K. A. Nelson. Ultrasonic and hypersonic properties of molten KNO_3-$Ca(NO_3)_2$ mixture. *J. Chem. Phys.*, 91:6052, 1989.

[49] S. M. Silence, S. R. Goates, and K. A. Nelson. *Chem. Phys.*, 149, 1990.

[50] A. R. Duggal and K. A. Nelson. *J. Chem. Phys.*, 94:7677, 1991.

[51] S. M. Silence, A. R. Duggal, L. Dhar, and K. A. Nelson. Structural and orientational relaxation in supercooled liquid triphenylphosphite. *J. Chem. Phys.*, 96:5448, 1992.

[52] I. C. Halalay and K. A. Nelson. The liquid-glass transition in $LiCl/H_2O$: Impulsive stimulated light scattering experiments and mode-coupling analysis. *J. Chem. Phys.*, 97:3557, 1992.

[53] I. C. Halalay, Y. Yang, and K. A. Nelson. *J. Non-Crys. Solids*, 172-174:175, 1994.

[54] A. R. Duggal, J. A. Roggers, and K. A. Nelson. *J. Appl. Phys.*, 72:2823, 1992.

[55] J. A. Rogers and K. A. Nelson. *J. Appl. Phys.*, 75:1534, 1994.

[56] J. A. Rogers, Y. Yang, and K. A. Nelson. Elastic modulus and in-plane thermal diffusivity measurements in thin polyimide films using symmetry-selective real-time impulsive stimulated thermal scattering. *Appl. Phys. A*, 58:523, 1994.

[57] Y. Yang, K. A. Nelson, and Farshid Adibi. Optical measurement of the elastic moduli and thermal diffusivity of a C-N film. *J. Mater. Res.*, 10:41, 1995.

[58] S. M. Silence. *Time-Resoved Light Scattering Studies of Structural Rearrangements in Disordered Condensed Phase Systems.* PhD thesis, Massachusetts Institute of Technology, 1991.

[59] A. R. Duggal. *Impulsive Stimulated Light Scattering Studies of the Dynamics of Viscoelastic Fluids and Thin Polymer Films.* PhD thesis, Massachusetts Institute of Technology, 1992.

[60] Y. Yang and K. A. Nelson. Impulsive stimulated light scattering from glass-forming liquids. i. generalized hydrodynamics approach. *J. Chem. Phys.*, 103:7722, 1995.

[61] Y.-X. Yan and K. A. Nelson. *J. Chem. Phys.*, 87:6240, 1987.

[62] K. F. Herzfeld and T. A. Litovitz. *Absorption and Dispersioin of Ultrasonic Waves.* Academic, New York, 1959.

[63] W. Götze. Relaxation near glass transition singularities. In T. Riste and D. Sherrington, editors, *Phase Transitions and Relaxation in Systems with Competing Energy Scales*, pages 191–232. Kluwer, Dordrecht, 1993.

[64] C. J. Montrose, V. A. Solovyev, and T. A. Litovitz. Structural-relaxation dynamics in liquids. *J. Acoust. Soc. Am.*, 43:117, 1968.

[65] R. D. Mountain. *Rev. Mod. Phys.*, 38:205, 1966.

[66] R. D. Mountain. *J. Res. Natl. Bur. Stand. Sec. A*, 70:207, 1966.

[67] R. D. Mountain. *J. Res. Natl. Bur. Stand. Sec. A*, 72:95, 1968.

[68] D. L. Sidebottom and C. M. Sorensen. *Phys. Rev. B*, 40:461, 1988.

[69] W. M. Du, G. Li, H. Z. Cummins, M. Fuchs, J. Toulouse, and L. A. Knauss. *Phys. Rev. E*, 49:2192, 1994.

[70] Y. Yang and K. A. Nelson. T_c of the mode coupling theory evaluated from impulsive stimulated light scattering on salol. *Phys. Rev. Lett.*, 74:4883, 1995.

[71] Y. Yang and K. A. Nelson. Impulsive stimulated light scattering from glass-forming liquids. ii. salol relaxation dynamics, nonergodicity parameter, and testing of mode coupling theory. *J. Chem. Phys.*, 103:7732, 1995.

[72] Y. Yang, L. J. Muller, and K. A. Nelson. Relaxational dynamics and strength in supercooled liquids from impulsive stimulated thermal scattering. In H. Z. Cummins, D. J. Durian, D. L. Johnson, and H. E. Stanley, editors, *Disordered Materials and Interfaces*, volume 407, pages 145–154. Materials Research Society, 1996.

[73] B. Frick, B. Farago, and D. Richter. Temperature dependence of the nonergodicity parameter in polybutadiene in the neighborhood of the glass transition. *Phys. Rev. Lett.*, 65:2921, 1990.

[74] W. Petry, E. Bartsch, F. Fujara, M. Kiebel, H. Sillescu, and B. Farago. Dynamic anomaly in the glass transition region of orthoterphenyl: a neutron scattering study. *Z. Phys. B*, 83:175, 1991.

[75] J. Toulouse, G. Boddens, and R. Pattnaik. Neutron investigation of the mode coupling T_c in phenyl salicylate (salol). *Phys. A*, 201:305, 1993.

[76] J. C. Halalay and K. A. Nelson. *Rev. Sci. Instrum.*, 61:3623, 1990.

[77] C. T. Moynihan, P. B. Macedo, C. J. Montrose, P. K. Gupta, M. A. DeBolt, J. F. Dill, B. E. Dom, P. W. Drake, A. J. Easteal, P. B. Elterman, R. P. Moeller, H. Sasabe, and J. A. Wilder. Structural relaxation in vitreous materials. *Ann. N.Y. Acad. Sci.*, 279:15, 1976.

[78] W. T. Laughlin and D. R. Uhlmann. Viscous flow in simple organic liquids. *J. Phys. Chem.*, 76:2317, 1972.

[79] P. K. Dixon and S. R. Nagel. *Phys. Rev. Lett.*, 61:341, 1988.

[80] P. K. Dixon, L. Wu, S. R. Nagel, B. D. Williams, and J. P. Carini. *Phys. Rev. Lett.*, 65:1108, 1990.

[81] Y. Yang and K. A. Nelson. Impulsive stimulated thermal scattering study of α relaxation dynamics and the debye-waller factor anomaly in $Ca_{0.4}K_{0.6}(NO_3)_{1.4}$. *J. Chem. Phys.*, 104:5429, 1996.

[82] H. Z. Cummins, M. Fuchs W. M. Du, W. Götze, S. Hildebrand, A. Latz, G. Li, and N. J. Tao. Light-scattering spectroscopy of the liquid-glass transition in $CaKNO_3$ and in the molecular glass salol:extended-mode-coupling-theory analysis. *Phys. Rev. E*, 47:4223, 1993.

[83] E. M. L. Beale. *J. R. Statist. Soc. B*, 22:1, 1960.

[84] E. S. Pearson and H. O. Harley. *Biometrika Tables for Statisticians.* Cambridge University, Cambridge, 1970.

[85] L. M. Torell. Brillouin scattering study of hypersonic relaxation in a $Ca(NO_3)_2$-KNO_3 mixture. *J. Chem. Phys.*, 76:3467, 1982.

[86] C. A. Angell and L. M. Torell. Short time structural relaxation processes in liquids: Comparison of experimental and computer simulation glass transitions on picosecond time scales. *J. Chem. Phys.*, 78:937, 1983.

[87] M. Fuchs, H. Z. Cummins, W. M. Du, W. Götze, A. Latz, G. Li, and N. J. Tao. Tests of the mode-coupling theory for a molten salt. *Phil. Mag. B*, 71:771, 1995.

[88] C. A. Angell. *Nuclear Phys. B*, 5A:69, 1988.

[89] G. I. A. Stegeman and B. P. Stoicheff. *Phys. Rev. A*, 7:1160, 1973.

[90] H. C. Andersen and R. Pecora. Kinetic equations for orientational and shear relaxation and depolarized light scattering in liquids. *J. Chem. Phys.*, 54:2584.

[91] N. D. Gershon and I. Oppenheim. Line shapes for low frequency depolarized (VH) light scattering from fluids. coupling of rotational and translational motion. *J. Chem. Phys.*, 59:1337.

[92] B. J. Berne and R. Pecora. *Dynamic Light Scattering.* Wiley, New York, 1976.

[93] S. M. Rytov. *Sov. Phys. JETP*, 6:401, 1958.

[94] M. Fuchs and A. Latz. Depolarized light scattering at the liquid to glass transition. *Ber. Bunsenges. Phys. Chem.*, 95:1131, 1991.

[95] M. Fuchs and A. Latz. Light scattering at the liquid to glass transition. *J. Chem. Phys.*, 95:7074, 1991.

[96] J. Wuttke, J. Hernandez, G. Li, G. Coddens, H. Z. Cummins, f. Fujara, W. Petry, and H. Sillescu. *Phys. Rev. Lett.*, 72:3052, 1994.

[97] M. J. Lebon, C. Dreyfus, G. Li, A. Aouadi, H. Z. Cummins, and R. M. Pick. *Phys. Rev. E*, 51:4537, 1995.

[98] W. Steffen, A. Patkowski, H. Glaser, G. Meier, and E. W. Fisher. *Phys. Rev. E*, 49:2992, 1994.

[99] E. Rössler, A. P. Sokolov, A. Kisliuk, and D. Quitmann. *Phys. Rev. B*, 49:14967, 1994.

[100] C. Alba-Simionesco and M. Krauzman. *J. Chem. Phys.*, 102:6574, 1995.

[101] H. Z. Cummins, G. Li, W. M. Du, R. M. Pick, and B. Dreyfus. Origin of depolarized light scattering in supercooled liquids: Orientational fluctuation versus induced scattering mechanisms. *Phys. Rev. E*, 53:896, 1996.

[102] P. P. Ho and R. R. Alfano. Relaxation kinetics of salol in the supercooled liquid state investigated with the optical kerr effect. *J. Chem. Phys.*, 67:1004, 1977.

[103] S. Ruhman and K. A. Nelson. Temperature-dependent molecular dynamics of liquid carbon disulphide: Polarization-selected impulsive stimulated light-scattering data and kubo line shape analysis. *J. Chem. Phys.*, 94:859, 1991.

[104] B. Kohler and K. A. Nelson. Femtosecond impulsive stimulated light scattering from liquid carbon disulfide at high pressure: Experimental and computer simulation. *J. Phys. Chem.*, 96:6532, 1992.